UNIVERSITY OF OKLAHOMA

GRADUATE COLLEGE

A CONTROLLED-SOURCE SEISMIC AND GRAVITY STUDY OF THE HIGH LAVA PLAINS (HLP)

A THESIS

SUBMITTED TO THE GRADUATE FACULTY

in partial fulfillment of the requirements for the

Degree of

MASTER OF SCIENCE

By

CATHERINE COX

Norman, Oklahoma

2011

A CONTROLLED-SOURCE SEISMIC AND GRAVITY STUDY OF THE HIGH LAVA PLAINS (HLP)

A THESIS APPROVED FOR THE
CONOCOPHILLIPS SCHOOL OF GEOLOGY AND GEOPHYSICS

BY

Dr. Randy Keller, Chair

Dr. Kurt Marfurt

Dr. Barry Weaver

Dedication

To my father, of blessed memory, for his love and support

ACKNOWLEDGEMENTS

This work would not have been possible without the support of NSF grant EAR-0641515, and a Research Assistantship from the Conoco Phillips School of Geology and Geophysics at the University of Oklahoma. Also a special thanks to IRIS and EarthScope for their travel grants received to attend conferences to present my research and providing support in my early professional development.

The High Lava Plains (HLP) experiment would not have been a success without the team of 67 scientists. They were a very remarkable group, and I am honored to have had the opportunity to work with them. I am also indebted to IRIS/ PASSCAL for lending their instrumentation and for their support during the field operation. I also owe a Special thanks to: Sara Alsbury who helped me survey all 2612 station locations, Galen Kaip who assisted with data issues, "Uncle" Steve Harder who worked on many aspects of the project and provided great mentorship and support, Dr. Matt Fouch and Kevin Eagar who compared models and results through the entire process, Dr. Anita Grunder and Jenda Johnston who brought such vibrant energy and an unmeasured wealth of knowledge, and finally all the primary investigators who provided feedback and positive support during this project.

I am also grateful to the staff at the ConocoPhillips School of Geology and Geophysics at the University of Oklahoma (OU) who lent an ear and additional support during my father's illness and passing: Niki Chapin, Adrienne Fox, Teresa Hackney, Nancy Leonard, and Donna Mullins. I would also like to acknowledge Dr. Tim Kwiatkowski, Brad Wallet, and Oswaldo Davagusto for their support in the Shell Crustal Imaging Facility (SCIF), and for their assistance with any unexpected computer

problems. Thank you to Bunmi Elebiju, Jefferson Chang, and Maxwell Okure for the numerous hours of help and patience. Thank you to Eva Rumpfhuber for teaching me the fine art of modeling and being a great friend and mentor. Special thanks also to Dr. Doug Elmore for his support, the late Dr. Roger Young for his interest in my research and encouragement, Steve Holloway for his technical assistance and support, Dr. Mike Engle for his support and offering a laugh when needed, Dr. Katie Keranen for her technical guidance, Dr. Barry Weaver for his interest in my research and endless knowledge of petrology, and the mentorship and humor from Dr. Kurt Marfurt.

Last, but certainly not least, I would like to thank Dr. Randy Keller for turning this rough geologist into a well-rounded geophysicist. It has been an honor to work with him, and I cannot thank him enough for everything he has done for me. He gave me the confidence I needed to overcome any challenges that were thrown my way and believed in me even when I didn’t believe in myself. I am the young professional and person I am today thanks to his mentorship.

TABLE OF CONTENTS

TABLE OF FIGURES

ABSTRACT

This study uses data collected during the High Lava Plains (HLP) controlled-source experiment in September of 2008. A total of 2612 Texan short-period seismic recorders and 120 RT-130 recorders were spaced across the HLP of eastern Oregon and adjacent parts of Nevada and Idaho to record 15 seismic sources. Seismic and gravity data were integrated to create 2-D crustal scale P-wave velocity and density models for the long NW-SE and N-S profiles to provide a better understanding of the crustal and upper mantle structure. These are the first high-resolution images beneath the path of migratory, bi-modal volcanism that dotted the High Lava Plains since16 Ma, in addition to the extension experienced in the region since 35 Ma. My models show that the crustal structure across the HLP region is similar to that of the northern Basin and Range. A thick layer (5-7 km) of sediments and volcanics extends over most of the area and is thickest in the Harney Basin area. I interpret denser/faster material in the lower to middle crust under the southern Harney Basin area to be mafic intraplating. I have also identified a region of denser/faster material in the upper crust in the vicinity of Jordan Valley. The crust thickens (34-37 km), and the lower increases in density (2.8-2.85 gm/cm^3) from west to east across eastern Oregon in close proximity to the interpreted position of the 0.706 Sr isotope line, suggesting moderate extension. In the lowermost crust below the southeastern HLP, there is relatively high velocity (7.2-7.4 km/s) and density (2.95 gm/cm^3) that suggests underplating. The HLP region has undergone moderate extension, and the average crustal velocity is somewhat higher than in the adjacent Basin and Range suggesting some magmatic modification in the lower crust, but not as much as might be expected given the voluminous surface volcanism.

INTRODUCTION

Central Oregon is part of an enigmatic volcanic province in the western United States (Figure 1). This region is one of the most accessible yet least understood examples of large-scale intraplate volcanism, which leads to the question as to why there is large volume volcanism in this less extended domain while the highly extended regions of the Basin and Range have undergone less volcanic activity. There is an estimated 220,000 km^3 of basalt in this region [*Camp and Ross,* 2004]. This leads to further questions about is the crustal structure beneath the widespread flood basalts, which are the focus of this thesis.

This area lies between two Cenozoic rhyolitic age progressive tracks of eruptions that roughly mirror each other. The Yellowstone track becomes younger to the NE and the Newberry trend becomes younger towards the NW (Figure 1). Episodes of volcanism occurred in north Oregon, southern Washington, and northern Idaho ~17 Ma. Episodic basalt volcanism blankets the Columbia Plateau to the north. The Columbia River Basalts were erupted by the Chief Joseph and Monument feeder [*Camp and Ross,* 2004] (Figure 1). This region is bounded to the west by the subducting Juan de Fuca plate, which has influenced the complicated tectonic and magmatic history of the western United States since 50 Ma. This flat-slab subduction of the Farallon plate, now remnant Juan de Fuca plate, created favorable conditions for the large-scale volcanism seen in central Oregon [*Severinghaus and Atwater,* 1989] (Figure 2). As the Juan de Fuca plate subducted beneath North America, the Pacific Northwest has undergone clockwise rotation with the pole of rotation, located by current GPS data, on the Washington-Oregon border, which is consistent with the direction of extension in southern Oregon since the Cenozoic [*McCaffrey et al*., 2000].

The High Lava Plains (HLP) of central Oregon is a physiographic province characterized by late Tertiary to Cenozoic bimodal volcanism and extension that extends from the Newberry volcano to the Snake River Plain (SRP). In earlier studies, a portion of the HLP was referred to as the Oregon Plateau, but for this study, we will refer to this area as the HLP [e.g., *Christensen and McKee, 1978, Carlson and Hart,* 1987]. The HLP is centrally located in the US Cordillera and extends across a portion of the northern Basin and Range Province of south-central Oregon (Figure 3). The HLP is bounded to the west by the Cascade Range, to the north by the non-extended accreted terrains of the Blue Mountains, and to the east by the Snake River Plain. Various volcanic centers [Jordan Craters, Diamond Craters, and Cow Lakes volcanic fields, Figure 3)] lie within the HLP region. The Owyhee Plateau and the 0.706 Sr isotope lines lie to the east of Jordan Craters. The 0.706 line (Figure 3) is interpreted to be the boundary between the North American Craton and Mesozoic accreted terrains [*Armstrong et al.,* 1977]. The Bruneau-Jarbidge and Twin Falls volcanic centers lie east of the 0.706 Sr isotope line, and to the west, the Columbia River Basalt, Steens Basalt, and Nevada feeder dikes. (Figure 3)

The HLP has a particularly complicated history of volcanic events because of the back arc volcanism that occurred ~30 Ma, as well as the ignimbrite flare-up of large-scale silicic magmas that spread across the region from north to south at ~20-25 Ma, [e.g. *Lipman et al.,* 1972], and the large volume basaltic volcanism in the Snake River Plain and the Columbia River Plateau ~17 Ma [*Luedke and Smith* 1984, 1991]. The HLP is one of two felsic volcanic tracks that migrated away from the McDermitt caldera complex beginning ~16 Ma [*Armstrong*, 1977]. These two trends roughly mirror each other (Figures 1 and 3). The Newberry rhyolite trend grows progressively younger towards the northwest to the vicinity of the Newberry volcano, and the Eastern Snake River Plain (ESRP) progression becomes younger to the NE towards the Yellowstone caldera [*Armstrong*, 1977*, Jordan et al.,* 2004]. Present day felsic volcanism is currently concentrated at Yellowstone and Newberry volcano (Figure 4).

The initiation of the almost symmetric rhyolitic trends began at about the same time (~16 Ma) as the beginning of the flood basalt event in southeastern Oregon. Large pulses flood basalt eruptions created the Columbia River Plateau and the western Snake River Plain northern Idaho from ~14-17 Ma. In addition, the Steens Basalt eruptive event occurred at ~16 Ma and produced 65,000 km^3 of basalt covering much of eastern Oregon [*Carlson and Hart*, 1987]. Large pulses also occurred from ~4-7 Ma in southern Idaho, while central Oregon and central Idaho experienced mafic eruptions from ~3 Ma to the present (Figure 5).

In addition to the magmatic events in the region, Basin and Range extension adds complexity to the geologic history of the HLP. The Basin and Range lies to the south of the HLP and is a region in the US Cordillera characterized by large-scale extension and crustal thinning. This province is divided into 3 regions: Southern, Central, and Northern. The High Lava Plains marks the northern extent of the Basin and Range and has experienced less extension but significantly more volcanism than other regions of the Basin and Range. The Basin and Range structure terminates at the southern end of the NW striking Brothers fault zone [e.g., *Lawrence,* 1976; *Pezzopane and Weldon,* 1993] that approximately follows the axis of the Newberry volcanic trend. It is estimated that central Oregon has undergone ~17% extension oriented in a WNW direction during the Cenozoic as a result of rotation of the Oregon coastal block [*Wells and Heller*, 1988; *Wells et al.*, 1998]. Presently, it is unknown what influence the extension of the northern Basin and Range had on crustal structure beneath the HLP.

High Lava Plains controlled source experiment

To better understand the crustal structure beneath the HLP, a high resolution controlled source seismic survey was conducted in September 2008 to image the crustal and upper mantle structure and to advance understanding of the tectonic evolution of the region. A total of 2612 Texan short-period seismic recorders and 120 RT-130 recorders from the PASSCAL and EarthScope instrument pools were deployed, and 15 seismic sources spaced across the High Lava Plains (HLP) region (Figure 6) were fired. This was the largest number of instruments deployed in an on-land controlled-source seismic experiment on a crustal scale and was possible thanks to the 42 students from 12 different universities, mainly the University of Oklahoma, Stanford University, Oregon State University, Arizona State University, Massachusetts Institute of Technology, Miami University, University of Texas at Dallas, and University of Rhode Island, as well as a team from the Carnegie Institution of Washington and HLP researchers These deployers were ably assisted by 6 staff members from the PASSCAL/EarthScope Instrument Center.

This controlled source seismic study was part of a larger multidisciplinary effort led by Carnegie Institute of Washington and Arizona State University and included an array of 117 broadband seismometers that were deployed over three years. The University of Oregon, Michigan Tech, and the U. S. Geological Survey also deployed an array in the Newberry volcano area to record earthquakes and the seismic sources.

Together, the goal of these efforts was to provide a deep and three-dimensional image of the regional crustal and upper mantle structure. New instrumentation built by the PASSCAL Instrument Center staff made it possible to carry out 3-component recording using three Texan single-channel instruments to study detailed crustal structure and anisotropy across the towering Steens Mountain region. The seismometers were deployed to provide high-resolution images of the mantle and crust directly beneath the path of the High Lava Plains volcanism since 16 Ma. In addition to the seismic component, the overarching project included a variety of geochemical investigations and geodynamic modeling and was funded by the National Science Foundation's Continental Dynamics program (http://www.dtm.ciw.edu/research/HLP). In this thesis, I present crustal velocity models and density models for the main profiles of the HLP controlled source experiment and discuss their tectonic implications.

PREVIOUS GEOPHYSICAL INVESTIGATIONS

Previous geophysical studies in the High Lava Plains are limited. *Catchings and Mooney*, [1991] conducted a study in the western portion of the HLP that began near Newberry caldera and extended eastward parallel the western portion of the HLP Line 1 profile (Figure 7). Their 180 km long profile used 9 shots ranging from 900 to 1800 kg spaced 15 km apart, and 120 USGS cassette-recording seismographs in a linear array east and west of Newberry volcano. The recorders were deployed twice and the longer offset shots were fired twice, thus producing a total of 240 recording stations. Catchings and Mooney found that the layers of weathered sediments and volcanics ranged from 3-5km thick with velocities ranging from 4.1-4.7 km/s (Figure 8). This layer was underlain by thin upper crustal layer with a velocity of 5.6 km/s, and the middle consisted of two layers with velocities ranging from 6.1-6.5 km/s. A fast (7.4 km/s) layer was found above the Moho whose depth was 37 km, and the upper mantle velocity (Pn) averaged 8.1 km/s (Figure 8). They concluded that Oregon had undergone significant extension, volcanism, and crustal underplating.

Another study was conducted by *Lerch et al.* [2007] in the northern Basin and Range, and Line 2 of the HLP experiment was designed to tie to this 300 km long profile (Figure 7). The design of this survey employed 1100 vertical seismometers, single channel Reftek RT125 (Texan) recorders, and Reftek RT130 recorder with 3-component sensors located at 300m station spacing to record 5 inline-shots and 1 off-line fan shot. The explosive source varied from 1100-1800 kg. Within the 300 km profile, 100 m spacing was used for ~ 35 km of the line to record a vibrator source. In addition to the seismic sources, mine blasts from 2 mines located in the eastern part of the seismic line were recorded. There is a gap in the eastern part of the line that is ~ 10 km long. They found that northern Nevada underwent 20% extension. The mid-crust has relatively low crustal velocities of 5.9 – 6.1 km/s and Moho depths ranged from 30 - 35 km depth with velocities of 6.6 km/s – 6.8 km/s in the lower crust and averaging 8.0 km/s below the Moho. Their model also found no evidence for underplating. At the intersection of the HLP Line 2 profile and this survey, the Moho depth is ~30 km with lower crustal velocity of ~6.8 km/s (Figure 9).

DATA ACQUISITION

The HLP large-scale controlled source seismic experiment was carried out by the team of 67 scientists, as well as students, and volunteers who deployed a total of 2612 Texan short period instruments across the High Lava Plains (HLP). Although this was the first academic land acquisition of this size, based on the number of instruments, the total time to execute this deployment from start to finish was 7 days.

This seismic survey is designed to image the crust and upper mantle with the purpose of understanding the tectonics and mechanisms that drive the intraplate volcanism of the High Lava Plains. The key geologic reason for this survey design is to understand why the HLP, which is in part a minimally extended part of the northern Basin and Range, has been the most volcanically active region of North America during the late Cenozoic. The two intersecting seismic refraction / wide-angle reflection lines (Line 1 and Line 2) are the focus of this thesis (Figure 6). The array consisted of 2612 receiver stations connected to 4Hz geophones spaced approximately 800 m apart. The northwest-southeast transecting line (Line 1) was approximately 400 km long, and the north-south trending line (Line 2) was approximately 350 km long. In the center of the seismic survey, we conducted a sparse 3-D deployment around the Harney Basin. Also included within the line profiles, a “piggy-back” survey was conducted by the Stanford University research group using 120 REFTEK130 receivers at less than half the receiver spacing used in the regional survey. This “piggy-back” investigation was designed to collect data, some of it 3-component, across Steens Mountain (Figure 6).

Pre-experiment Procedures

Pre-experiment procedures were begun approximately two years before the field deployments. The deployment scheme for the instruments was determined and permits were obtained to deploy along the highways and roads involved. The shotpoints were located, and permits were obtained from private landowners, the National Forest Service, and the BLM granting us permission to place some instruments off main roads and place

15 one-ton seismic sources in the proposed acquisition design. During the summer of 2008, a colleague and myself surveyed the field area. The first step in this process was the programming of two Garmin GPS units with preliminary coordinates generated by National Geographic's TOPO!® Software. The surveyed points were located at 800 m station spacing. The GPS unit would beep upon arrival at the preliminary waypoint, and then the surveyors located a good location of the instrument and placed the GPS unit on the ground to get an exact surveyed waypoint. Once the survey point was collected, the GPS unit was moved and set at the next waypoint. This procedure was repeated for all 2612 waypoints. A similar procedure was conducted during the reconnaissance for the shot locations.

While the Texan locations were being surveyed, the drilling of the shot holes commenced. The boreholes were drilled to a depth of 24 m with a diameter of 30.5 cm. These holes were filled with emulsion that filled approximately 6 m of the hole and the remaining 18 m of the hole was filled in order with a bentonite layer, angular gravel to hold the shot in, and finally with cuttings from the drilling. Finally, the shotpoint was capped and locked for security purposes (Figure 10).

The Deployment

The deployer's week started with a safety and deployment training session, which included field exercises on the GPS unit, digging the hole for the Texan, and planting the geophone. There were a total of 16 deployment teams, which made the task of deploying 2612 Texans less overwhelming; each team was instructed to think of their deployment as their own small experiment consisting of 60-75 instruments (Figure 11). On deployment day each team received the following items: Texan instruments (Figure 12), 4 Hz geophones, a GPS unit with pre-programmed waypoints for each Texan location, a map of their deployment area, a spreadsheet to record GPS points and take field notes, a packet of safety information, copies of the permits, shovels, and safety vests.

During the deployment, the GPS was used to alert the deployers where to place the instruments. The deployers were free to move the location of the instrument based on safety and security, and noise source considerations. Once the instrument and geophone were placed in the ground, a new waypoint was recorded and marked on the spreadsheet. Some deployers had the opportunity to use a new technology developed by the IRIS PASSCAL group called the "Lunch Box". The "Lunch Box" was designed to minimize bookkeeping errors while in the field (Figure 13). Once the deployers finished at one station, they repeated this procedure to complete the deployment. On the final night, after all the instruments had been deployed, 5 shooters fired all 15 shots in one night. The next day the instruments attempted to record mine blasts from a mine in Winnemucca, Nevada. The next two days were used to retrieve the instruments. Groups used their waypoints and field notes from the deployment to locate the deployed instruments. Deployers were asked to record a waypoint before they removed the instruments from the ground. Each time waypoints were recorded; they were also downloaded to their GPS unit. The coordinates were used to create a geometry file compiled by averaging the deployment and retrieval coordinates from the GPS units and spreadsheets were used as a back up. The preliminary coordinates were used only as a guide for finding the station locations during deployment. The final days of the effort were used for cleaning the field sites, cleaning and packing equipment, and celebrating the success of this unique, large-scale experiment.

SEISMIC PROCESSING AND MODELING METHODS

Processing

Once the field data were collected, the data set was preprocessed and record sections were cut by the IRIS/ PASSCAL group. One challenge encountered once I started working was displaying the data so that the phases of interest (Figure 14) could be identified. Each shot gather had to be separated into a file for its appropriate line and the offsets for each trace had to be evaluated. These pre-processing steps are shown in Figure 15, which shows the preliminary workflow for the HLP data set. This workflow was developed by [*Rumpfhuber et al.,* 2009] for the CD-ROM data set, and was tailored to the HLP dataset (Figure 16). Pre-processing was preformed using PROMAX®, which is a commercial product of Landmark. First, Line 1 and Line 2 were separated from each record section using PROMAX®. Figures 17 and 19 show the raw data for the common shotpoint (SP 14/25), for Lines 1 and 2 respectively. Then noisy and dead traces were killed, and trace headers were checked to ascertain that each trace was in its correct position. If the traces were not positioned correctly, a simple script was used to correct this problem. Additional processing for Line 2 was necessary because of an error within the sign convention causing for some of the traces to plot in the wrong position. Next SEG-Y files were then exported into zp for Pg and Pn phase picking. A spectral analysis was conducted to assess the frequencies of the data and noise so filters could be designed to eliminate noise. A bandpass filter of 1-2-12-15 Hz was used because the data had a frequency range of 2-15 Hz. Traces of poor quality were killed, and an AGC of 7s was applied to the data, which made picking the first arrivals easier. PROMAX was then used to pick PcP and PmP. Figure 18 and Figure 20 show the clean shotgathers for SP 14 and SP 25. By utilizing the hyperbola velocity tool, phases PcP and PmP were easily identified and picked. The picks were exported into zp and modeled before the next steps for modeling could be completed. Figures 18 and Figure 20 show data from the shared shot point 14/ 25 with travel-time phase picks. These travel-time picks were used for the forward modeling of Line 1 and Line 2.

Phase identification and travel time picking

The first step in creating a velocity model is properly identifying crustal phases present in the data. The validity of a velocity model is based on the quality of the travel-time picks [*Zelt,* 1999]. In a crustal scale refraction/wide–angle survey, key phases must be identified to create a velocity model, and in the HLP data, the crustal diving wave (Pg) phase or first arrival up to the Moho refracted wave (Pn) crossover, the mid-crustal layer (PcP), and the Moho reflector (PmP) (Figure 14) were present. The Pg and Pn phases are normally picked first because they easily identifiable in the data. The Pg (first arrival) phase and the reflectors were picked while displaying the data in a reduced time of 6.0 km/s, and the Pn (Moho refraction) was picked in a reduced time of 8.0 km/s. Pg and Pn travel time picks were made using ‘zp’, which is a readily available routine written by Colin and Barry Zelt and can be downloaded from their websites [*Zelt and Smith,* 1992]. This program can be utilized to plot SEG-Y files, construct models, and raytrace models by solving the wave equation via asymptotic ray theory. These crustal phases were forward (trial-and-error) modeled using the travel-time picks interpreted from the field data by comparing the observed traveltimes to the calculated values. Numerous iterations of adjusting the boundary and velocity nodes to obtain a match were made.

Using PROMAX, the PmP reflector phase and PcP mid-crustal reflector phase were picked utilizing the hyperbola velocity tool in PROMAX that made identifying the deeper reflections easier. These phases were then exported from PROMAX into ‘zp’. The picks were reformatted using ‘zp’ and then exported to the model building routine VMED and raytrace inversion program RAYINVR. Then picks were then modeled and modified until a final velocity model was developed displayed good agreement between the travel-time picks and calculated values. The validity of a final velocity model is dependent on the picks and the processing and modeling methods.

Forward Modeling of the Observed Traveltimes

The first step in developing a velocity model is creating a good starting model from previous geophysical data if it is accessible. For Line 1, a model created from the *Catchings and Mooney* [1991] experiment in the western HLP are was employed (Figure 8), and the southernmost section of Line 2 was modeled after *Lerch et al.,* [2007] (Figure 9). The models were created in VMED. The layer boundaries and velocities are controlled by nodes and can be edited interactively in the VMED program or via the v.in file. One pitfall of the VMED program is that the layers must be continuous for the ray tracing to be effective. Despite this shortcoming of the program, it is possible to insert a floating reflector and pinchout layers. Once a model is built, RAYINVR is used to raytrace the observed traveltimes. RAYINVR is a raytracing program utilizing asymptotic ray theory to solve the wave equation. It is effective in modeling crustal scale models, because it is fast and effective in identifying events with particular propagation paths. Forward modeling is an iterative process in which the model is modified in VMED and rays are traced in RAYINVR until the travel time picks and calculated travel time values match. Sometimes during this process, repicking in zp might be necessary.

A top down approach, as mentioned in [*Zelt,* 1999]*,* was used in constructing the models. I began modeling the top layer and modeling each subsequent layer below until all layers were modeled. I modeled the first arrivals and Pn phase to obtain the overall velocity structure of the model, beginning with the top layers and working downward. Then I modeled the PcP and PmP phases. This process involved several iterations between modifying the picks as well as the model. The RMS values quantify the travel-time pick misfits. Values closest to 0 are interpreted to mean a perfect fit between the calculated values and the travel- time picks from the data. For crustal scale refraction/ reflection experiments, a value of 0.10 is ideal for the Pg phase, and 0.20 is ideal for the PcP, PmP, and Pn phases. Once a good fit model with RMS values close to the accepted values was obtained, I ran the DMPLSTSQR inversion code from *Zelt and Smith* [1992] to calculate the inversion to reduce the RMS values. The inversion works best when the model created by forward modeling exhibits a satisfactory agreement in travel time picks and calculated values. The inversion is also conducted in a top down approach similar to that of the forward modeling. Once an inversion was calculated, the resulting model was the final result.

In addition to the RMS values, a plot of the values of the diagonal of the resolution matrix is another way to assess the model as outlined in *Zelt* [1999]. The size of each velocity and depth node represents the value of the corresponding diagonal element of the resolution matrix. Diagonals of the resolution matrix with a value of 1 are ideal, and values less than 1 indicate a spatial averaging of the true earth structure by a linear combination of model parameters. Resolution matrix diagonals greater than 0.5 are considered to indicate well resolved model parameters. Since the diagonals also indicate the number of rays that sample a model parameter, resolution matrix diagonals less than 0.5 indicate poor ray coverage and/or poor representation of the earth structure in the model parameterization.

A velocity model is only as strong as the travel-time picks that are modeled. RMS values and resolution matrix diagonals can be used to quantify the robustness of the model, but it is the ray coverage that influences the validity of these techniques. Figure 21a-d show the ray coverage for Line 1 based on the travel-time picks produced in RAYINVR. Figure 22a-d show ray coverage for Line 2. The lack of ray coverage can be attributed to the spacing of the shotpoints along both lines. Areas with higher resolution matrix values have denser ray coverage, whereas areas with minimal ray coverage have lower values. Figures 23 and 24 show good agreement between the travel time picks from the field data (shown in color) and the calculated values (shown in black) generated by the Zelt program for Line1 and Line 2.

Seismic Models

Line 1

Figure 25 shows the model for Line 1 of the High Lava Plains that was constrained by Pg, PcP, PmP, and Pn velocity picks during forward modeling. Then DMPLSTSQR was run to calculate the inversion to improve the fit of the travel time picks. In order to assess the model, I used RMS values to quantify the travel-time pick misfits. A value of 0.10 is ideal for the Pg phase, and 0.20 is ideal for the PcP, PmP, and Pn phases. For Line 1 the following picks per phases with RMS values were modeled: 415 Pg picks (.178), 70 PcP (0.144), 133 PmP (.202), and 68 Pn (0.166). After the inversion the RMS values were reduced to Pg (.135), PcP (.153), PmP (.196), and Pn (.107). Figure 26 shows the final model for Line 1 after the inversion. Figure 27 shows the resolution diagram for line 1 after the inversion. The resolution in the upper layers is good, but as would be expected, the lower layers are not as well resolved. This is of course due to lack of dense ray coverage of the deeper phases (Figure 21).

This model shows that the cover of sediments and volcanics is ~5-7 km thick, gradually decreasing in thickness eastward from the Harney basin. These sediments overlay Basin and Range structure in the western portion of the profile and in the far eastern portion of the profile. The horst structures in the east lie in the Oregon-Idaho graben area. Areas of faster material are located under the Harney Basin, and in the extreme eastern part of the profile, these anomalies are interpreted igneous bodies in the shallow crust. The upper crust is relatively slow with average velocities of ~6.1 km/s. It is important to note, that the bottom of the upper crust is a reflector and not a continuous boundary as depicted in Figure 26. In the lower crust, the velocities range from 6.4 to 7.3 km/s and are lower in the west and underneath the Harney Basin, but to the east a 7.xx layer (7.2 -7.3 km/s) is present. These lower crustal velocities suggest that underplating has occurred. Moho depths along the Line 1 generally increase eastward. In the west under apparent horst and grabens and Harney basin, the Moho depth is ~30~35 km, and increases 37 km at the eastern portion of the profile. There is a gradual increase in thickness from underneath sp15, which corresponds to the location of the Owyhee Plateau region.

Line 2

Figure 28 shows the model for Line 2 of the High Lava Plains experiment and has been constrained by Pg, PcP, PmP, and Pn velocity picks by forward modeling. For Line 2, the following picks per phase with RMS values were modeled: 429 Pg (.176), 86 PcP (.187), 119 PmP (.162), and 21 Pn (.098). After the inversion, the RMS values were reduced: Pg (0.126), PcP (0.150), PmP (0.169), and Pn (0.161). Figure 29 shows the final model for Line 2. Figure 30 shows the resolution diagram for the final Line 2 model. Figure 30 shows the resolution diagram for Line 2 after the inversion, which shows that the upper layers are well resolved while the lower layers are not as well resolved. This to be expected is due to lack of dense ray coverage for the deeper phases, as seen in Figure 22.

This profile extends northward from the Basin and Range, along the Steens Mountain area, into the HLP and Harney basin, and terminates at the southern boundary of the accreted terrains. This model displays two ~5-7 km thick layers of sediments and volcanics across its entirity. Thes layers cover Basin and Range structures in the southern portion of the profile,and thicken in the Harney Basin area. The upper crust benarth these layers contains an area of faster material under the southern Harney Basin. Otherwise, the upper crust consists of relatively slow material with average velocities of ~6.1 km/s in the south that gradually increase to the north. In the lower crust, the velocities range from ~6.5 km/s in the south, and increase northward to the Harney Basin area where there evidence for a thin 7.xx layer. These lower crustal velocities suggest that underplating may be occurring in the northern portion of the profile. Moho depths along the Line 1 profile increase northward. To the south under the Basin and Range, , the Moho depth is ~29 km and it rapidly increases to ~35 km under the HLP and boundary of the accreted terrains.

GRAVITY AND MAGNETIC METHODS

Gravity maps and Processing

A series of gravity maps were created for the High Lava Plains. The data used to create the gravity maps were obtained from the PACES website (http://paces.geo.utep.edu/gdrp/Search.aspx), that is a database with North American gravity data that is readily available to the public [*Keller et al.,* 2005 *and Hinze et al.,* 2005]. The data were processed using Oasis Montaj and then gridded. Once the grid was created, it was projected into the WGS 84/ UTM 11N coordinate system. First, a complete Bouguer anomaly map was generated from the gridded data (Figure 32). Then an upward continuation of 30 km was applied to the data (Figure 33). I started with a 20 km upward continuation grid that resulted in a residual map that appeared noisy and did not accentuate the major gravity anomalies of interest. Then the upward continued grid of 35 km was subtracted from the complete Bouguer anomaly grid to obtain the residual map (Figure 34) that provided the desired anomaly separation. The residual map shows the Harney Basin to be a region of intermediate gravity anomalies with areas of gravity highs. The Snake River Plain and Owyhee Plateau appear as gravity highs. The gravity low that represents Steens Mountain is misleading because this area has data coverage.

The residual gravity confirms the previous proposed thoughts about the High Lava Plains. There is not significant regional high in the area such as the prominent one as seen in the Snake River Plain or a regional low as seen in the Idaho Batholith.

Magnetic Maps and Processing

Constructing the magnetic map was very similar to constructing the gravity map. I compiled my magnetic data from http://crustal.usgs.gov/geophysics/state.html. Unlike the gravity data, the downloaded magnetic data was already gridded. Once the data were downloaded, the data set was input into Oasis Montaj to be processed. Once the grid was constructed, the data was reprojected to WGS84/UTM 11N. This projection matches the gravity maps and the topography map. Starting with the Total Magnetic Intensity (TMI) map, I tested different upward continuation filters. This process allowed me to take slices of the anomalies at different depths. After trying several iterations, the 20 km upward continuation filter provided the best for eliminating desired wavelengths. The 20 km upward continuation grid was subtracted from the TMI grid to obtain the residual (Figure 35). A comparison of the TMI grid and the residual grid show that they are very similar in appearance; However, the residual grid exhibits more lineations of magnetic highs in the Snake River Plain, N-S trends in the Basin and Range, and similar N-S trending lineations in the High Lava Plains. Because of the volume of volcanics in the HLP, no regional interpretations could be made from the residual magnetics.

Density Modeling

Line 1

The Line 1 gravity model was constructed using GYMSYS within the Oasis Montaj program (Figure 35). GYMSYS uses the principles of modeling 2D bodies as polygons [*Talwani,* 1959] to match the computed values to the residual gravity until the curves match. For crustal scale modeling, 2 mGal is the margin of error that was tolerated, because this value is the estimated precision of the anomaly values in the dataset. A profile along the HLP seismic Line 1 (Figure 29) was selected for modeling, and the Line 1 seismic model was employed as a constraint for constructing the gravity model. The dimensions of the model were 410 km long by 70 km deep. Since the program warps the ends, the length of the model is actually longer than the one above correcting for the curvature of the ends. The model boundaries were constructed to resemble the seismic model. To determine the densities, I used the relationship between P-wave velocity and density presented by *Brocher* [1995] and shown below where rho is the density.

$$V_p\,(\text{km/sec}) = 39.128\rho - 63.064\rho^2 + 37.083\rho^3 \; 9.1819\rho^4 \; 0.8228\rho^5$$

Once the density and velocity relationships were determined, only short wavelength anomalies needed to be changed to obtain a close fit observed and calculated values (Figure 35). Longer wavelength anomalies were well constrained by the seismic model. The upper part of the model consists of low-density materials that represent sediments and volcanics that thin east of the Harney Basin and covers the Basin and

Range structures in the western part of the profile. Some dense shallow material is located under the Harney Basin, and there are horst and graben structures in the eastern part of the profile that are also related to denser material. The upper crustal densities (2.75-2.78) are representative of the slower velocity felsic material with minor variations in density values. The lower crust exhibits a lateral density decrease from west to east. This corresponds with the thickening crust towards the east. The pink layer is dense material that is interpreted as underplating. This model has a fit error of 2.2 mGal, which is a good data fit.

Line 2

The Line 2 gravity model was also constructed using GYMSYS within the Oasis Montaj program (Figure 36) and follows seismic Line 2 (Figure 29). I used the Line 2 seismic model as a constraint for constructing this gravity model. The dimensions of the model were 350 km long by 70 km deep. Similar methods were used to construct the Line 2 profile as the Line 1 profile. The upper part of the model consists of low-density materials that represent sediments and volcanics, and this material thins to the north. This layer covers Basin and Range structures in the southern part of the profile. Denser material is located under the southern Harney Basin. The upper crustal densities are representative of the slower velocity felsic material with minor variations in density values. A block of less dense material can be found under the horst and graben structures in the south. The lower crust shows a lateral density decrease from south to north. This corresponds to the thickening crust towards the north. The pink layer is dense material that is interpreted as underplating, which is obviously too thin to be resolved by the gravity data alone. This model also has a fit error of 2.2 mGal.

INTEGRATING SEISMIC AND GRAVITY MODELS

2D full-waveform Modeling

The final step of analyzing the HLP data was to test the robustness of the model. A model for Line 1 model that integrates the raytrace model (Figure 26) and the Line 1 density model (Figure 35). Using the commercial 2D full waveform modeling software TESSERAL® (Tesseral Technologies Inc., http://www.tesseral-geo.com/), synthetic seismograms for shotpoints 11,12, 13, 14, 15 16, and 17 were generated. TESSERAL® is designed for interactive analysis and verification of depth-velocity models. The program simulates P-wave propagation in a heterogeneous medium utilizing a finite-difference calculation using a staggered grid approach. The crustal phases (Figure 14) are compared to the real data for similarities and differences in waveform, amplitude, and frequency spectrum. Then travel-time picks were made on the synthetic seismograms. These picks were used to ray trace model, and finally an inversion computes the final synthetic model in the Zelt program.

The first step in creating this model in TESSERAL was to reconstruct the boundaries node by node to match the velocity model and the far offsets were modeled after the density model. The model bounds are the same as the seismic and density models, 410 km long by 50 km deep. As mentioned before, the density model helps provide information about the far offset boundaries, velocities, and densities unseen by lack of ray coverage. Next nodes with density and velocity values were paced in the same locations as the velocity nodes in the seismic model. A total of 514 receivers spaced at 800 m spacing and 7 shotpoints were modeled to simulate the acquisition parameters.

Synthetic seismograms for all Line 1 shotpoints were generated. For all of the shotpoints, I used a 5 Hz Ricker wavelet with a spatial gird size of 0.5 km to model the P-wave propagation. The run time for shot point 14 was 01:51:10 and for shotpoint 16 was 1:46:19. Refer to Appendix B for the other seismograms. The synthetics generated in TESSERAL were then exported as an IBM format SEG-Y files and imported into PROMAX®. A flow was used to give each trace the correct offset and output an IEEE format SEG-Y file. The new SEG-Y file was then displayed in zp (Figures 37 and 38).

Figure 37 shows the synthetic seismogram generated for SP 14 and Figure 38 shows the synthetic seismogram generated for SP 25. The synthetic data contains a lot of reverberations and very strong ground roll but displays the main arrivals observed in the field data. However, the delay times for the Pg phase do not agree as well as would be expected. Some of the similarities that we do see are the shared Pn crossover locations, the weak amplitudes of the PcP, and the strong amplitudes of the PmP. In order to further investigate the resolution of the field data similar workflow was used to model the travel-time picks made from the synthetic seismograms (Figure 16). I used the Line 1 model (Figure 26) as the starting model for the raytrace modeling. RMS values for the final model before inversion were as follows: Pg (0.271), PcP (0.101), PmP (0.132), and Pn (0.211). An inversion was then run to calculate the final model (Figure 39) with improved RMS values: Pg (0.101), PcP (0.054), PmP (0.70), and (0.177) Pn. Figure 40 shows the resolution diagram for synthetic Line 1 after the inversion. The resolution in all layers is good, and, as would be expected, compared to the resolution diagram for Line 1 (Figure 27), there is better ray coverage in the deeper layers in the model.

DISCUSSION

Scientific motivation

An integrated approach was used when analyzing the wide-angle reflection/ refraction and gravity data collected from the High Lava Plains (HLP) experiment. These data were collected to provide the first high-resolution images of crustal structure across the HLP to better understand the structure and evolution of the region. Two methods of seismic modeling were applied: 1) forward modeling using the asymptotic ray theory algorithm of *Zelt* [1999], and 2) full waveform modeling using a finite difference algorithm. As part of the overall High Lava Plains effort, we anticipate that the seismic velocity models derived in this study will ultimately be integrated with passive source data to refine current mantle tomographic models derived from the passive source portion of the project [e.g., *Roth et al.,* 2008].

The asymptotic ray theory modeling algorithm requires that interfaces that reflect and refract rays extend entirely across the model, even though layers may pinch out or may be discontinuous. The software provides features that allows for complexities such as the isolated mid-crustal body in the model for Line 2 (Figure 28). However, I do not believe that the mid-crustal interface shown for Line 1 in Figure 25 is actually continuous, and instead I believe that it is probably a different reflector in northwestern, central, and southeastern portions of the model. This discontinuous nature is shown in Figure 26.

During the modeling process, gravity data were also modeled along with the seismic models as constraints in order produce integrated models in which both P-wave velocity and density were represented. Because the average source spacing was ~60 km, narrow features such horst blocks could not always be resolved by the seismic data alone. However, the closely spaced gravity data that was collected along the profiles could resolve such features and could also constrain the seismic models at each end where the ray geometries produced triangular zones with no ray coverage (Figures 25 and 28). Even within the interior portions of the seismic models, gravity data provided useful constraints on deep structure in areas of sparse ray coverage. This integrated approach involved a series of iterations between the seismic and gravity models in order to produce matching P-wave velocity and density models.

The modeling process did begin with the seismic modeling, and the initial seismic models were used to constrain the initial density models via a modern Vp versus ρ relationship [*Brocher et al.*, 1995]. For each line, the initial seismic model was used to derive the starting model for the gravity analysis. However, the gravity modeling revealed some shallow structures such as the apparent horst blocks in the northwest portion of the model for Line 1 (Figure 16), and these structures were incorporated into the seismic model. Some of the lack of continuity of seismic constraints on the structure in the middle crust due to poor ray coverage (Figures 26 and 29) could be constrained by the gravity data. Once the first iteration of gravity modeling was complete, the new results were incorporated into the seismic models, which were in turn, iterated by trial and error ray tracing and inversion. The updated velocity models were then translated into density models, which only required minor adjustments to fit the data satisfactorily (Figures 35 and 36). A final integration of the gravity and seismic models was used to derive interpretative cartoons that illustrate the main features of the crustal structure beneath the HLP for Line 1 (Figure 42) and Line 2 (Figure 43).

The ray coverage diagrams (Figures 21-22) provide a qualitative avenue to assess the uncertainty of the seismic model, and the inversion routine provides quantitative information on resolution (Figures 27-30). However, I also tried a new approach to assess resolution using full-waveform modeling. I constructed a model with the identical velocity and density structure as my final integrated models for Line 1 after inversion (Figure 26) and using the same acquisition parameters as in the actual field experiment, a record section of synthetic seismograms was generated for each shot along Line 1. Following the same steps as in the modeling of the field data, the synthetics were then picked, and the travel times were forward modeled to compare the velocity structure for the final Line 1 model before inversion (Figure 26). An inversion was run on the resulting velocity model to improve the RMS values, and the final synthetic model was obtained (Figure 39). Although the synthetic data was not identical to the field data, the final model produced showed very good agreement with the model created from the field data (Figures 29 and 39). The synthetic data can be though of as the result of an "ideal" field experiment in which noise is minimal and all shots were recorded by all stations. Thus, the match of the models derived from the "ideal" and actual field supports my assertion that the integrated models produced are well resolved.

Sedimentary and Volcanic Cover

The upper two layers in the seismic and density models indicate a thick (2-7 km) cover of volcanics and sediments blankets the High Lava Plains and the northern Basin and Range to the south. In the summer of 1977, Exploration Logging drilled a well in the

Harney Basin. This well reached a depth of 2.3 km, and confirms the lithology of the Harney Basin fill to be sediments, ash, and basalt. This cover thins northward toward the accreted terrains and southeastward toward western Idaho, and it is thickest (7 km) in the Harney Basin.

The first of these layers has velocities ranging from 3.0 - 5.0 km/s and a density of 2.2 gm/cc. This layer covers horst and graben structures in the western part of Line 1 (Figure 26), in the vicinity of Jordan Valley to the east (Figures 3 and 6), and in the southern part of Line 2 where the line is clearly in the Basin and Range. The structures to the east could be related to the Oregon-Idaho graben system (Figure 3)

The second of these layers has greater variations in velocity and density in this layer. Velocities in this layer along Line 1 (Figure 26) range from 4.0 km/s in the west to 6.0 km/s in the east, with average velocities below the Harney Basin being about 5.8 km/s. The average density of this layer is 2.5 g/cm^3, and pockets of denser material (2.8 gm/cc) lie beneath the Harney Basin in the vicinity of Diamond Craters and to the east in the vicinity of the Jordan Craters near Jordan Valley (Figures 3 and 6). Thus, these pockets of denser material are interpreted to be mafic material related to these young volcanic centers. In the Basin and Range along Line 2, the second layer has an average velocity of 5.1 km/s to 5.6 km/s, and similar velocities are found north of the Harney Basin as the accreted terrains are approached.

Crystalline Upper Crust

Crystalline upper crust as defined here lies between the bottom of the upper two layers of sedimentary and volcanic cover, and the discontinuous PcP reflector (Figures 26 and 29). This layer has an average velocity of 6.0 km/s to 6.2 km/s with density values that vary between 2.70 g/cm^3 and 2.78 g/cm^3 (Figures 35 and 36). Overall, these values do not indicate the presence of large-scale magmatic modification of the upper crust such as seen in the Eastern Snake River Plain (Figure 41). However, there is a high velocity zone below the southern portion of the Harney Basin (Figures 26, 29, and 43) that could be due to magmatic modification of the upper crust associated with Diamond Craters or a caldera that could be related to the source of the extensive Rattlesnake Tuff that has been interpreted to have a source in this vicinity [*Streck and Grund*er, 2008]. Near the southern end of Line 2, a diamond-shaped body was required to fit the gravity and seismic data. Its seismic velocity and density are slightly higher than the adjacent material to the south and north, and its upper surface is a clear reflector. There is no surface expression of this feature that can be detected in geologic maps. However, *Barton et al.* [1988] suggest that this area is within a region where more than 50% of the upper crust consists of Cretaceous granitic material. Thus, I have interpreted this body to be a zone of intraplating (Figure 43).

Lower Crust and Moho

The lower crust is the region between the discontinuous PcP reflector and the Moho and has P-wave velocities of 6.4 to 7.3 km/s and densities that range from 2.81 to 3.0 g/cm^3 (Figures 26, 29, 35, and 36). Along Line 1, velocities and densities increase to the southeast while the crust thickens (32 km to 37 km) (Figures 26 and 35). The domal feature lying between 300-350 km along this line is near the Jordon Craters, but this is a small-volume Quaternary feature. In a broad sense, this feature lies under the northwest portion of the Owyhee Plateau (William Hart, personal communication). Thus, this crustal feature is most likely related to the extensive volcanism in this region and has been interpreted a zone of intraplating (Figure 42). The southeast end of Line 1 lies in close proximity to the interpreted position of the 0.706 Sr isotope line (Figure 3), and thus the entire line can be thought of as lying west of cratonal North America. The lowermost crustal structure along Line 1 suggests that a thin 7.xx layer developed under the southeastern portion of the line and that underplating has occurred (Figure 42). In spite of many geological similarities, the crustal structure resolved in this study very different from the crustal structure of the ESRP (Figure 38) [e.g., *Sparlin et al.,* 1982]. This fact is evident in the gravity maps (Figures 31-33) that show a large linear gravity high associated with the Snake River Plain and no gravity high following the HLP trend.

The NW-SE thickening of the crust along Line 1 (Figures 26 and 42) indicates that some crustal thinning has occurred in the western portion of the HLP, which is in agreement with the results of *Catchings and Mooney* [1995]. The extensive cover of volcanics and sediments is several kilometers thinner to the south in the Basin and Range [*Lerch et al*., 2007], but otherwise the crustal structure in the western portion of Line 1 and in the Basin and Range to the south is very similar. Based on geological observations, this is no surprise and supports the assertion that HLP is part of the Northern Basin and Range. The southern portion of Line 2 also crosses the northernmost Basin and Range and ties to the *Lerch et al.* [2007] model as part of the original HLP experiment design. The lower crust beneath the Basin and Range has values of 6.8 km/s with Moho depths of ~28 km, and these result agree well with the velocity model of *Lerch et al.* [2007] near their Shotpoint 2, which is the tie point between the two experiments.

From south to north long Line 2, the Moho thickens abruptly beneath the Steens Mountain region to ~38 km, which suggests there is a possibly a crustal root for this impressive mountain range. However, it is the lower crust that accounts for most of this thickening. The velocity and density also increase as the lower crust thickens (Figure 29 and 36). Throughout the region, the Moho depths are broadly consistent with the High Lava Plains receiver function results [*Eagar et al.,* 2010] (Figure 44), which adds a planned element of three-dimensionality to the combined results of the HLP seismic experiments.

Tectonic and Geologic Implications

The HLP region geologic and tectonic attributes with both the neighboring Snake River Plain and the Basin and Range. The residual gravity map in Figure 33 shows the Snake River Plain as a strong gravity high that is due to massive mafic magmatism in the upper crust, while HLP is neither associated with a distinct gravity anomaly nor high velocity material in the upper crust. In fact, the crustal structure of most of the HLP region is similar to the Basin and Range to the south. These contradictions suggest that little magmatic modification in the upper crust has occurred in the HLP region, even though similarities in the shallow structure of the HLP and the ESRP, which indicates that as the rhyolite trends migrated across the ESRP and HLP, the interactions with the upper crust were very different.

The origin of the crust in the HLP region is a fundamental scientific question, and I have found that the crust in this region to surprisingly similar to that in the Northern Basin and Range. Thus, I would characterize the HLP region crust as being typical of extended continental areas with modest magmatic modification in the crust. As shown by

Carlson and Hart [1987], the geochemistry of the mid-Miocene flood basalts provides evidence for extensive crystal fractionation so signification volumes residues must have been produced. My results do not preclude some magmatic modification of the crust (Figures 42 and 43) but do suggest that most of this residue must be in the thin underplated zone along the eastern portion of Line 1 or the uppermost mantle. Despite the HLP being located on accreted material, my results indicate that the HLP region was once a microcontinent(s) and was not originally accreted oceanic arc material because its crustal structure is so typical of extended continental regions (Figures 42 and 43).

When comparing the seismic models (Figure 26 and Figure 27) to the findings of [*Lerch et al*., 2007] (Figure 9), there are differences in the amount of sediment and volcanics that are seen at the surface. Had the [*Lerch et al.,* 2007] model had upper layer of sediment, it would look almost identical to the HLP model, suggesting that the HLP is part of the Northern Basin and Range. It is plausible that there was enough extension to prevent large amounts of magmatic modification in the mid-crust. In addition to the lack of extension, there is the 0.706 boundary to the east that means the ESRP is located on relatively young continental crust. This change in geochemistry might also hold clues as to why the magmatic interactions with the crust to differ.

CONCLUSIONS AND FUTURE WORK

The High Lava Plains (HLP) controlled-source seismic experiment covered the HLP region and adjacent Basin and Range and extended to the edge of cratonal North America on the east and to the accreted terrains of the Blue Mountains to the north. The main goal of my study was to produce integrated models for Lines 1 and 2 of the experiment. P-wave velocity models were generated by using raytrace modeling and then modified by integration with gravity modeling and tested by comparison with full waveform modeling.

This study concludes that the crust is similar to that of the Basin and Range in that it is thinner than surrounding continental crust and is overlain by a 5-7 km thick layer of sediments and volcanics. The upper crust is also composed of crystalline material similar to typical continental crust that implying the origin of the crust beneath is not due to an accreted island arc(s). This result provides additional evidence that most of the HLP region is part of the Northern Basin and Range. The HLP is obviously similar to the SRP in terms of its magmatic history but the similarities end below the uppermost crust. Based on the gravity and seismic models I derived, there is also evidence for underplating in the lower crust beneath the eastern portion of HLP. In addition, a zone of magmatic modification was identified beneath the southern Harney Basin suggesting possible evidence for a caldera system beneath this area. Further 3-D seismic modeling will be needed to evaluate this possibility. The average crustal velocity and density structure is somewhat higher than in the adjacent Basin and Range suggesting some magmatic modification in the lower crust but not as much as might be expected given the voluminous surface volcanism. It is plausible that the extension in the HLP reduced the amount of magmatic modification as compared to the relatively unextended SRP. Additional studies combining advanced petrologic studies, geochronology, geodynamic models, and passive source seismic images are needed to fully understand the evolution of the HLP, and these studies are part of the overall HLP region.

REFERENCES

Armstrong, R. L., Taubeneck W. H., and P.O Hales, (1977), Rb-Sr and K-Ar geochronometry of Mesozoic granitic rocks and their Sr isotopic composition, Oregon, Washington, and Idaho, *Bull. Geol. Soc. Am.*, *88*, 397-411.

Barton, M., D. Battles, G. Debout, R. Capo, J. Christensen, S. Davis, R. Hanson, C. Michelsen, and H. Trim (1988), Mesozoic contact metamorphism in the western United States, in Ruby Colloquium on Metamorphism and Crustal Evolution of the Western United States, vol. 7, Metamorphism and Crustal Evolution of the edited by W. Ernst, pp. 110–178, Univ. of Calif., Los Angeles.

Benford, B., Crowley, J., Schmitz, M., Northrup, C. J., and B. Tikoff (2010), Mesozoic magmatism and deformation in the northern Owyhee Mountains, Idaho: Implications for along-zone variations for the western Idaho shear zone. *Lithosphere, 2*, 93-118.

Blakely, R. J. (1996), *Potential Theory in Gravity and Magnetic Applications*. New York, Cambridge University Press.

Braile, L. W. and R. B. Smith (1974), Guide to the Interpretation of Crustal Refraction Profiles. *Geophys. J. R. Astr. Soc.*, *40*, 145-176.

Braile, L. W., R. B. Smith, Ansorge, J., Baker, M. R., Sparlin, M.A., Prodehl, C., Schilly, M. M., Healy, J. H., Mueller, S.T., and Olsen, K.H. (1982), The Yellowstone-Snake River Plain seismic profiling experiment: Crustal structure of the eastern Snake River Plain. *J. Geophys. Res,, 87*, B4, 2597-2609.

Brueseke, M. E., Heizler, M.T., Hart, W.K., and Mertzman, S.A. (2007), Distribution and geochronology of Oregon Plateau (U.S.A.) flood basalt volcanism: the Steens Basalt revisited. *J. Volcan. Geotherm. Res., 161***,** 187-214, doi:10.1016/j.jvolgeores.2006.12.004

Camp, V. E., and M. E. Ross (2004), Mantle dynamics and genesis of mafic magmatism In the intermontane Pacific Northwest, *J. Geophys. Res*., *109*, B08204, doi:10.1029/2003JB002838.

Camp, V. E., M. E. Ross, and Hanson, W.E. (2003), Genesis of flood basalts and Basin and Range volcanic rocks from Steens Mountain to the Malheur River Gorge, Oregon. *Geo. Soc. Am. Bull., 115*, 105-128.

Carlson, R. W. (1991), Physical and chemical evidence on the cause and source characteristics of flood basalt volcanism. *Austral. J. of Earth Sci.*, *38*, 5, 525 – 544, doi: 10.1080/08120099108727989.

Catchings, R. D. and W. D. Mooney (1988), Crustal Structure of East Central Oregon: Relation Between Newberry Volcano and Regional Crustal Structure. *J. Geophys. Res., 93***,** B9, 10,081-10,094.

Christensen, N. I. and W. D. Mooney (1995), Seismic velocity structure and composition of the continental crust: A global view. *J. Geophys. Res., 100*, B7, 9761-9788.

Dickinson, W. R. (2004), Evolution of the North American Cordillera*. Annu. Rev. Earth Planet. Sci., 32*, 13–45, doi: 10.1146/annurev.earth.32.101802.120257

Dickinson, W. R. (2006), Geotectonic evolution of the Great Basin. *Geosphere, 2*, 353-368.

Eagar, K. C., M. J. Fouch, D. E. James, and R. W. Carlson (2011), Crustal structure beneath the High Lava Plains of eastern Oregon and surrounding regions from receiver function analysis, *J. Geophys. Res., 116*, B02313, doi:10.1029/2010JB007795.

Hart, W. K., and R. W. Carlson (1987), Tectonic controls on magma genesis and evolution in the northwestern United States, *J. Volcanol. Geotherm. Res.*, 32, 119– 135.

Jordan, B. T., Grunder, A.L, Duncan, R. A., Deino, A. L. (2004), Geochronology of age-progressive volcanism of the Oregon High Lava Plains: Implications for the plume interpretation of Yellowstone. *J. Geophys. Res. 109,* B10, B10202.

Keller, G. R., T. G. Hildenbrand, R. Kucks, M. Webring, A. Briesacher, K. Rujawitz, A. M. Hittleman, D. J. Roman, D. Winester, R. Aldouri, J. Seeley, J. Rasillo, T. Torres, W. J. Hinze, A. Gates, V. Kreinovich, and L. Salayandia. (2006), A community effort to construct a gravity database for the United States and an associated Web portal. In: A. K.Sinha, Editor. *Geoinformatics: Data to Knowledge*, Geological Society of America Publ., Boulder, Colorado, 21-34.

Lerch, D. W., S. L. Klemperer, J. M. G. Glen, D. A. Ponce, E. L. Miller, and J. P. Colgan (2007), Crustal structure of the northwestern Basin and Range Province and its transition to unextended volcanic plateaus, *Geochem. Geophys. Geosyst.*, *8*, Q02011, doi:10.1029/2006GC001429.

Long, S. P., Link, P. K., Janecke, S. U., and Rodgers, D. W. (2004), Geologic map of the Henderson Creek Quadrangle, Oneida County, Idaho, Idaho Geological Survey.

McQuarrie, N. and B. P. Wernike (2005), An animated tectonic reconstruction of southwestern North America since 36 Ma. *Geosphere, 1*, 147-172.

Pezzopane, S. K. and R. J. Weldon (1993), Tectonic role of active faulting in central

Oregon. *Tectonics, 12***,** 5, 1140-1169.

Roth, J.B., Fouch, M.J., James, D.E., and R.W. Carlson (2008), Three-dimensional seismic velocity structure of the northwestern United States, *Geophys. Res. Lett*., 35, L15304, doi:10.1029/2008GL03466.

Severinghaus, J. a. A., T. (1990), Cenozoic geometry and thermal condition of the subducting slabs beneath western North America. *Basin and Range extensional tectonics near the latitude of Las Vegas, Nevada* edited by B. P. Wernicke, *Geological Society of America Memoir, 176*, 1-22.

Shervais, J. W., S. K. Vetter, Hanan, B. B. (2006), Layered mafic sill complex beneath the eastern Snake River Plain: Evidence from cyclic geochemical variations in basalt. *Geology, 34*, 365-368, doi: 10.1130/G22226.1.

Smith, R. L., and Luedke, R. G. (1984), Potentially active volcanic lineaments and loci in western conterminous United States. in *Explosive Volcanism: Inception, Evolution, and Hazards*. edited by J. R. Boyd, National Academy Press**,** 47–66, Washington, D.C.

Sparlin, M. A., L. W. Braile, and Smith, R. B. (1982), Crustal structure of the eastern Snake River Plain determined from ray trace modeling of seismic refraction data. *J. Geophys. Res., 87*, B4, 2619-2633.

Streck, M. and A. Grunder (2008), Phenocryst-poor rhyolites of bimodal, tholeiitic provinces: the Rattlesnake Tuff and implications for mush extraction models. *Bull. Volcan., 70*, 3, 385-401.

Streck, M. J. and A. L. Grunder (1995), Crystallization and welding variations in a widespread ignimbrite sheet; the Rattlesnake Tuff, eastern Oregon, USA. *Bull.*

Volcan., 57, 3,151-169.

Talwani, M., J. L. Worzel, and M. Landisman (1959), Rapid gravity computations for two-dimensional bodies with application to the Mendocino submarine fracture zone, *J. Geophys. Res.*, *64*,1, 49–59.

Wagner, L.S., D. Forsyth, M. Fouch, D. James (2010), Detailed three-dimensional shear wave velocity structure of the northwestern United States from Rayleigh wave tomography *Earth and Planetary Sci. Lett.*, *299*, 273-284. doi: 10.1016/j.epsl.2010.09.005

Wells, R. E. (1990), Paleomagnetic Rotations and the Cenozoic Tectonics of the Cascade Arc, Washington, Oregon, and California. *J. Geophys. Res. 95,* B12, 19, 409-419.

Wells, R. E., Weaver, C. S., and Blakely, R. J. (1998), Fore-arc migration in Cascadia and its neotechtonic significance. *Geology, 26,* 8, 759-762.

Wernike, B. P. (1992), Cenozoic extensional tectonics of the U.S. Cordillera. *The Cordilleran Orogen: Conterminous U.S., The Geology of North America, G-3.* B. edited by C. Burchfiel, P. W. Lipman and M. L. Zoback. pp. 553-582, GSA, Boulder, Colorado.

Wyld, S. J. and J. E. Wright (2001), New evidence for Cretaceous strike-slip faulting in the United States Cordillera and implications for terrane-displacement, deformation patterns, and plutonism. *Am. J. Sci.,* 301, 150-181. doi: 10.2475/ajs.301.2.150.

Wyld, S. J. and J. E. Wright (2007), Alternative tectonic model for Late Jurassic through Early Cretaceous evolution of the Great Valley Group, California. *Geol. Soc. Am. Spec. Paper, 419*, 81-95.

Zelt, C. A. (1999), Modeling strategies and model assessment for wide-angle seismic traveltime data. *Geophys. J. Int., 139*, 183-204, doi:10.1046/j.1365-246X.1999.00934.x.

Zelt, C. A. and R. B. Smith (1992), Seismic traveltime inversion for 2-D crustal velocity structure. *Geophys. J. Int., 108*, 16-34, doi:10.1111/j.1365-246X.1992.tb00836.x.

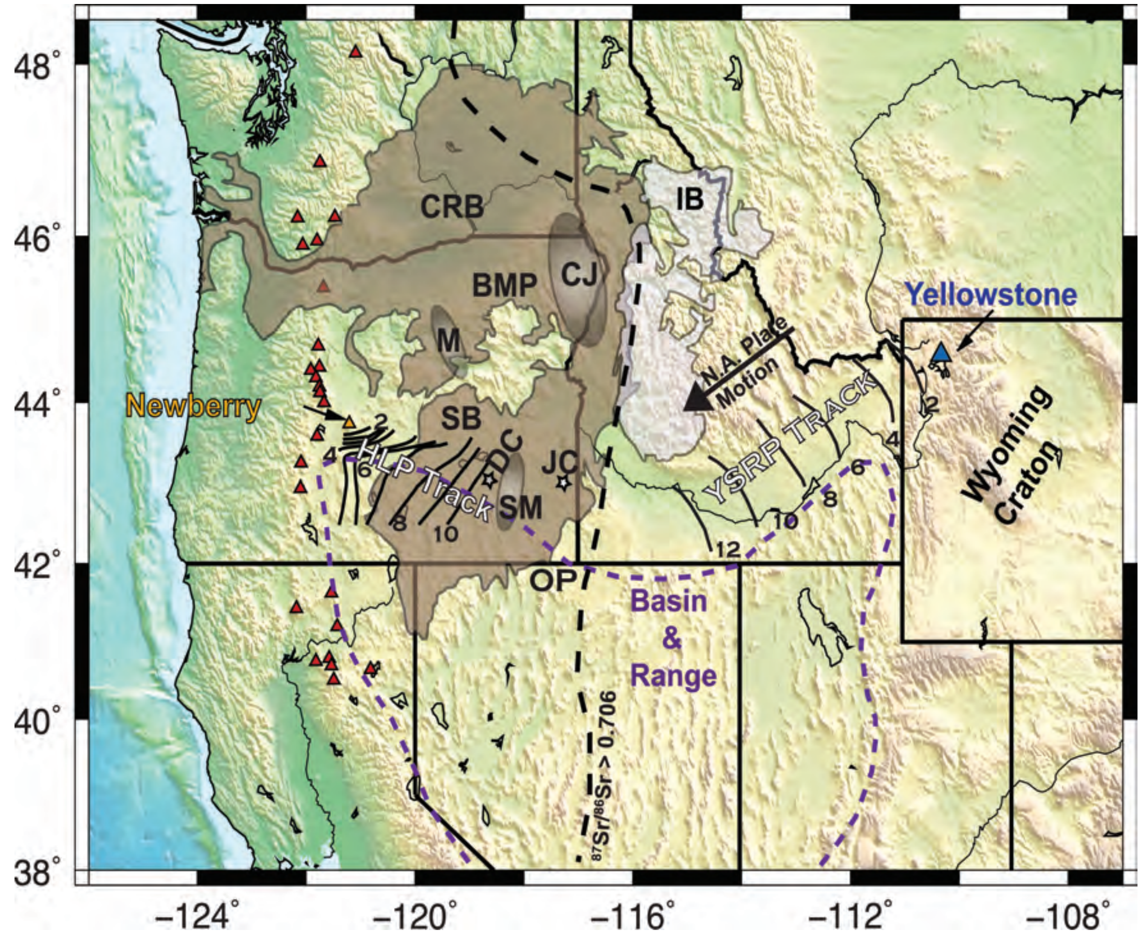

Figure 1. [from *Wagner et al.,* 2010] Geologic map of the northwestern United States: the brown shaded area shows the extent of the Columbia River (CRB) and Steens Mountain (SB) flood basalts The white shaded area represents the Idaho Batholith (IB) . Also shown are the locations of the Blue Mountain Province (BMP), the Chief Joseph (CJ), Monument (M) and Steens Mountain (SM) dike swarms (shaded ovals), and the Owyhee Plateau (OP). Basaltic centers Diamond Craters (DC) and Jordan Craters (JC). *T*he 0.706 line is shown is shown as a black dashed line. The boundaries of Basin and Range extension are shown with a purple dashed line. The Newberry and Yellowstone volcanic tracks are show in black with ages in millions of years.

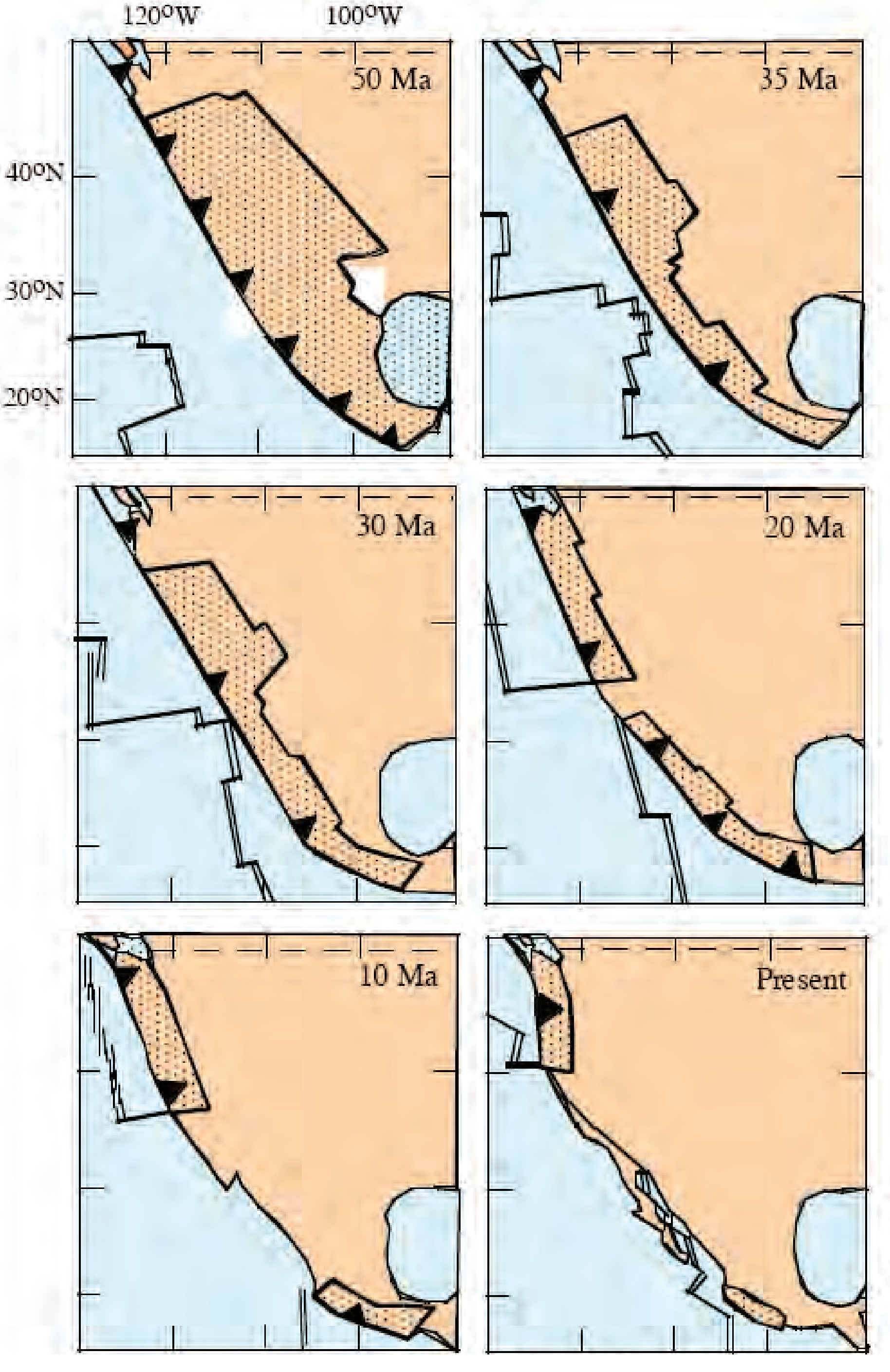

Figure 2. The evolution of the geometry of the subducting Juan de Fuca plate from 50 Ma to present [*Severinghaus and Atwater,* 1989].

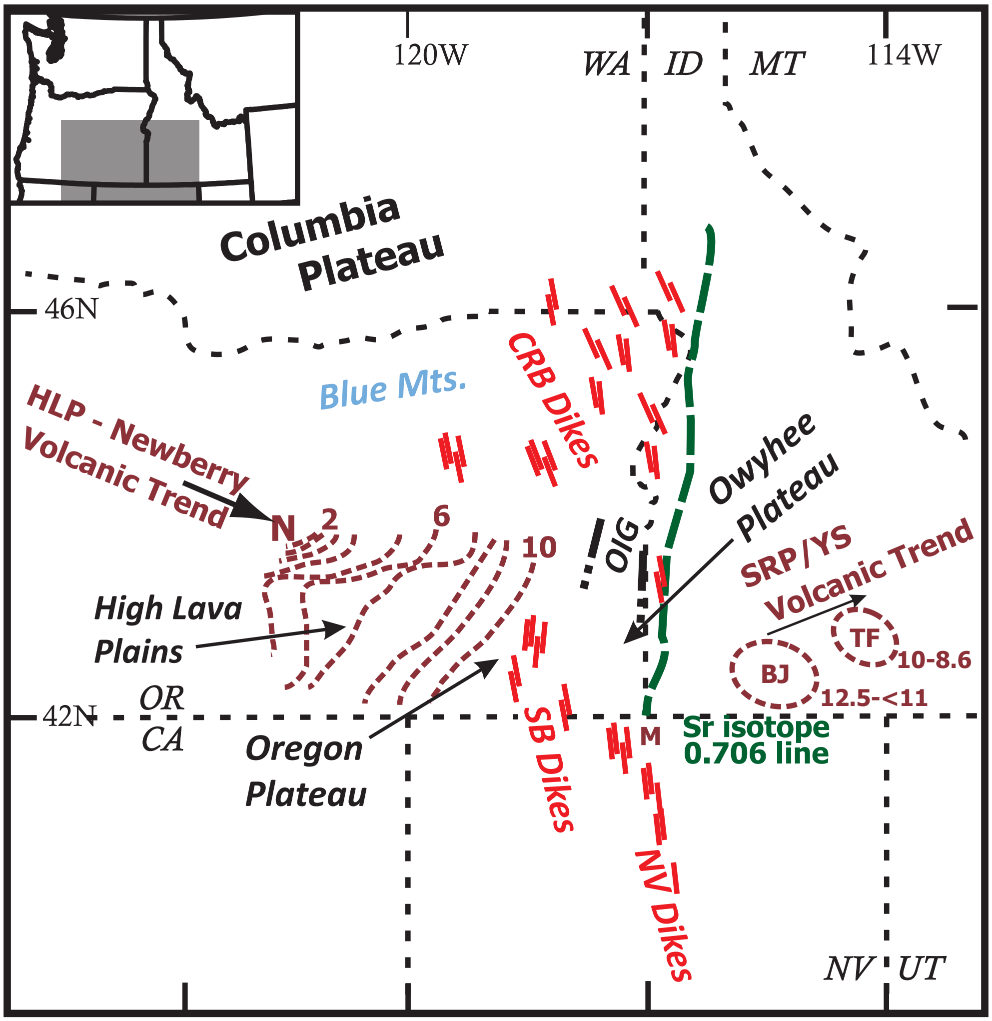

Figure 3. Modified from [*Brueseke et al,* 2007], [*Benford et al.,* 2010], and [Personal communication with *Bill Hart and Basil Tikkoff*] Index map showing the geologic setting of the region. The High Lava Plains is situated between the SR/YS (Snake River/Yellowstone) volcanic track that includes the lies the Bruneau-Jarbidge (BJ) and Twin Falls (TF) volcanic fields and the HLP-Newberry trend (brown)are bounded to the north by the Blue Mountians and the Columbia Plateau, to the east lie the Columbia River Basalt (CRB), Steens Basalt (SB), and Nevada (NV) feeder dikes (red); in adition to the 0.704 and 0.706 Sr isotope lines (green) and the Oregon- Idaho graben (OIG) and OwyheePlateau (black).

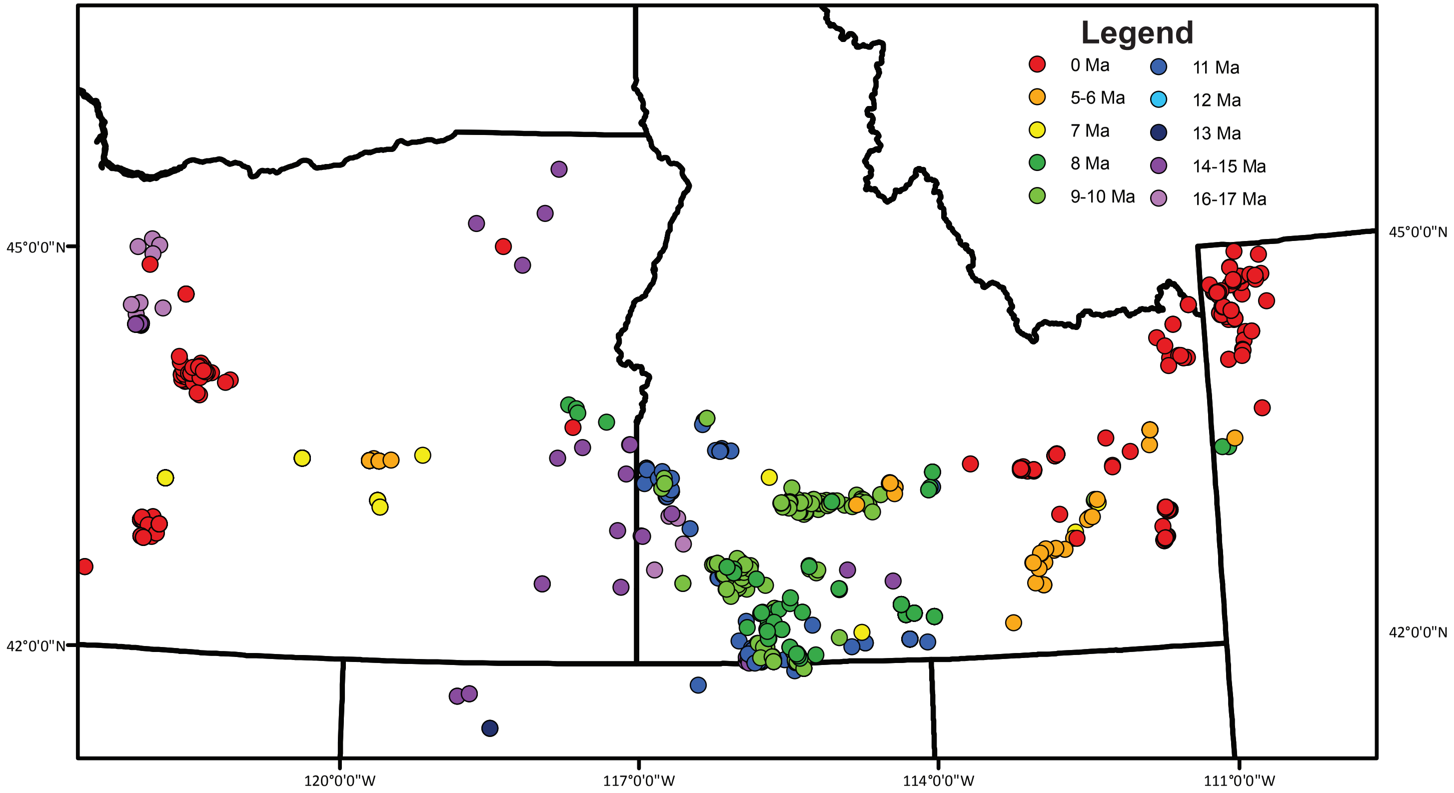

Figure 4. Map of rhyolite age progression tends from 17 Ma to the present based on radiometric dating. Data is from the NAVDAT website.

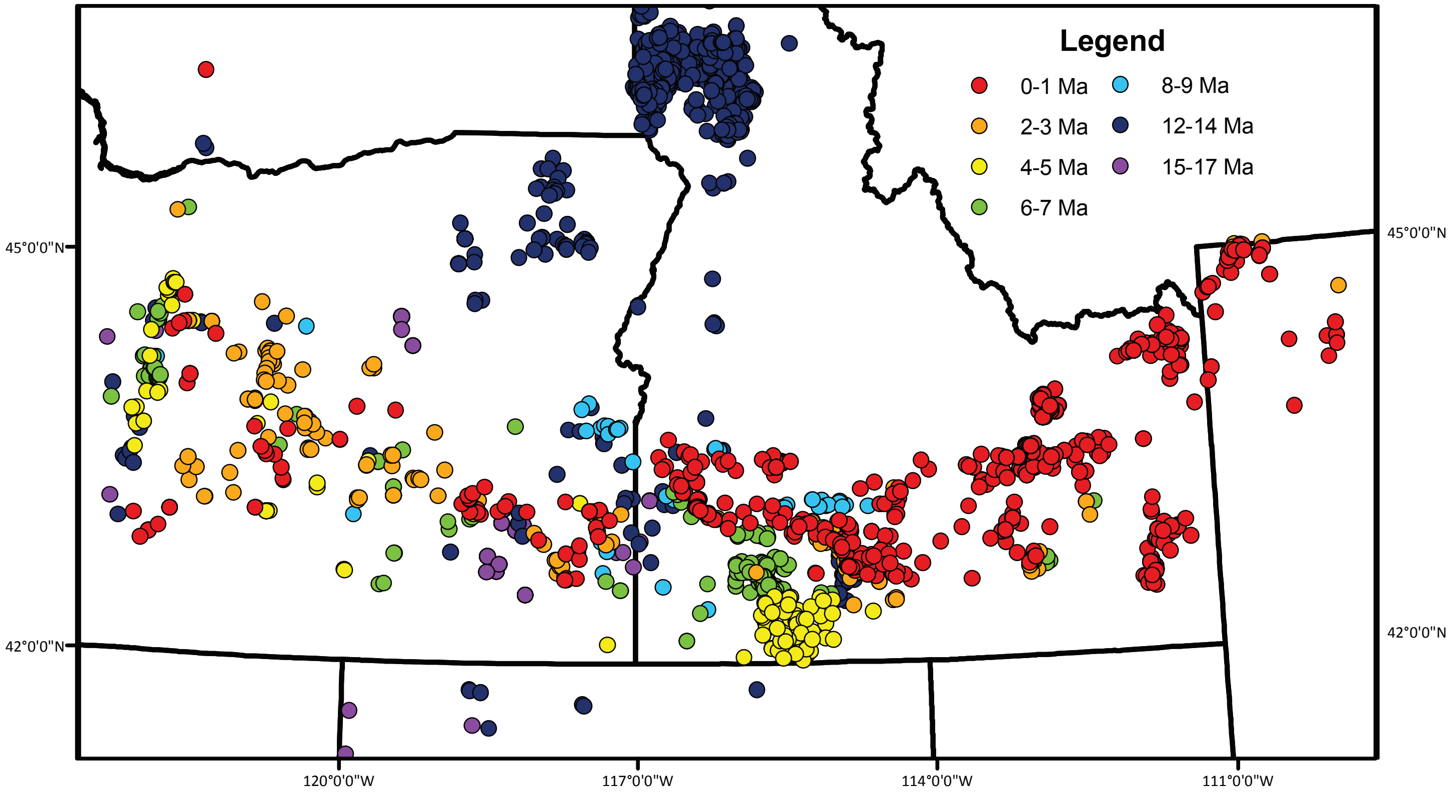

Figure 5. Map of basalt tends from 17 Ma to the present based on radiometric dating. Data is from the NAVDAT website.

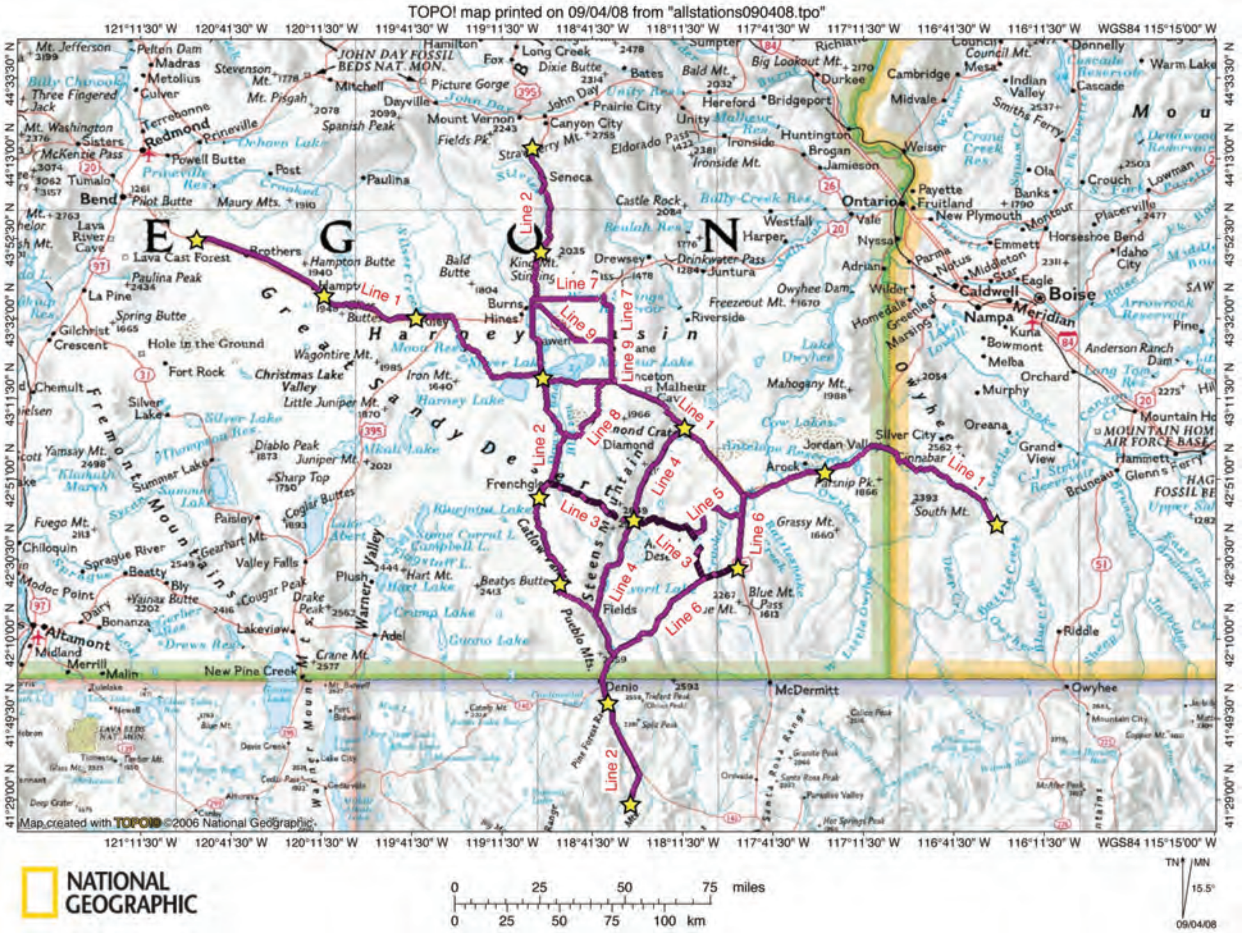

Figure 6. Index map of the High Lava Plains controlled-source seismic experiment. Shot points are shown by yellow stars and the single component recievers are show as purple dots and the 3C line is shown by black and purple dots.

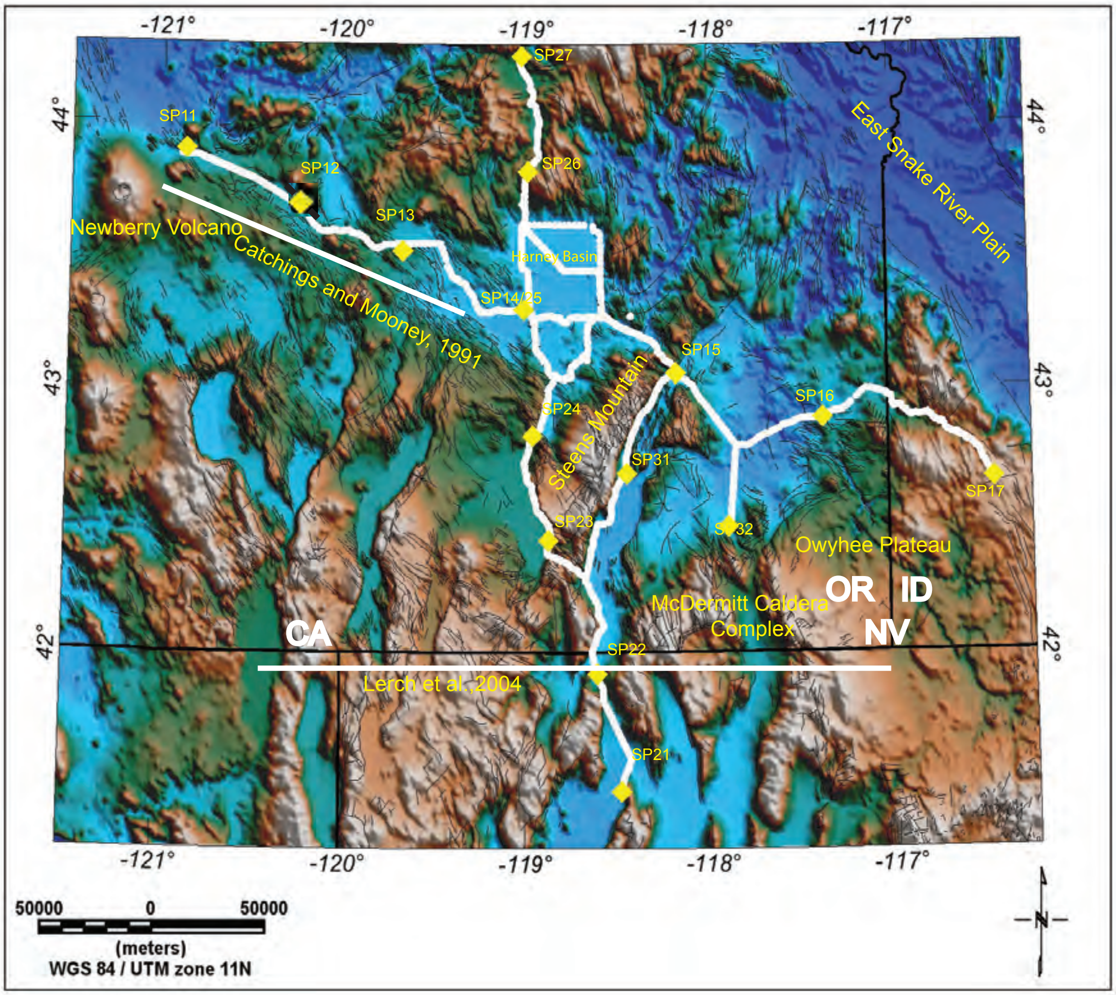

Figure 7. DEM index map of High Lava Plains. Previous seismic experiments shown as white lines, reciever locations in black, and shotpoints shown as yellow diamonds.

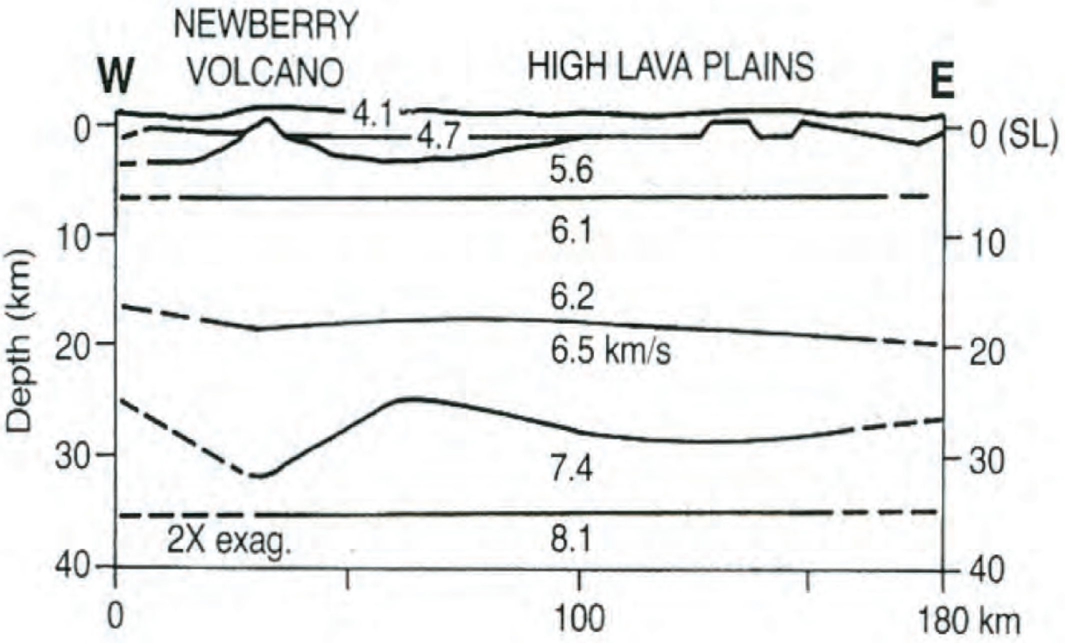

Figure 8. Seismic velocity model from [*Catchings and Mooney,* 1991]. This model was used as the starting model for the High Lava Plains Line 1 profile.

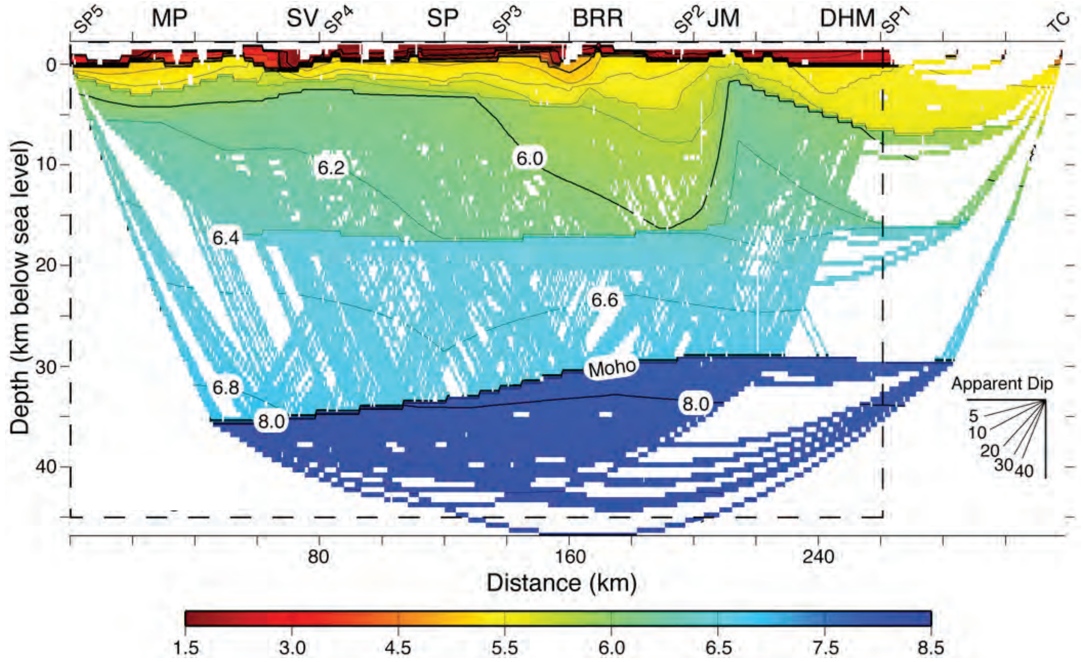

Figure 9. P-wave velocity model from [*Lerch et al..,* 2007]. In the vicinity of SP2 of this model was used as the starting model for the south end of the High Lava Plains Line 2.

Figure 10. Field photo showing the drilling operations for the High Lava Plains Controlled- source seismic experiment. The shot holes were filled with 1-ton of emulsion gel (red), 60 ft of angular gravel (blue), and toped with cuttings and sediment (orange).

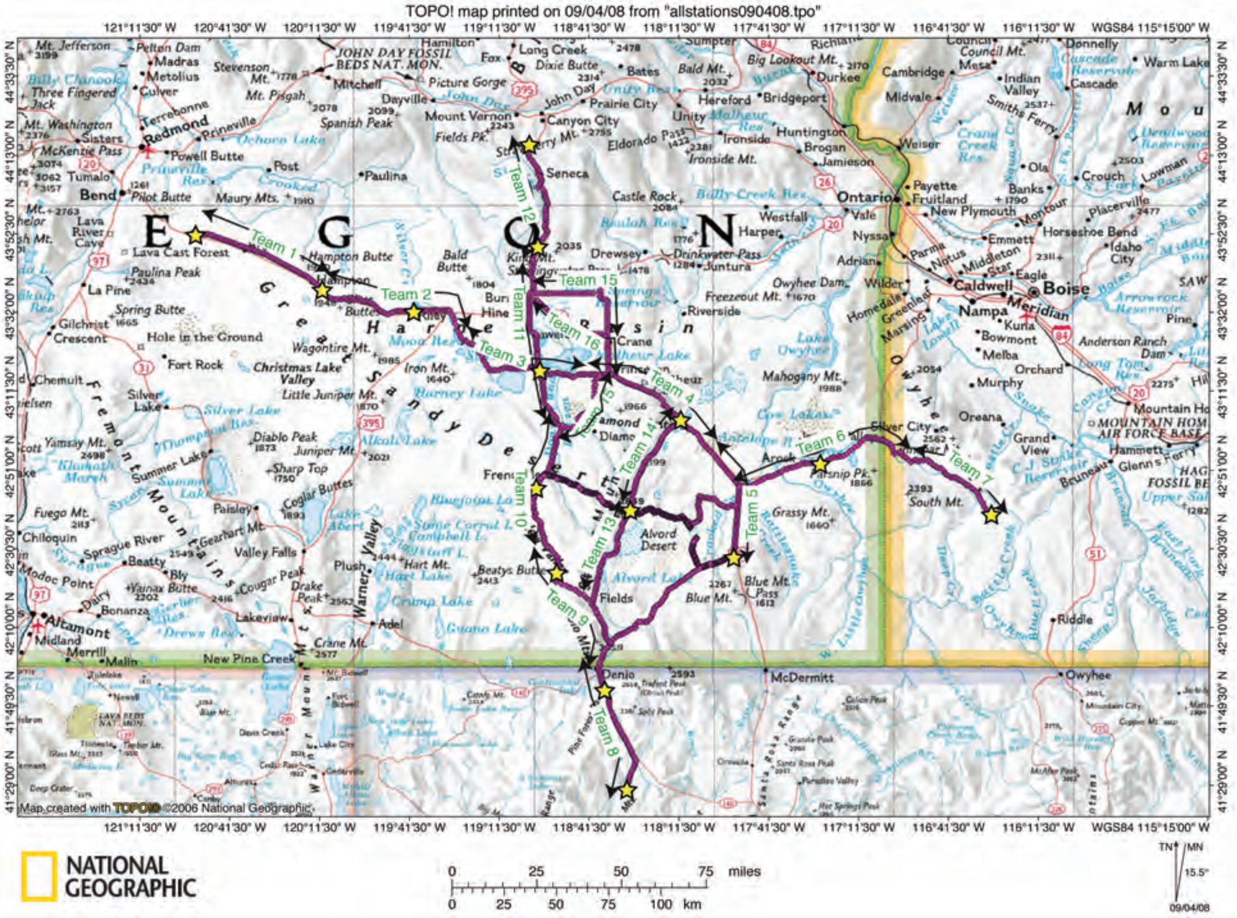

Figure 11. Index map that shows the aquisition design of the High Lava Plains controlled experiment with the breakdown of which team deployed Texans in a given area.

Figure 12. Photo of the Texan receivers used during the controlled-source experiment.

Figure 13. Photo of the “Lunchbox” used to record Texan locations.

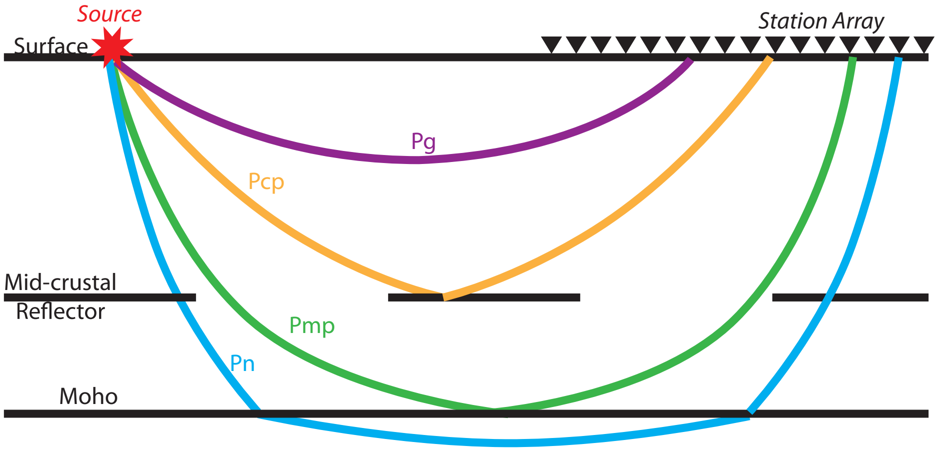

Figure 14. The key crustal phases for the HLP controlled-source experiment: the crustal diving wave Pg, the mid-crustal reflector PcP, the Moho reflector PmP ,and Pn Moho refracted wave.

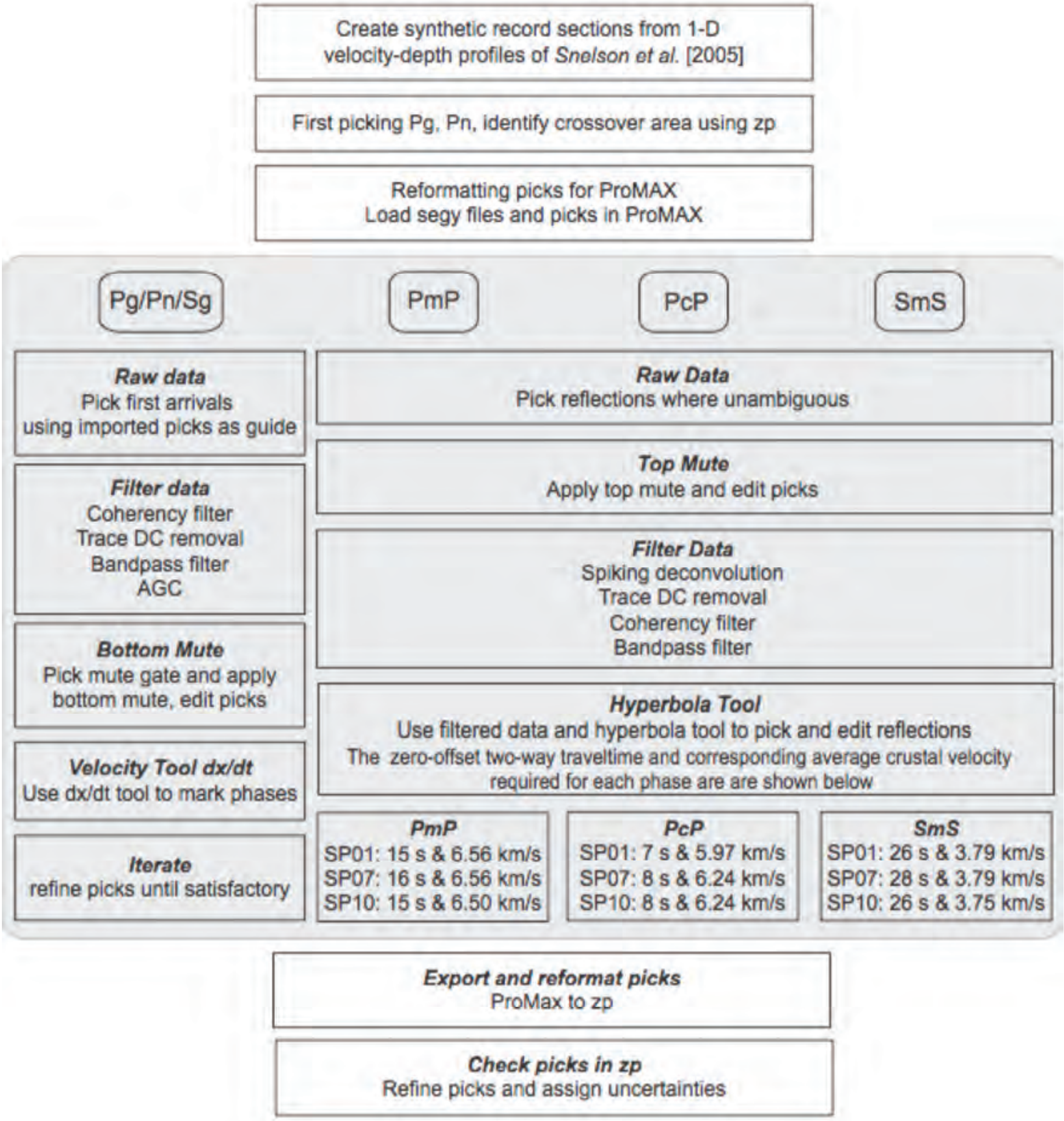

Figure 15. Intial workflow that was used to process the HLP data [from *Rumpfhuber et al.,* 2009].

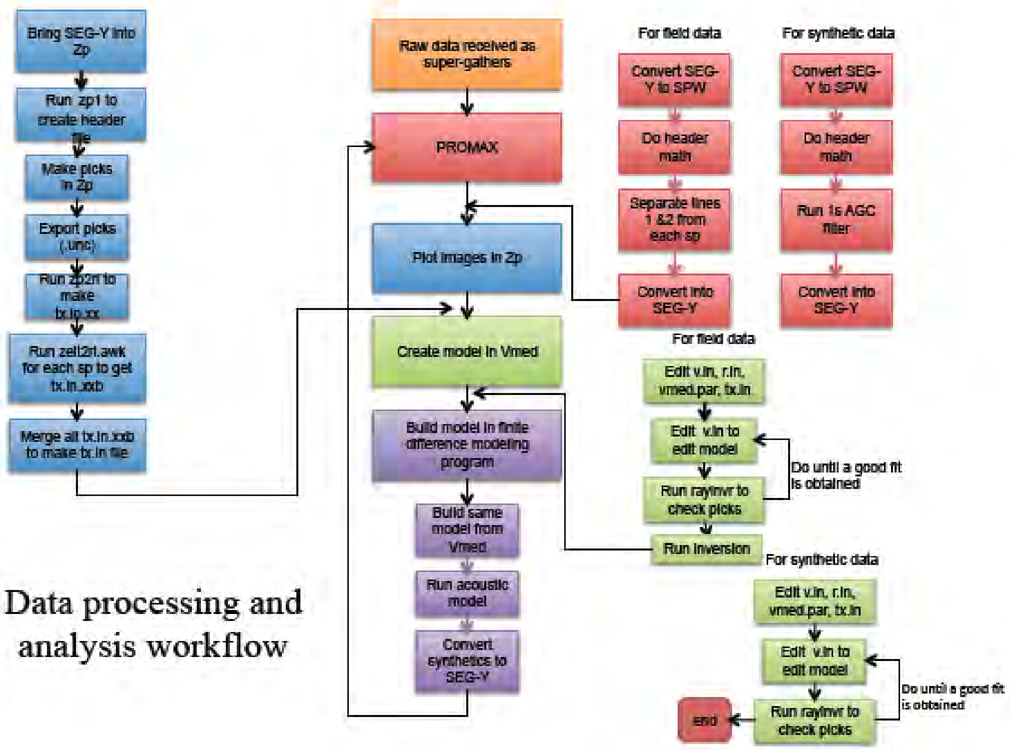

Figure 16. Final workflow used to analyze the High Lava Plains data.

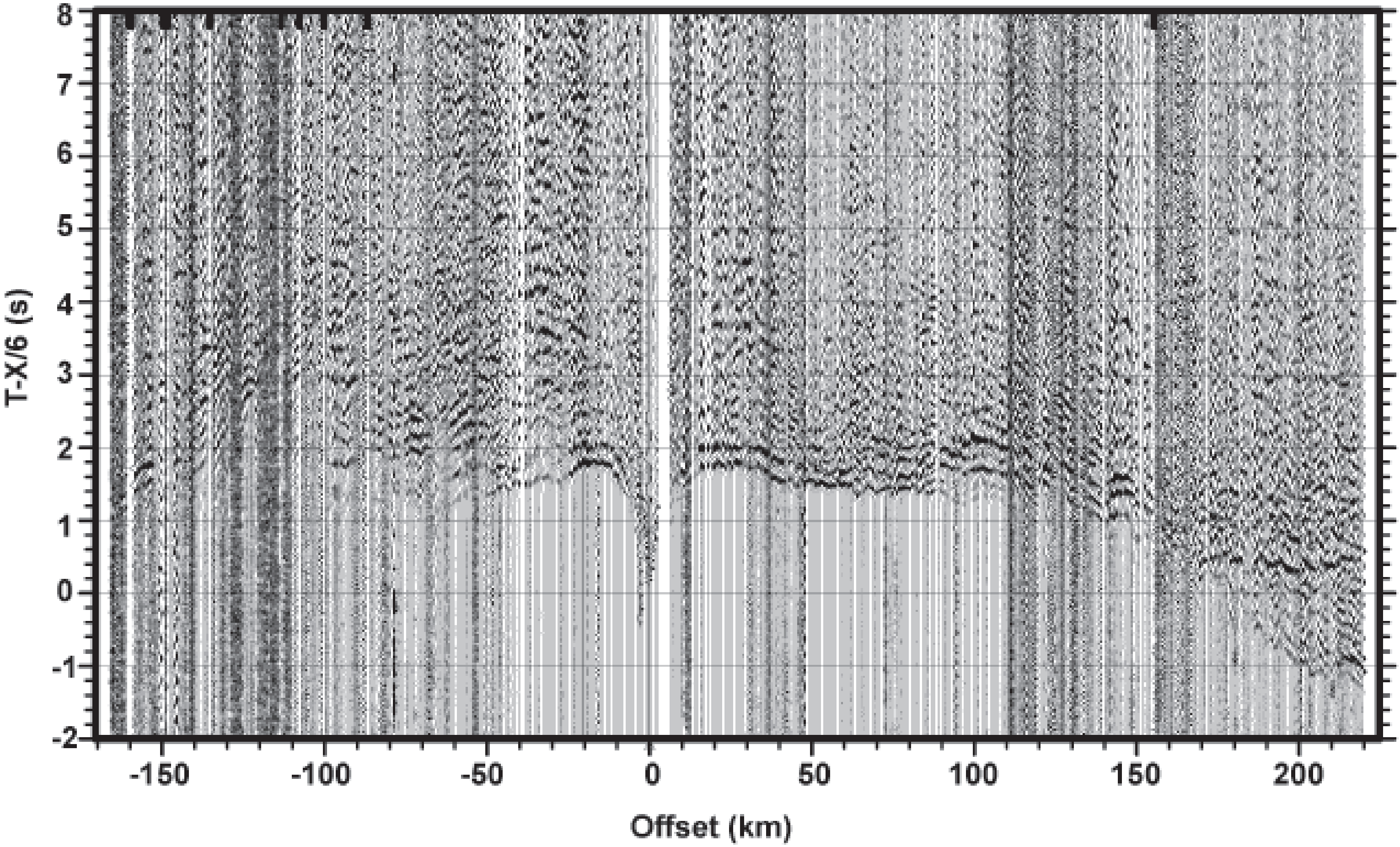

Figure 17. Raw, unfiltered shotgather SP 14.

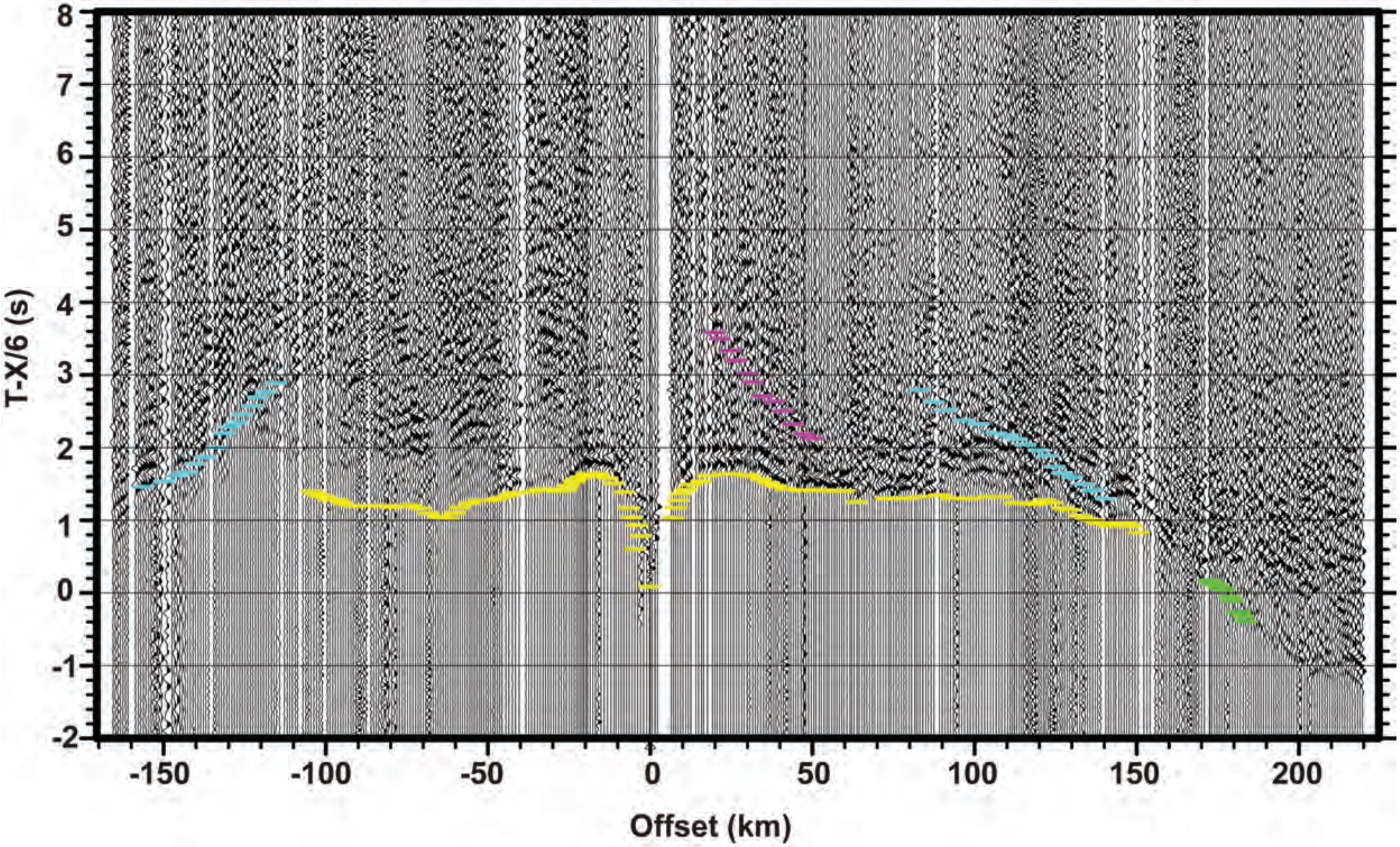

Figure 18. Shotgather SP 14 after applying a 2-4-12-15 Ormsby filter and muting of bad traces. Travel time picks corresponding to Pg (yellow), PcP (pink), PmP (light blue), and Pn (green) events.

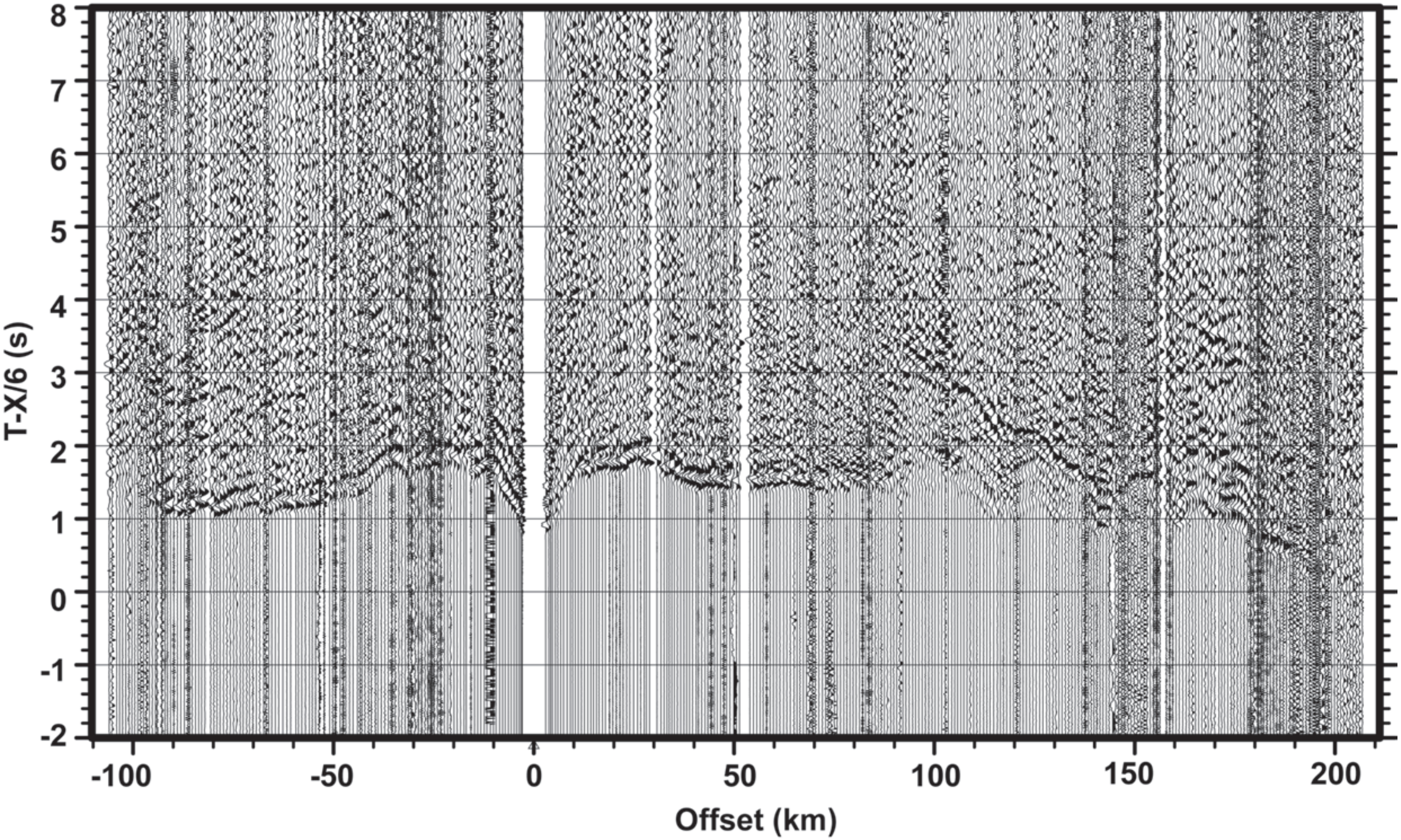

Figure 19. Raw, Unfiltered shotgather SP 25.

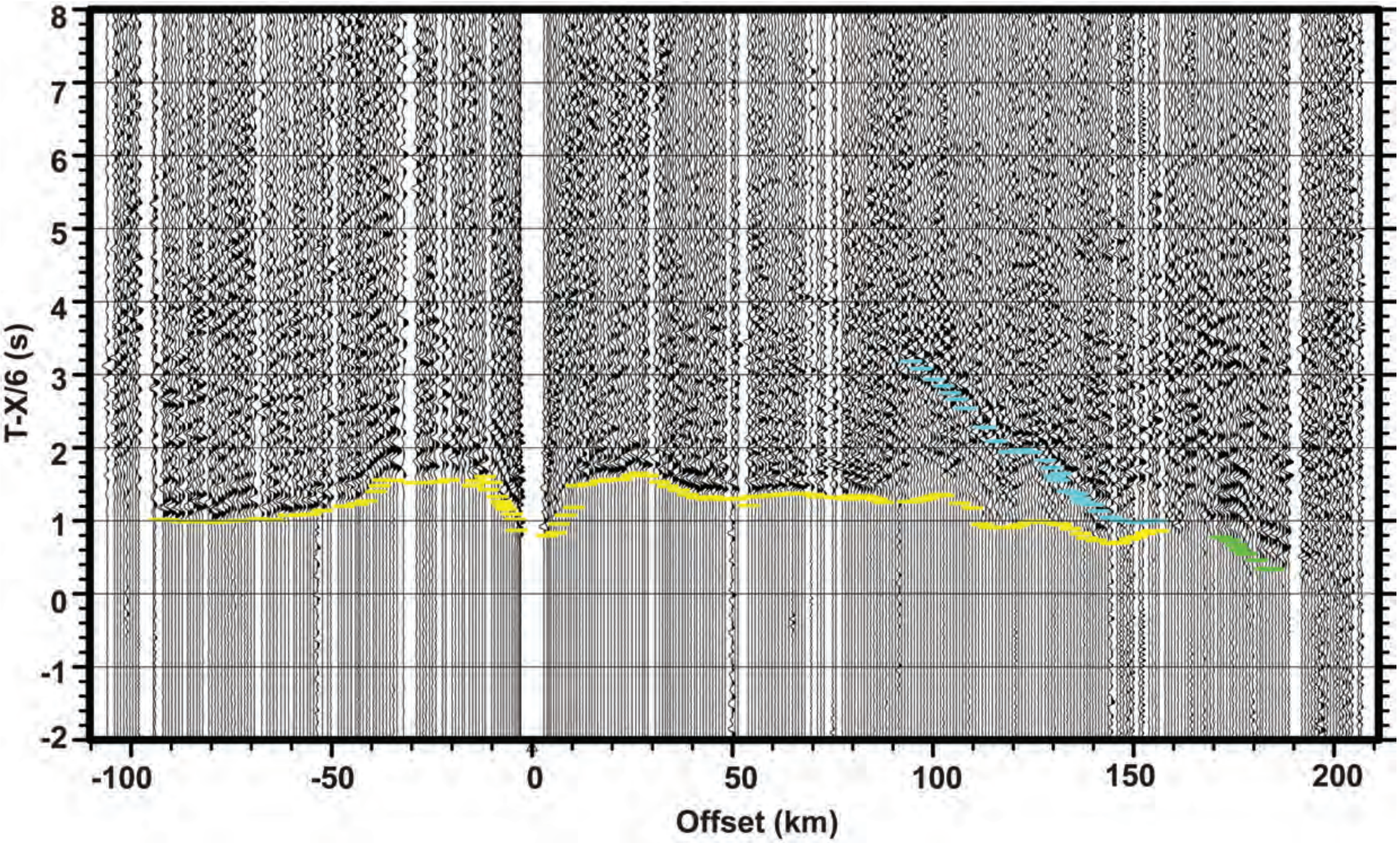

Figure 20. Shotgather SP 25 after applying a 2-4-12-15 Ormsby filter and muting of bad traces. Travel time picks corresponding to Pg (yellow), PmP (light blue), and Pn (green) events.

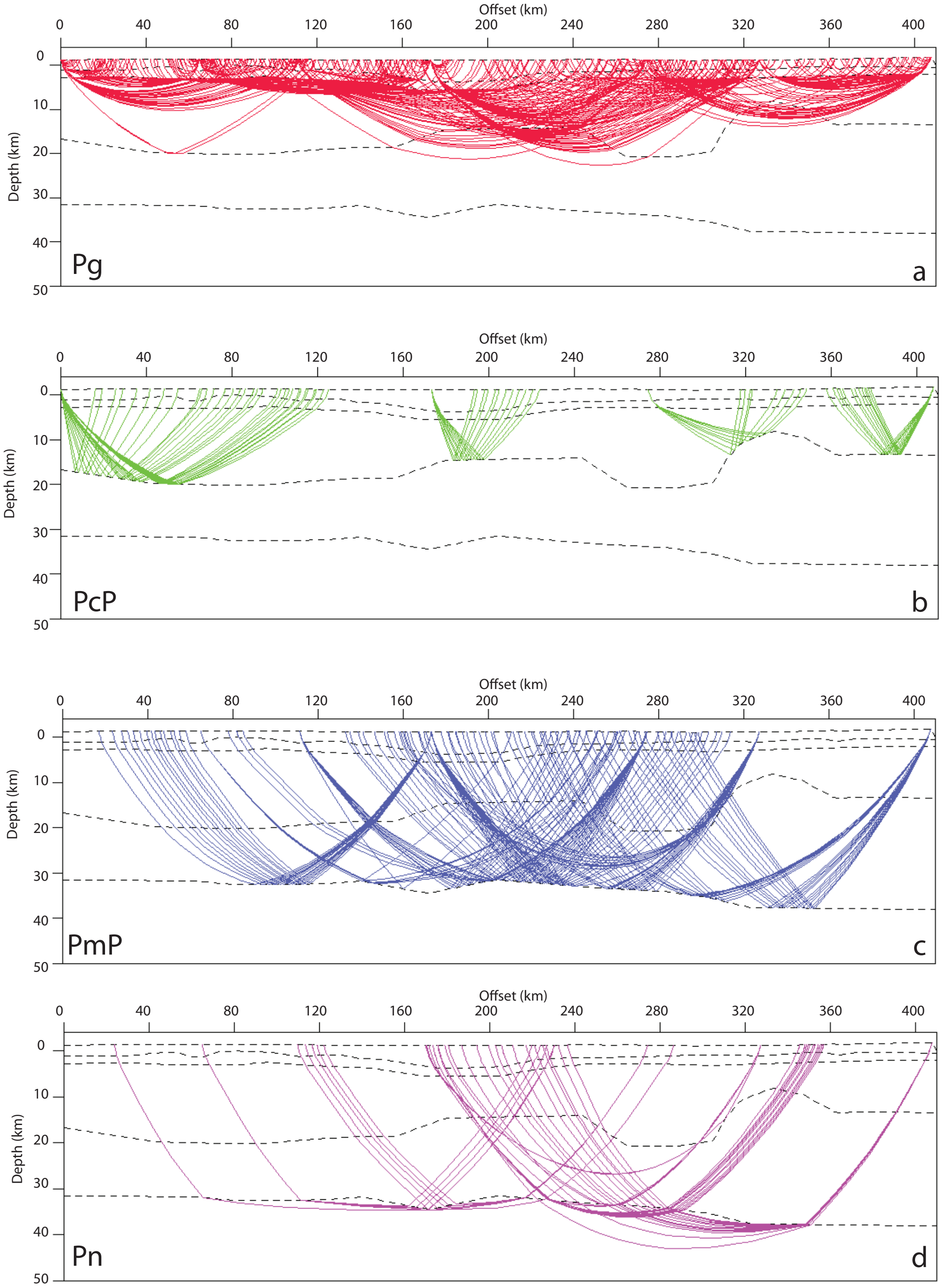

Figure 21. Ray coverage figures for Line 1 the crustal diving wave Pg (a), the mid-crustal reflector PcP (b), the Moho reflection PmP (c), and the mantle refraction, Pn (d).

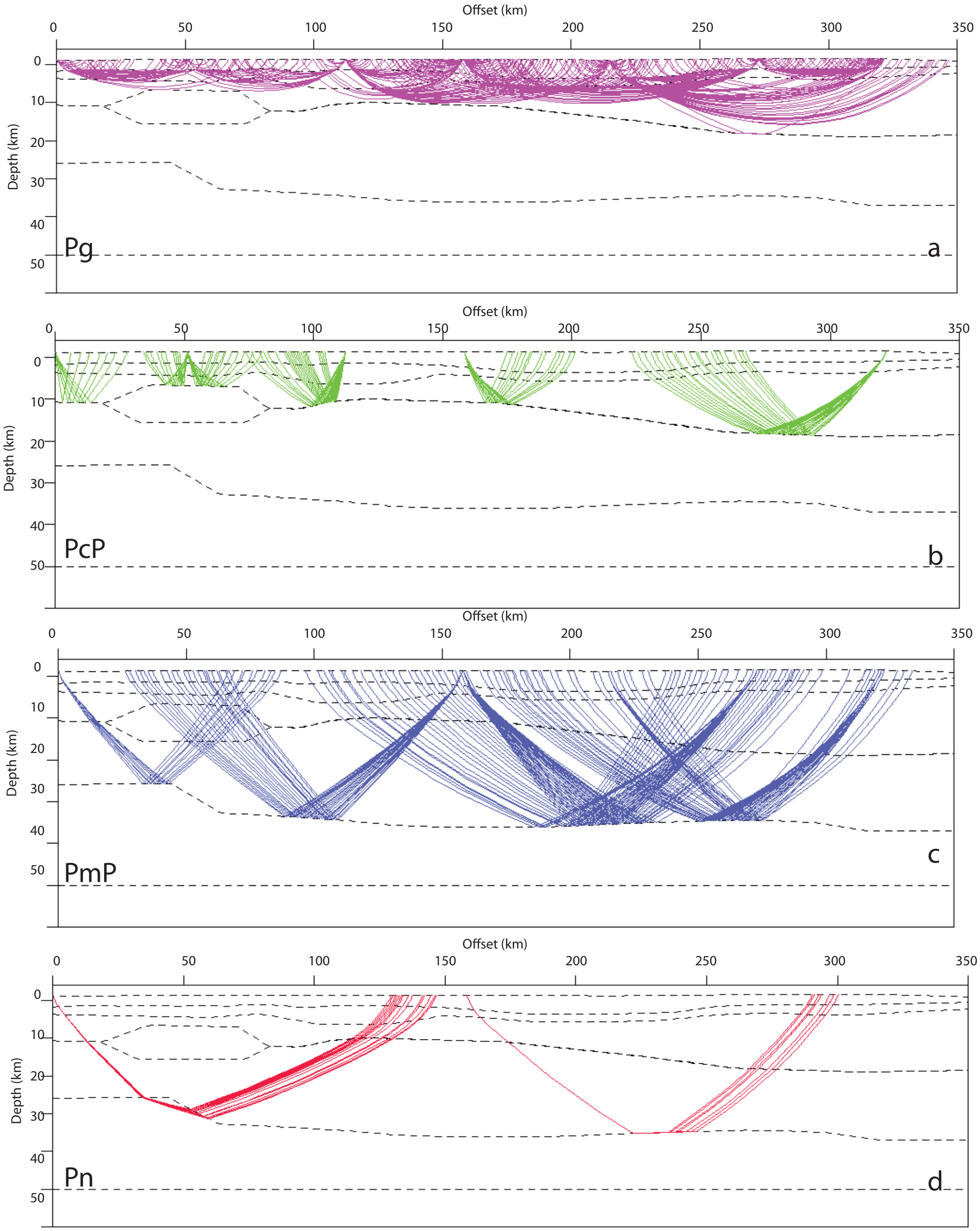

Figure 22. Ray coverage figures for Line 2 the crustal diving wave Pg (a), the mid-crustal reflector PcP (b), the Moho reflection PmP (c), and mantle refraction, Pn (d).

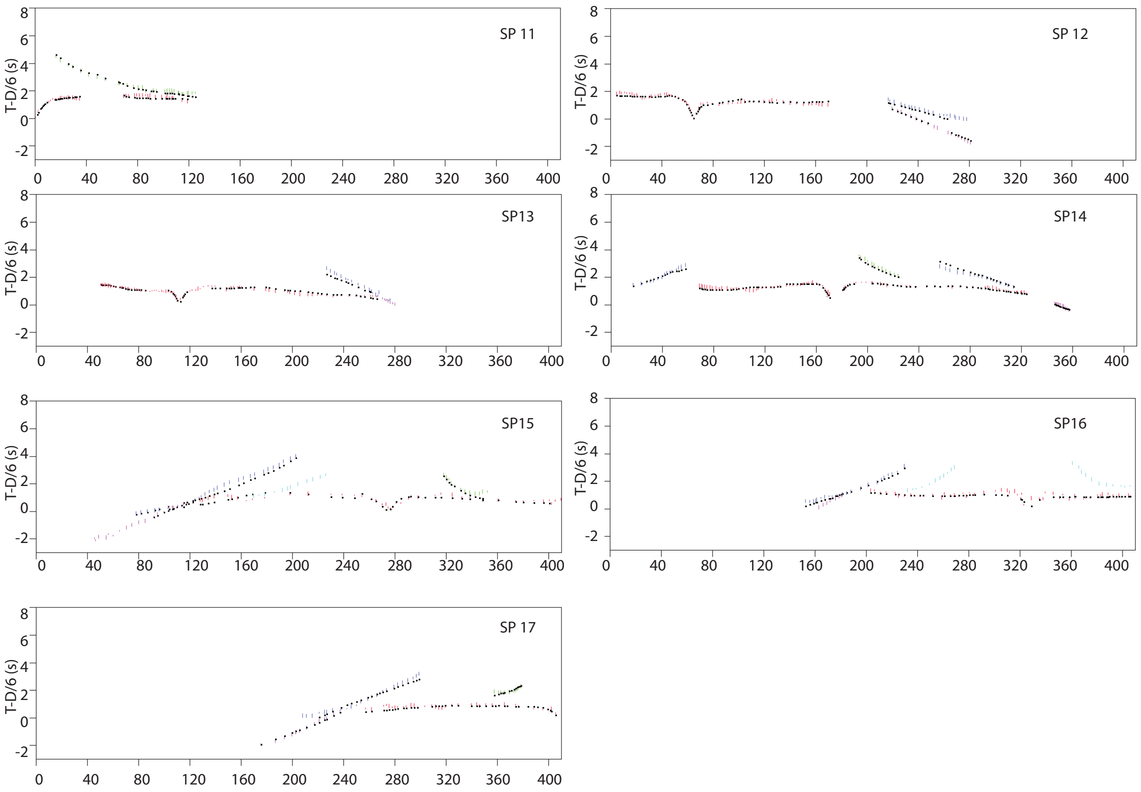

Figure 23. The key crustal phases for Line 1 showing typical large-scale refraction and wide-angle reflection controlled source experiment: the crustal diving wave Pg (pink), the Moho reflector (blue) PmP, PcP from a mid-crustal reflector (green), and the Moho refracted wave Pn (pink).

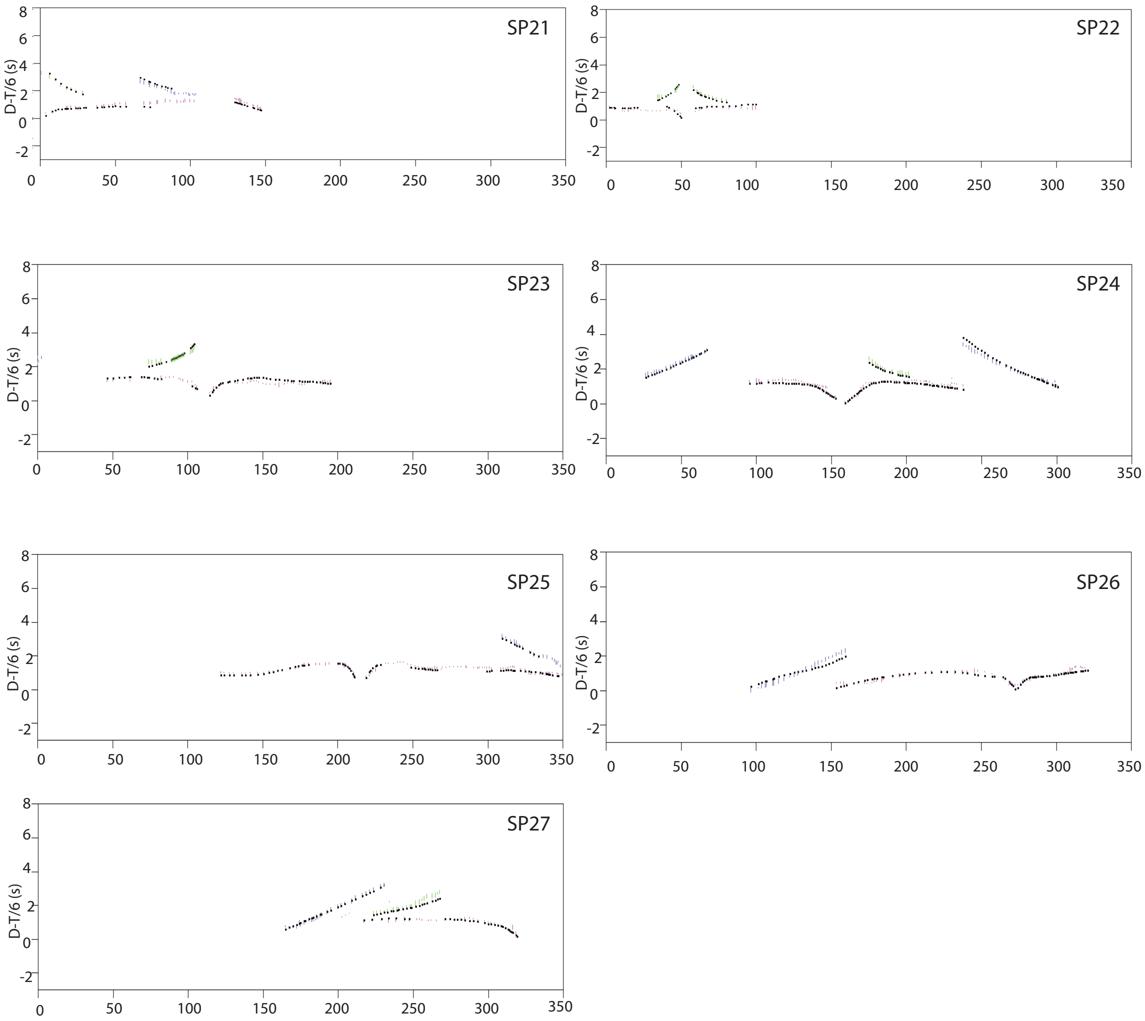

Figure 24. The key crustal phases for Line 2 showing typical large-scale refraction and wide-angle reflection controlled source experiment: the crustal diving wave Pg (red), the Moho reflector (blue) PmP, PcP from a mid-crustal reflector (green), and the Moho refracted wave Pn (pink).

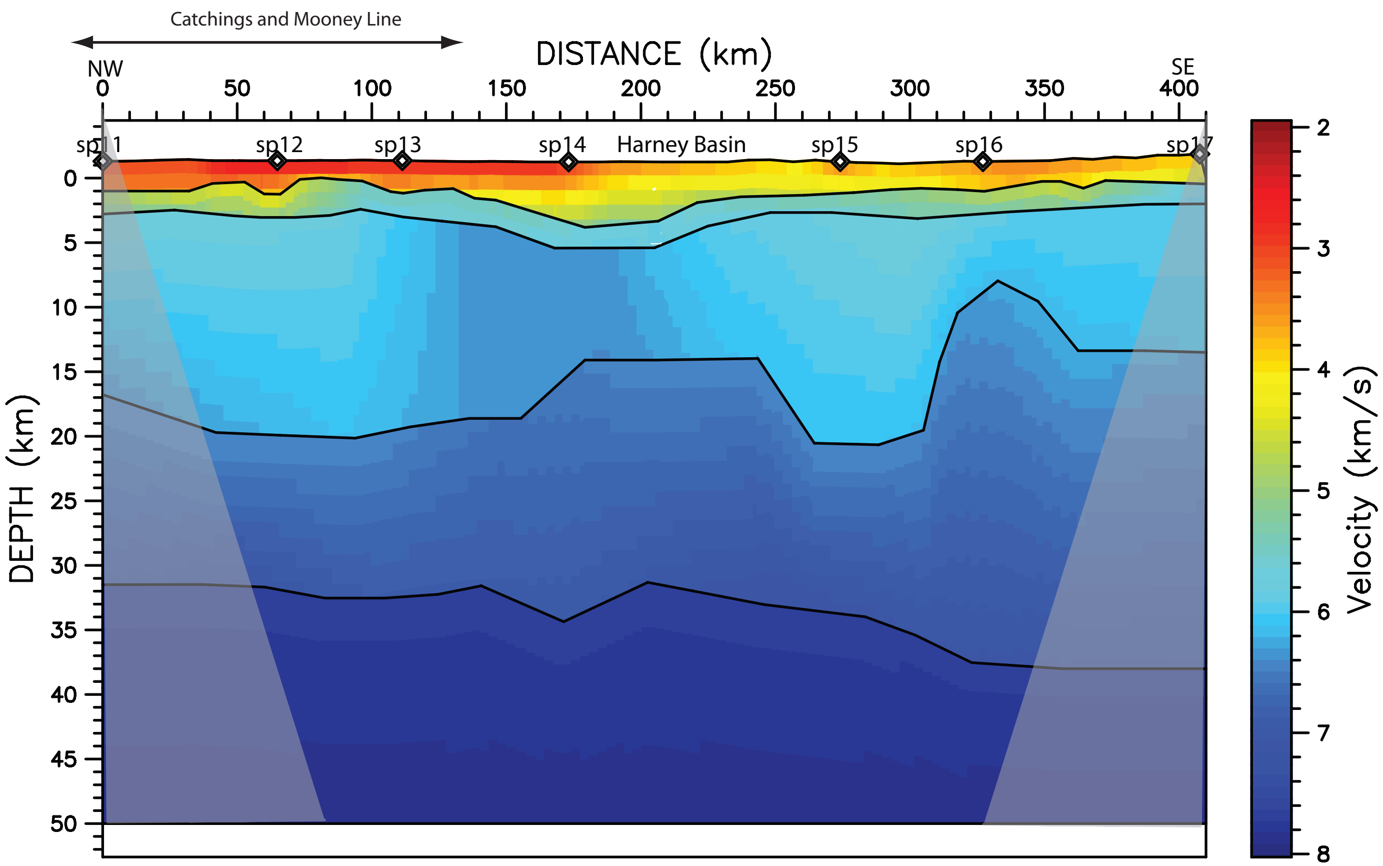

Figure 25. P-wave velocity model before the inversion for Line 1 generated from the picked field data events. The grey shaded areas indicate areas lacking ray coverage.

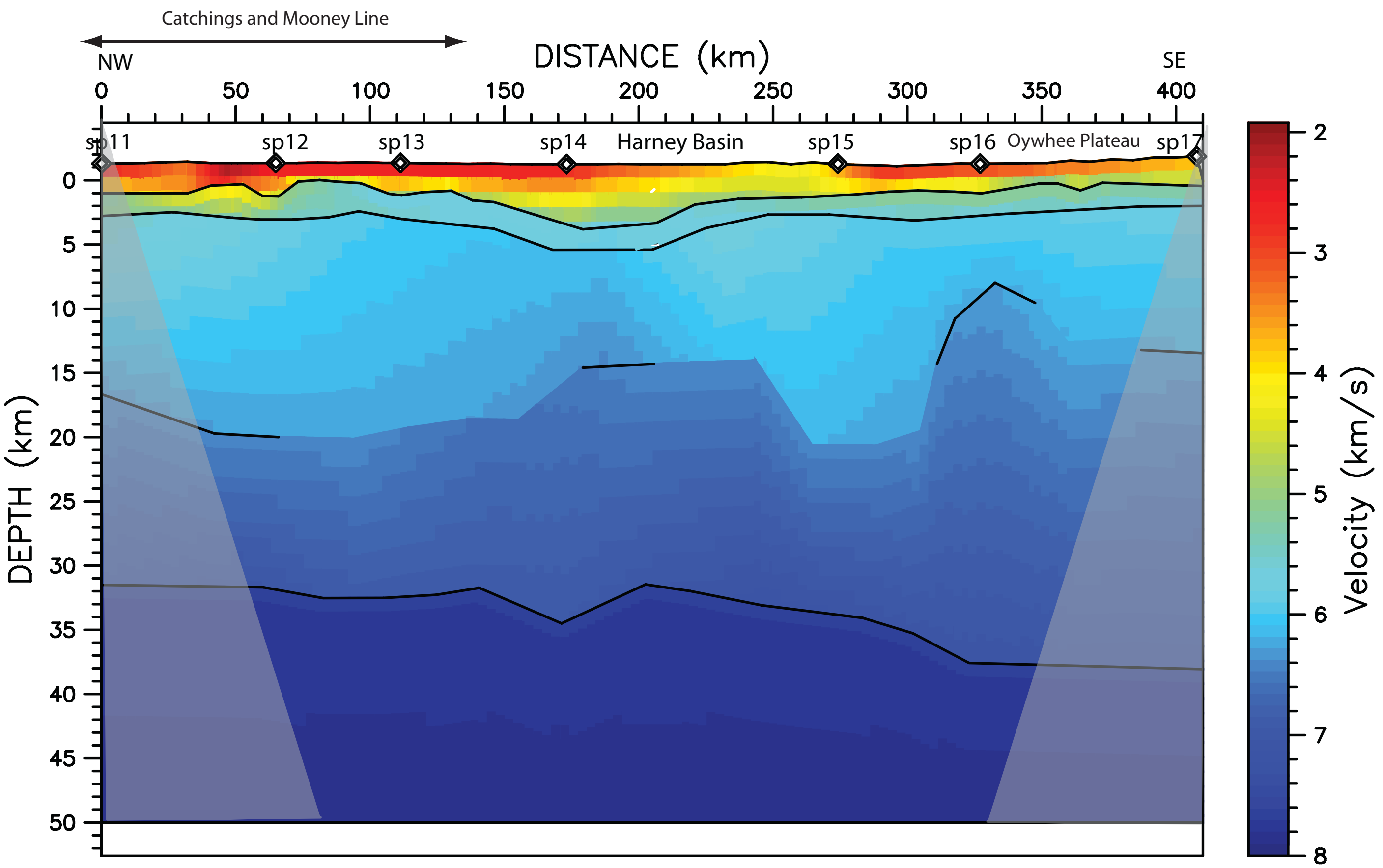

Figure 26. Final P-wave velocity model for Line 1 generated from the picked field data events. The grey shaded areas indicate areas lacking ray coverage.

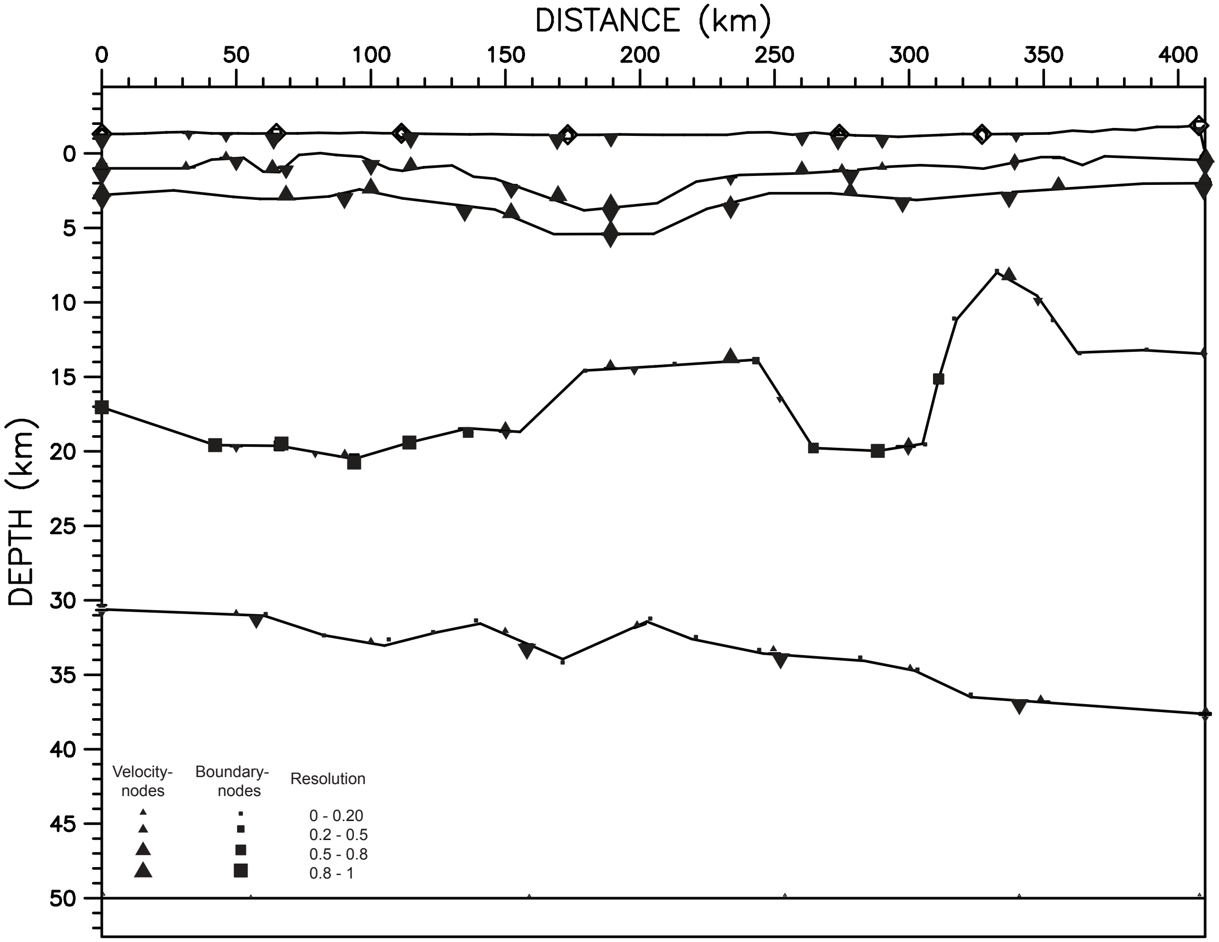

Figure 27. Resolution estimates for the final Line 1 P-wave velocity model derived from RAYINVR. The squares represent boundary nodes, the triangles represent velocity nodes, and the sizes of the symbols are scaled to represent the corresponding values of the resolution matrix.

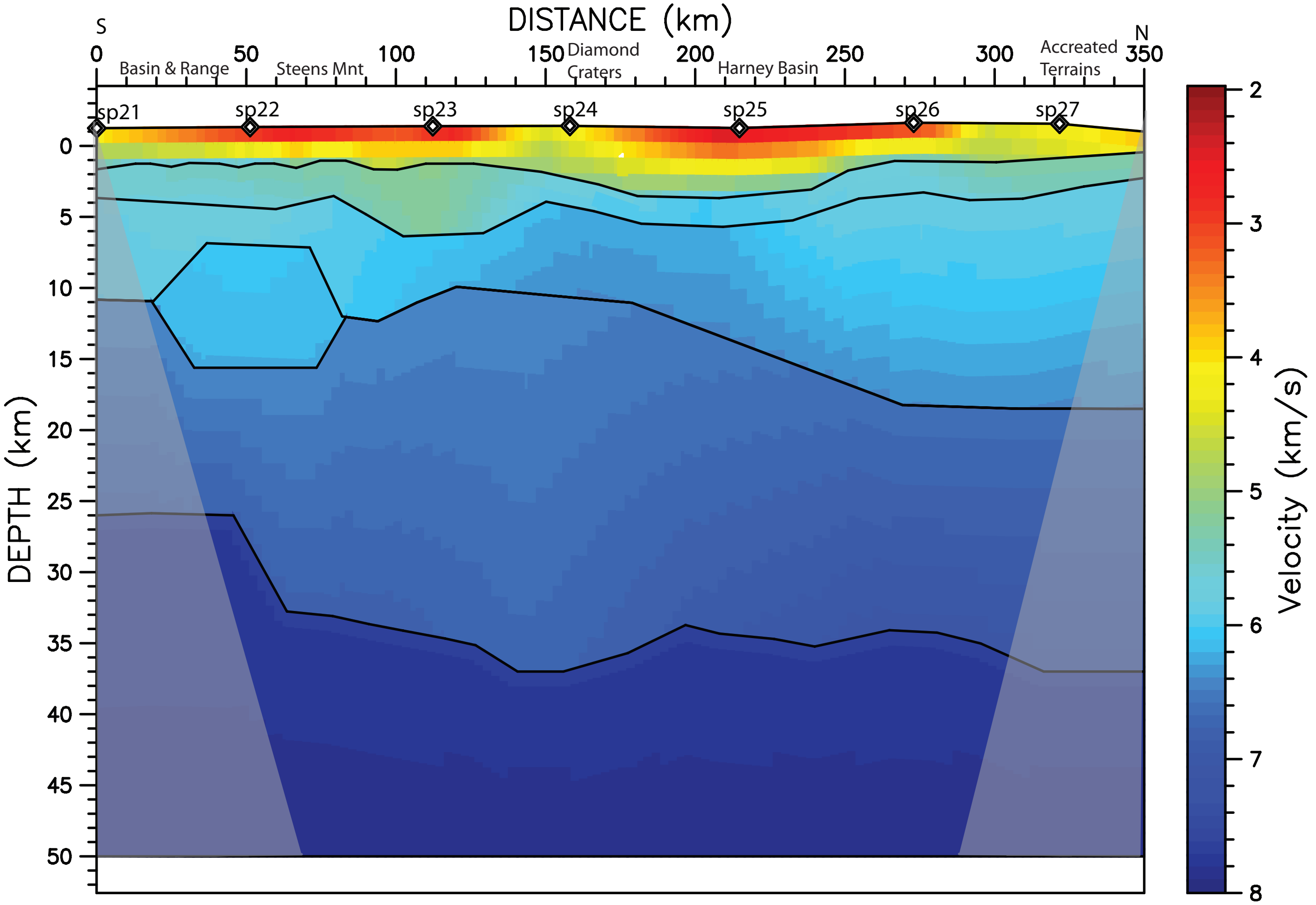

Figure 28. P-wave velocity model before the inversion for Line 2 generated from the picked field data events. The grey shaded areas indicate areas lacking ray coverage.

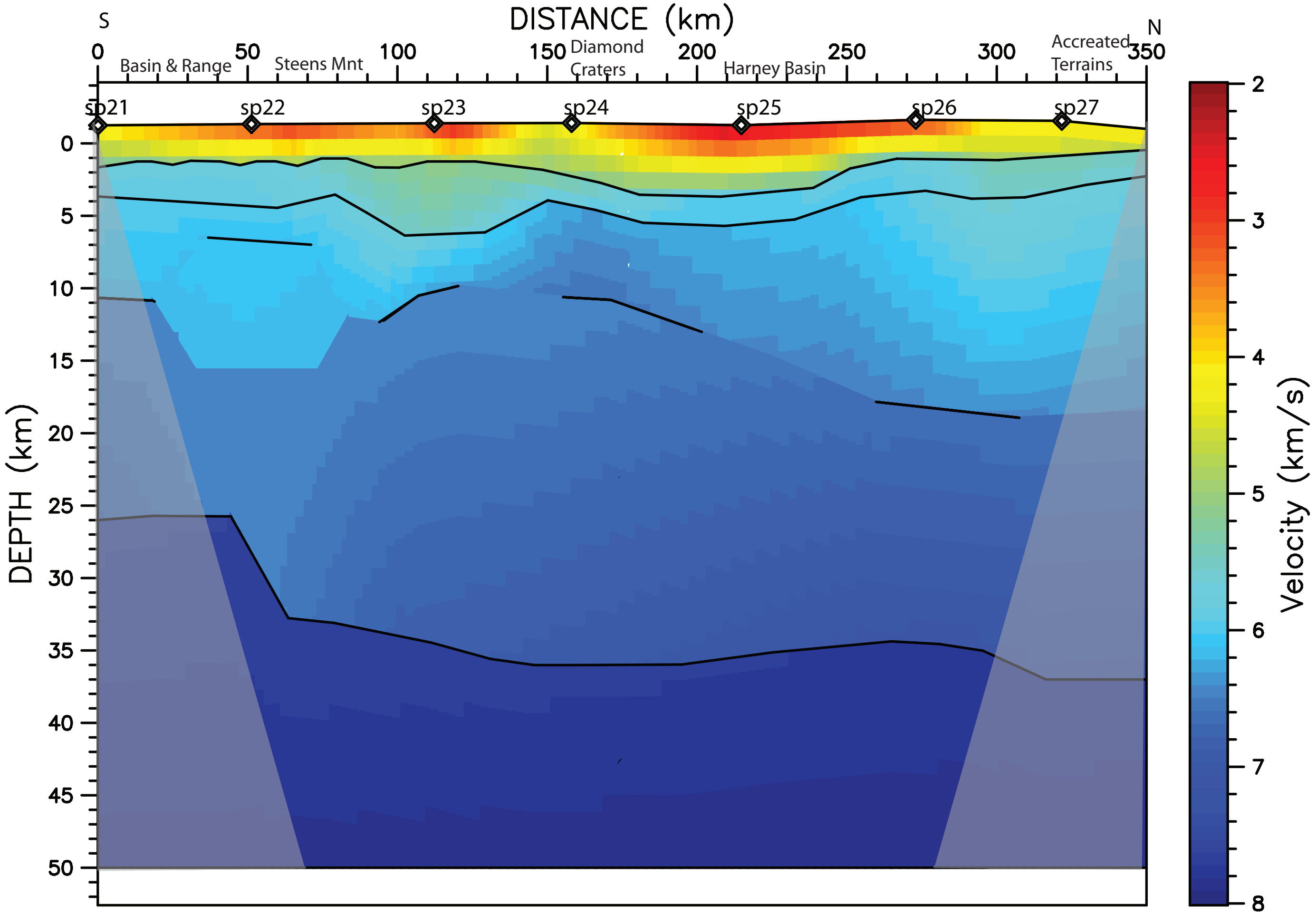

Figure 29. P-wave velocity model after the inversion for Line 2 generated from the picked field data events. The grey shaded areas indicate areas lacking ray coverage.

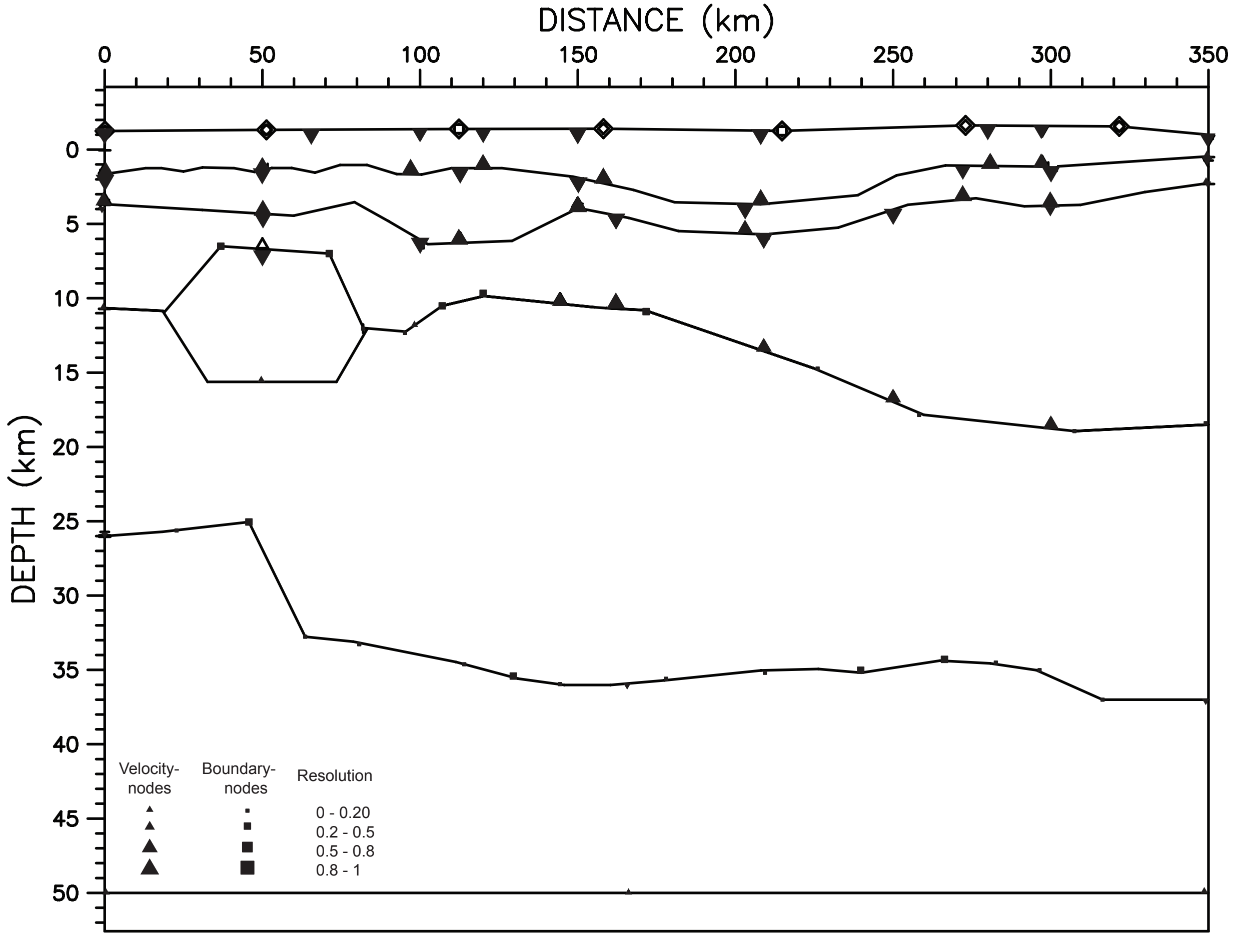

Figure 30. Resolution estimates for the final Line 2 P-wave velocity model derived from RAYINVR. The squares represent boundary nodes, the triangles represent velocity nodes, and the sizes of the symbols are scaled to represent the corresponding values of the resolution matrix.

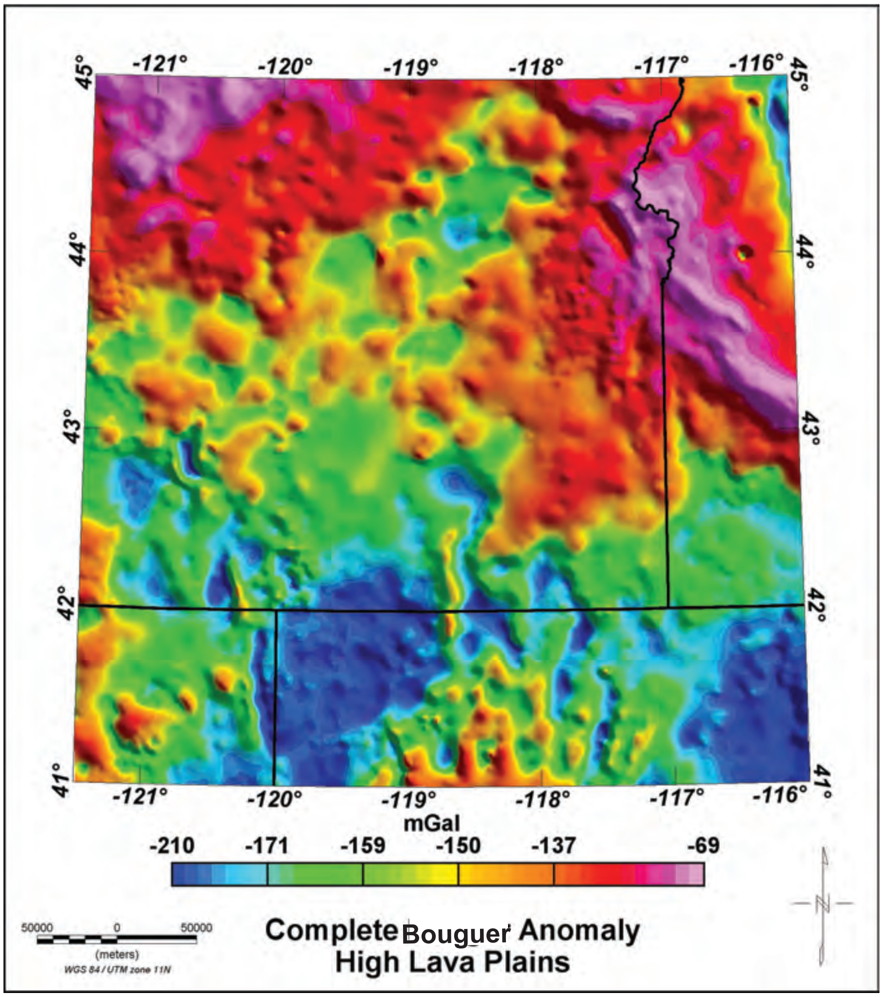

Figure 31. Complete Bouguer Anomaly map for the High Lava Plains.

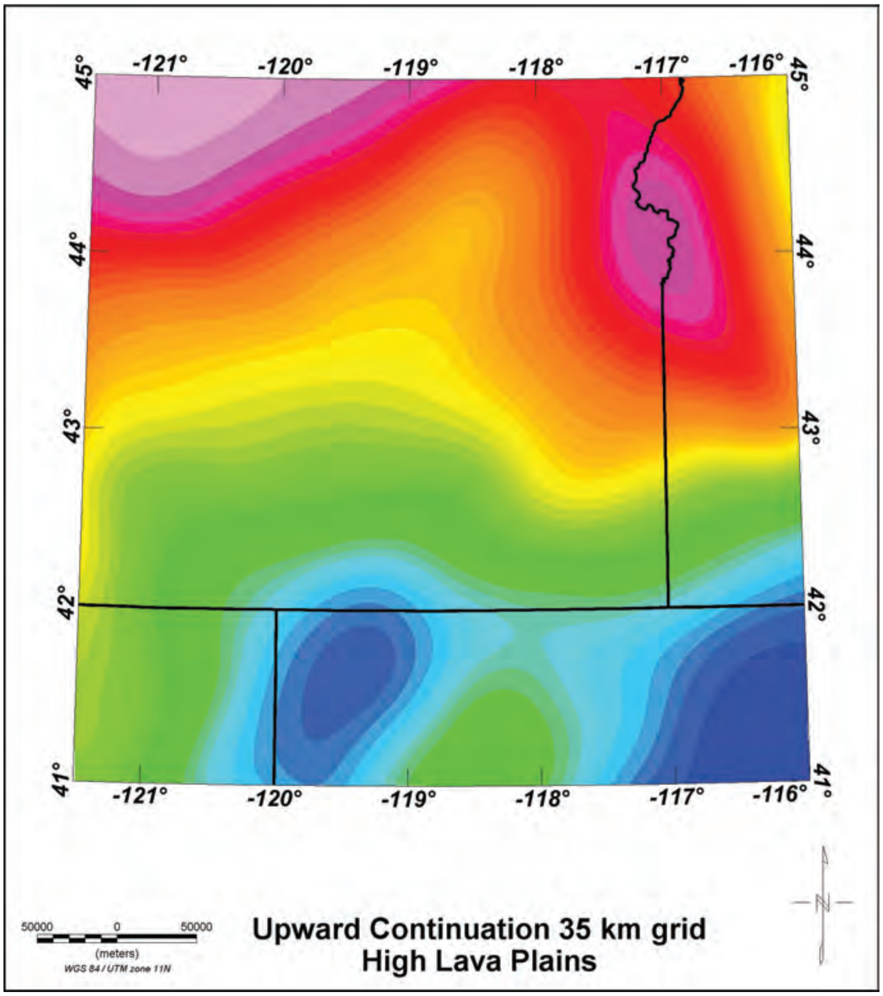

Figure 32. The Bouguer anomaly grid was upward contiuned 35 km. Them this gird was subtracted from the Bourguer anomaly to produce a residual gravity map.

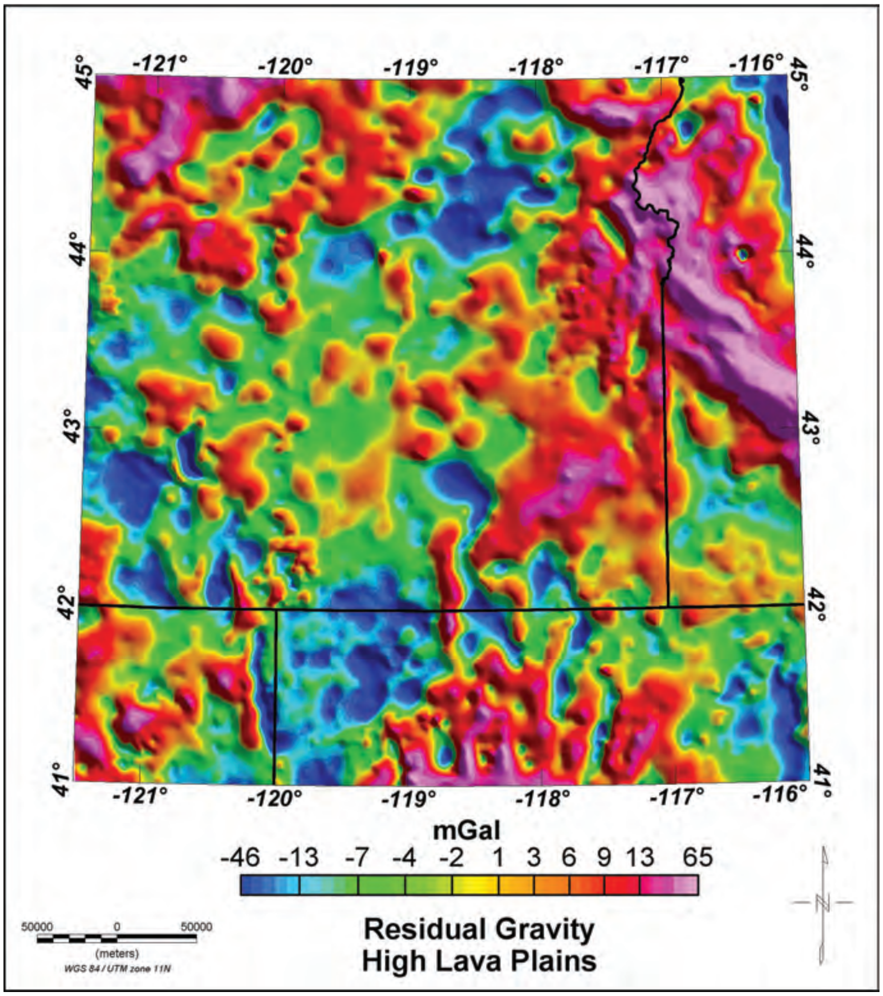

Figure 33. Residual gravity map for the High Lava Plains

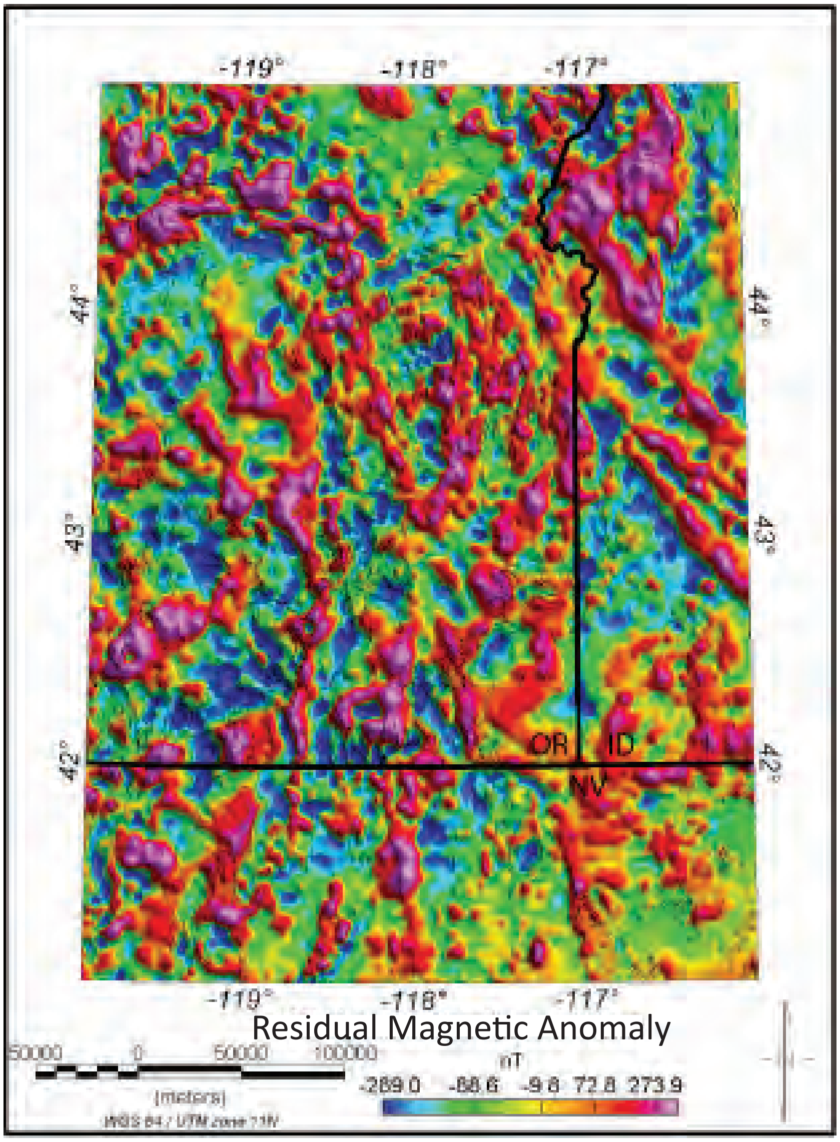

Figure 34. Magnetic residual map for the High Lava Plains

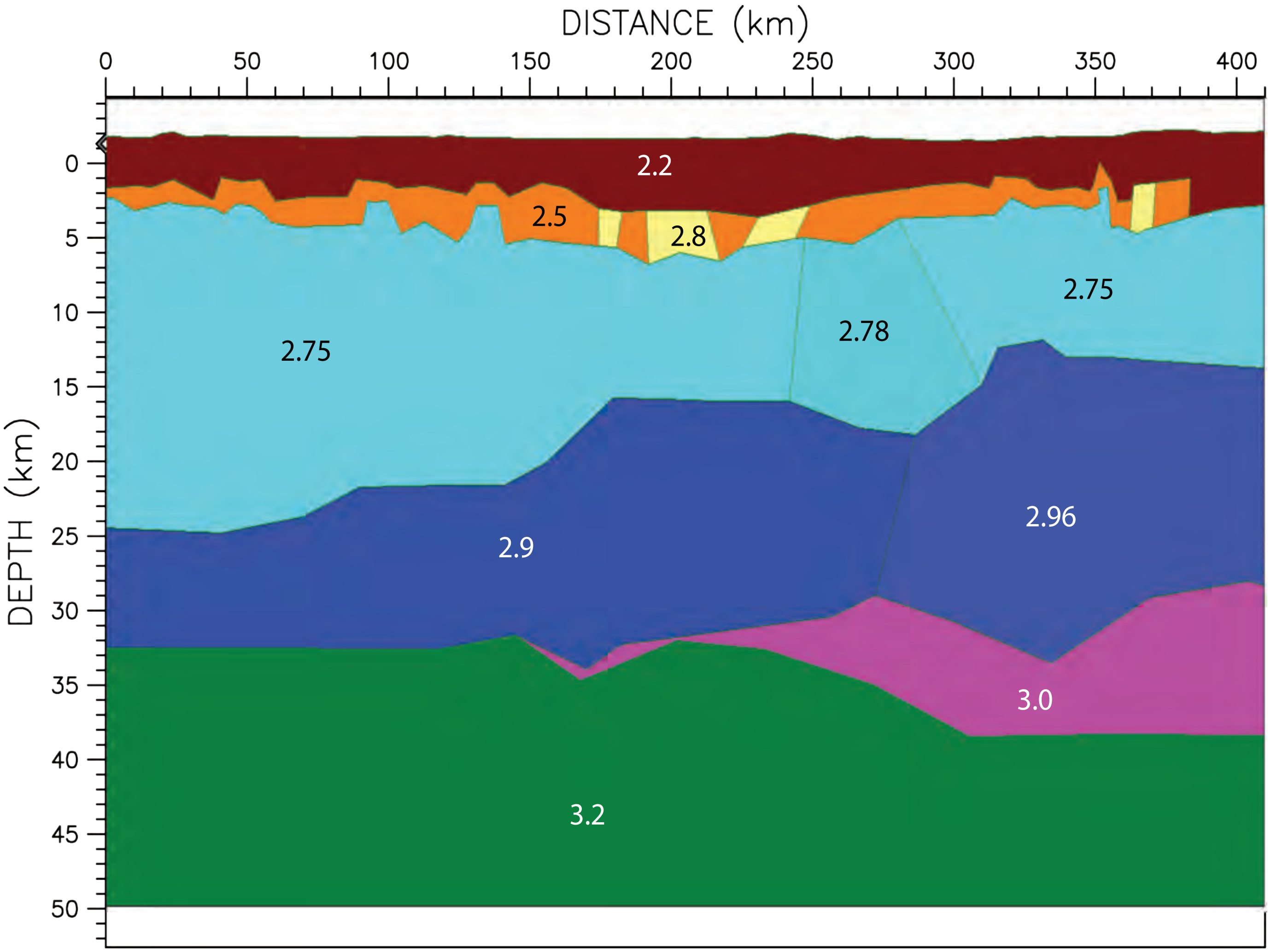

Figure 35. Density (g/cm^3) model for Line 1 that is constrained by the seismic data.

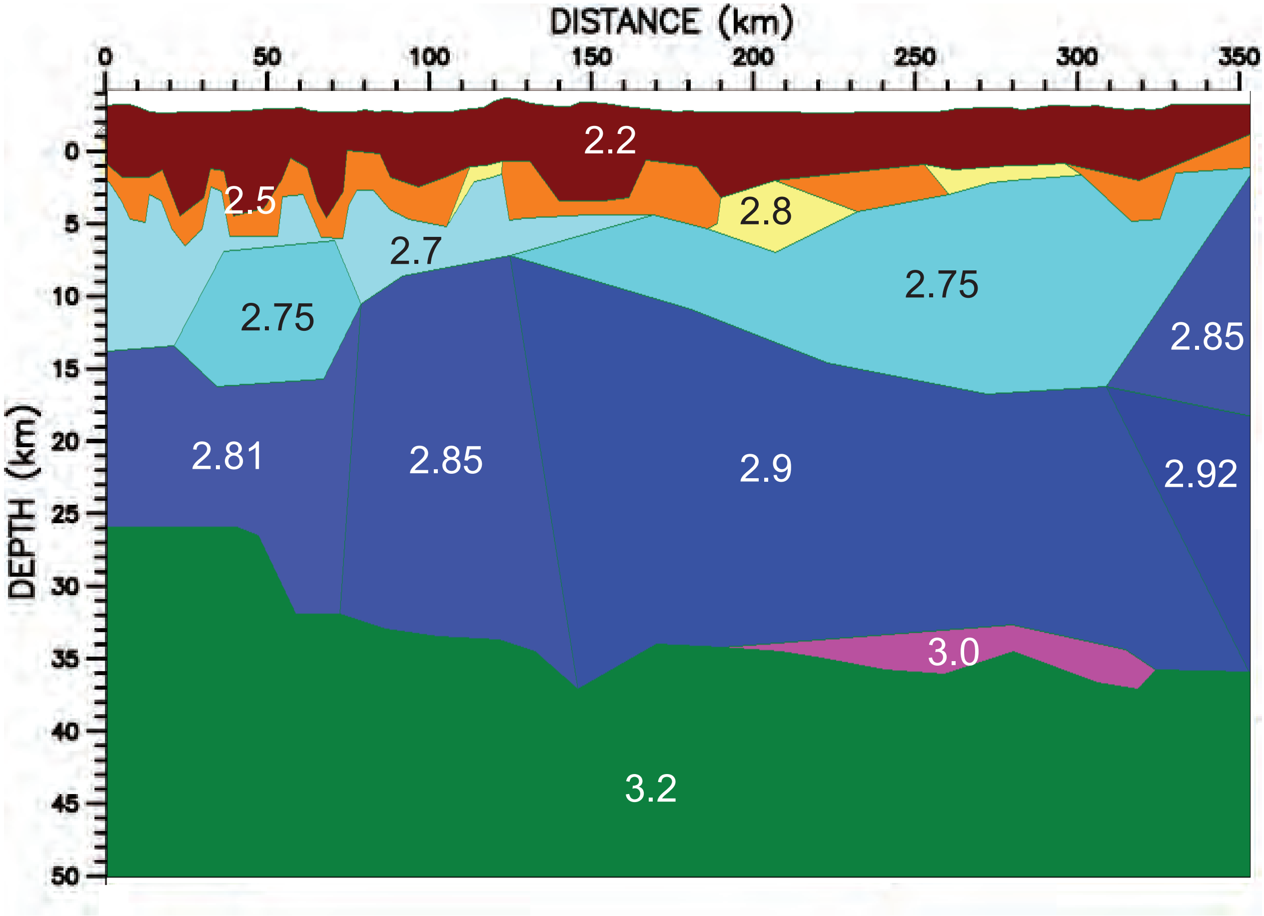

Figure 36. Density model for Line 2 that is constrained by the seismic data. Density values are in g/cm^3.

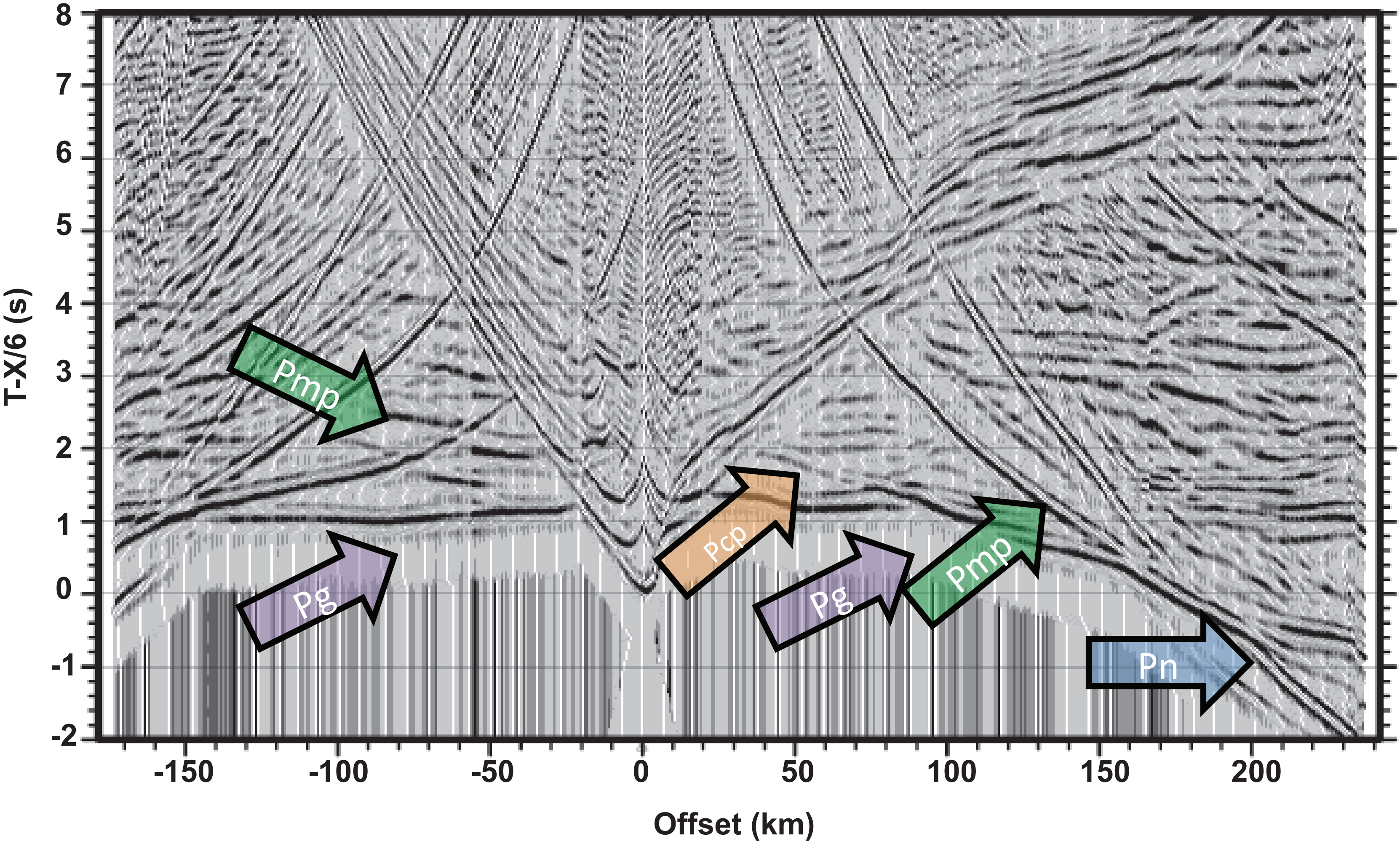

Figure 37. Synthetic seismogram for SP 14 that was created using a commercial finite difference solution of the scalar wave equation. Arrows indicate crustal phases used in the inversion.

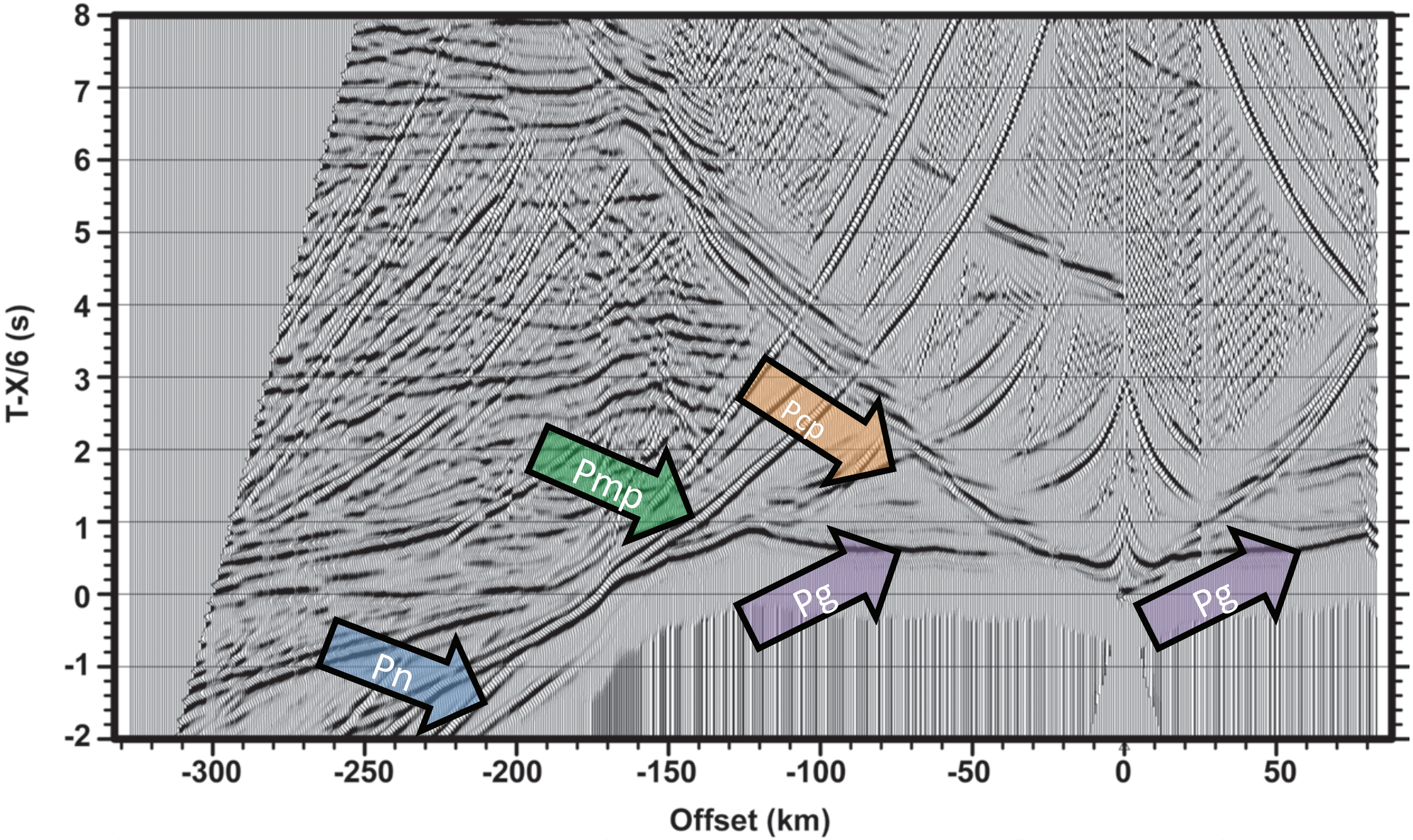

Figure 38. Synthetic seismogram for SP 16 that was created using a commercial finite difference solution of the scalar wave equation. Arrows indicate crustal phases used in the inversion.

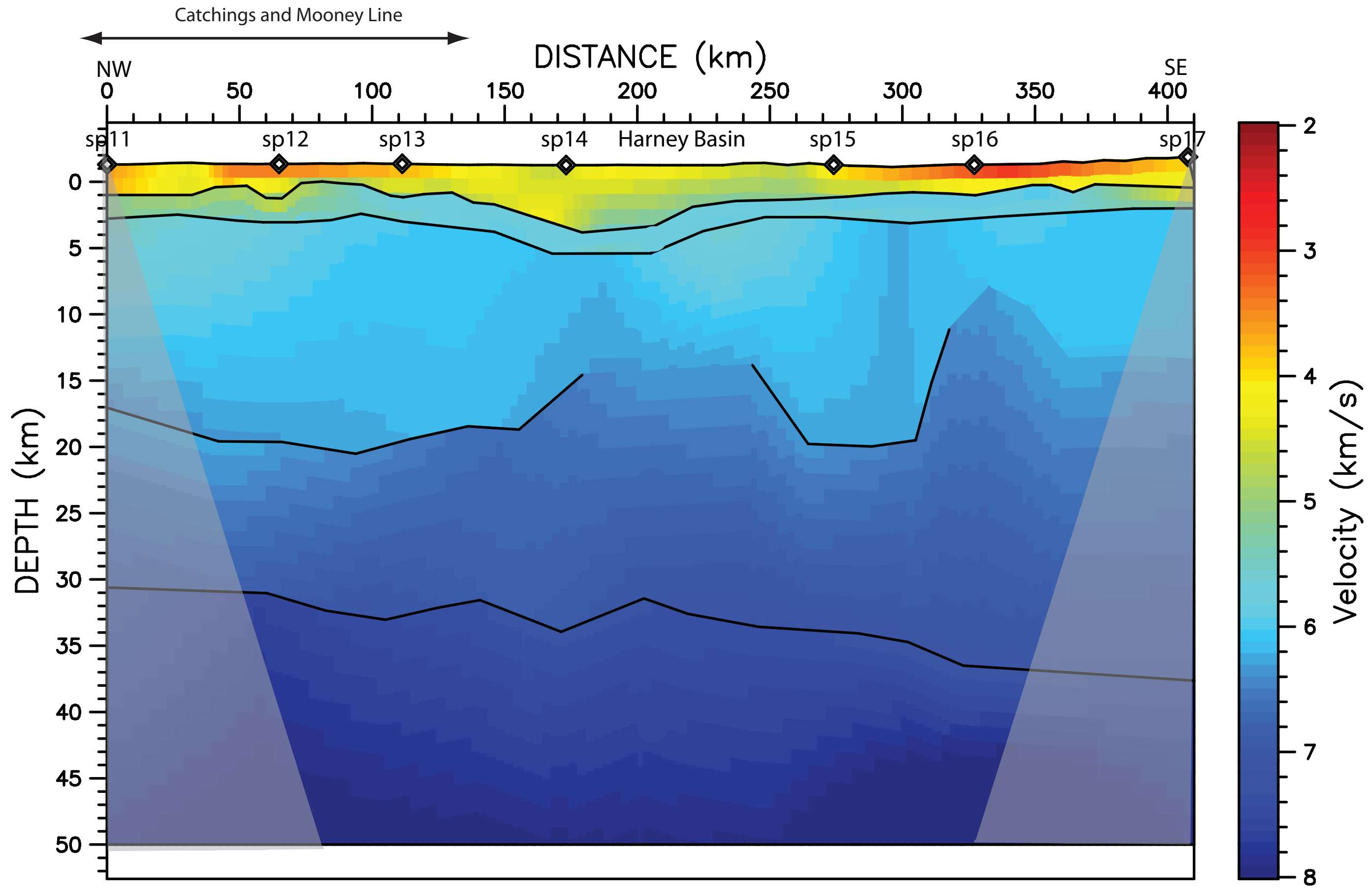

Figure 39. Final P-wave velocity model for Line 1 generated from the picked finite difference events. The similarity of this inverted image to that shown in Figure 26 validates the accuracy of the tomographic inversion algorithm. The grey shaded areas indicate areas lacking ray coverage.

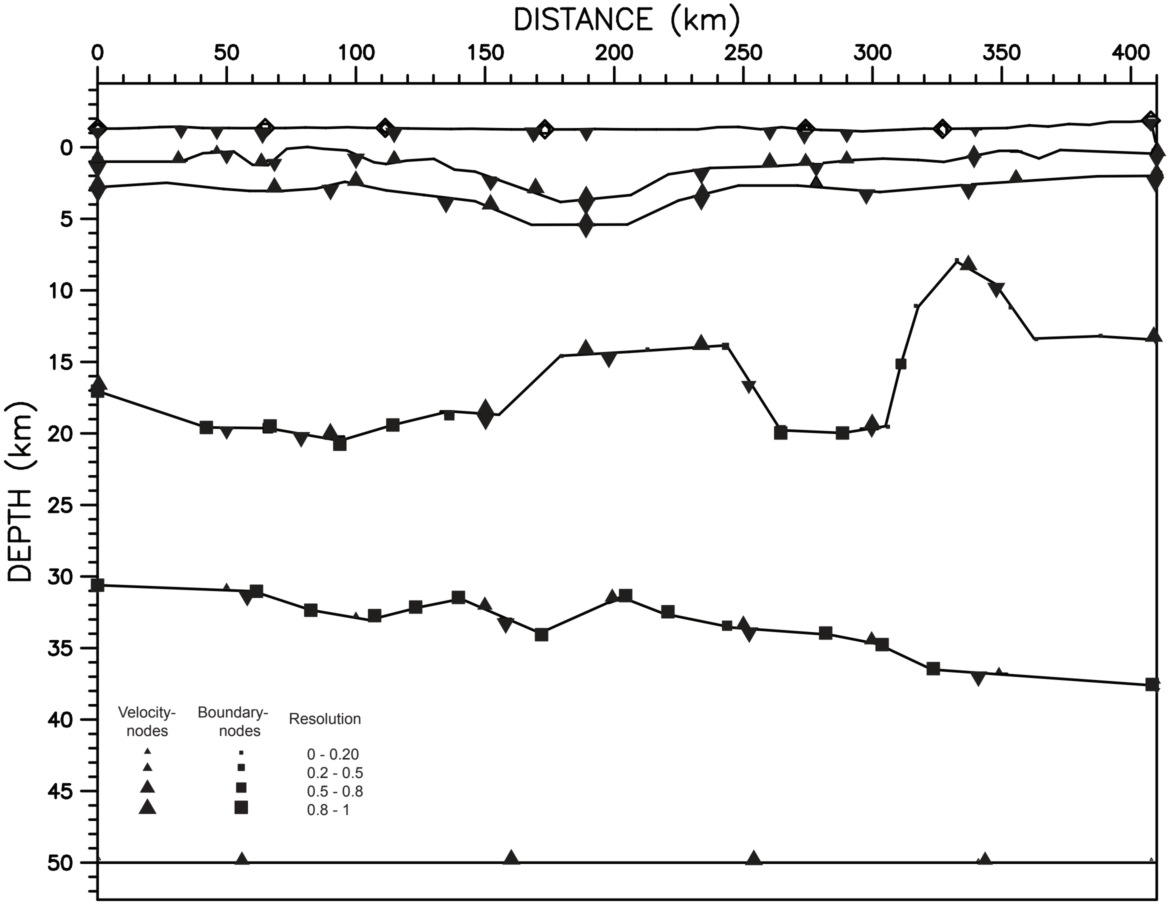

Figure 40. Resolution estimates for the final Line 1 P-wave velocity model derived from the synthetic data. The squares represent boundary nodes, the triangles represent velocity nodes, and the sizes of the symbols are scaled to represent the corresponding values of the resolution matrix.

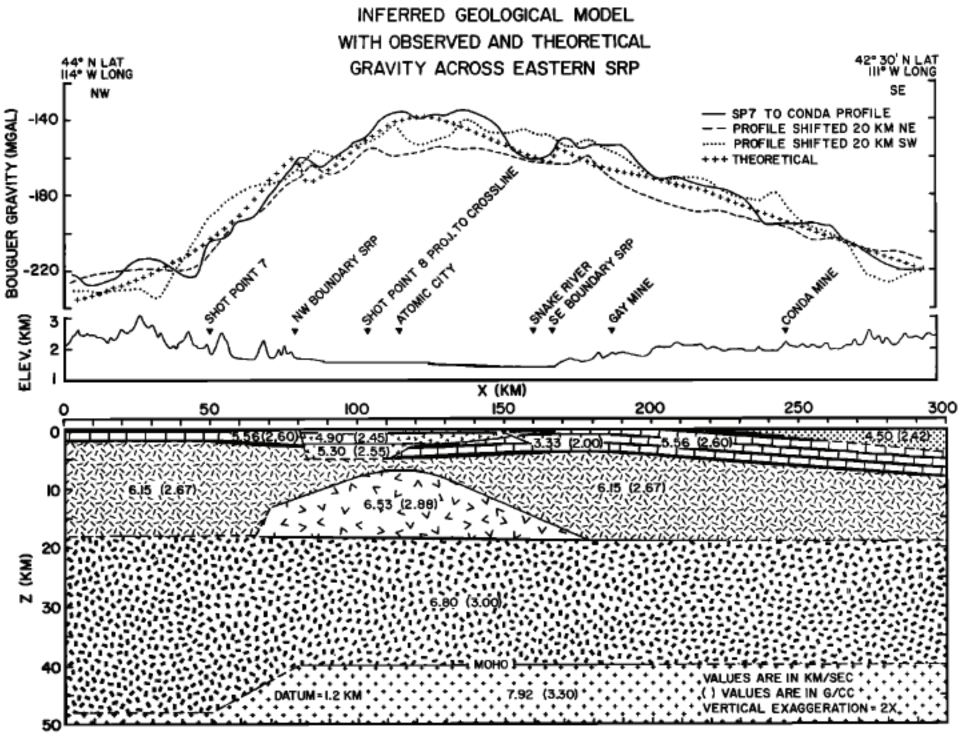

Figure 41. [from *Sparlin et al.,* 1982] Crustal model of the Snake River Plain. This model corresponds the the eastern part of Line 1.

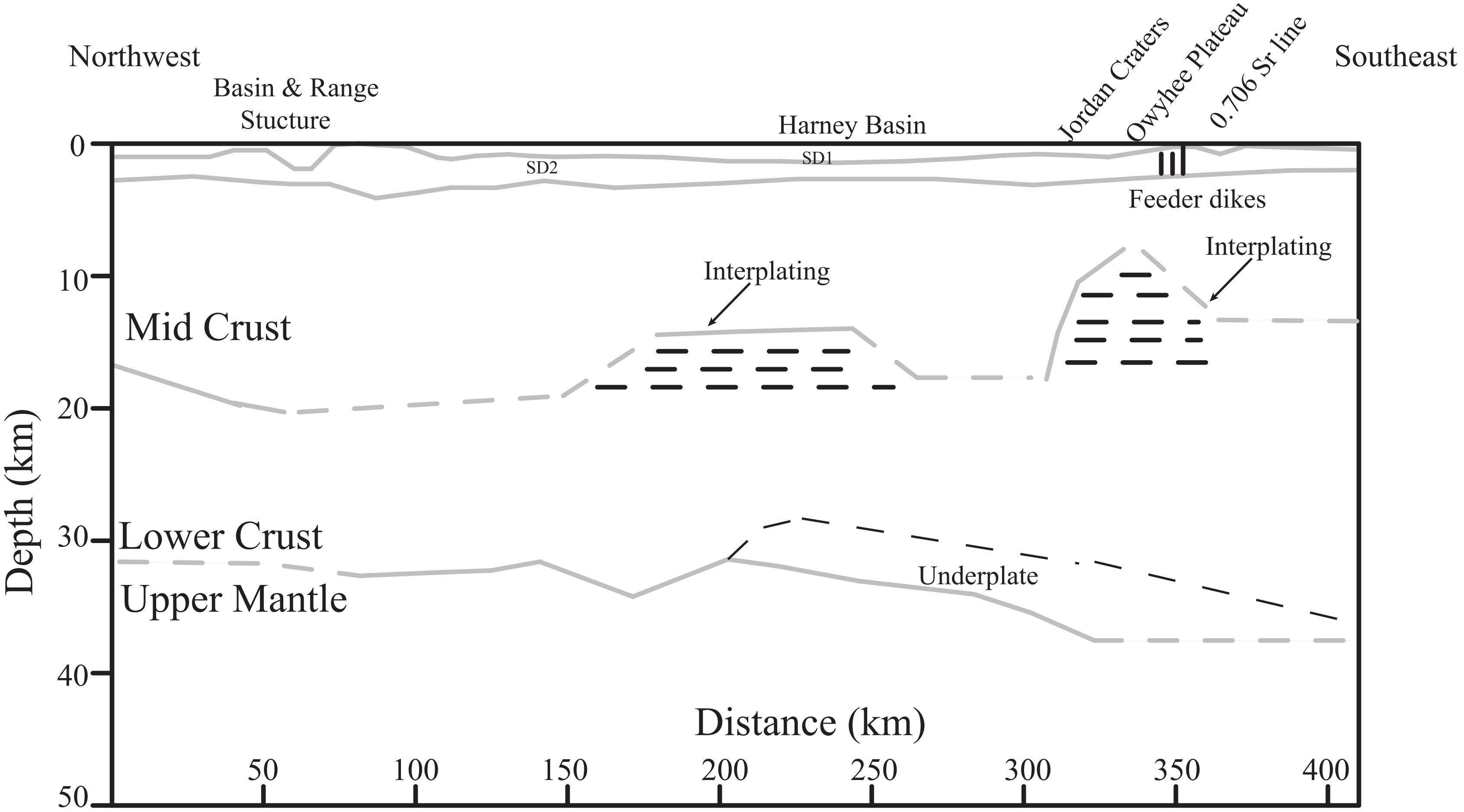

Figure 42. Geologic interpretation cartoon for HLP Line 1 profile. Solid grey lines are well constrained by the seismic data and dashed lines are poorly constained by the seismic data.

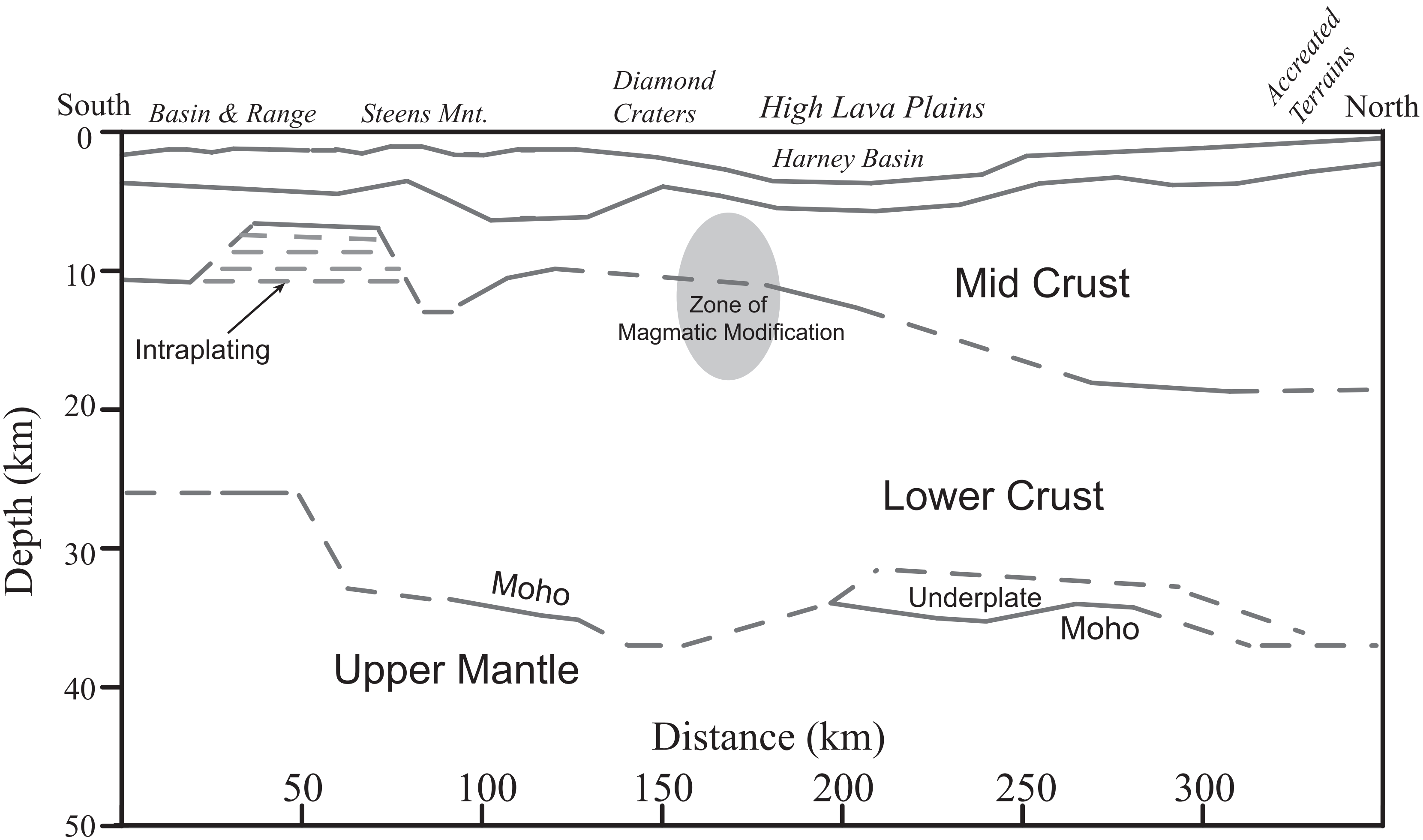

Figure 43. Geologic interpretation cartoon for HLP Line 2 profile. Solid grey lines are well constrained by the seismic data and dashed lines are poorly constained by the seismic data.

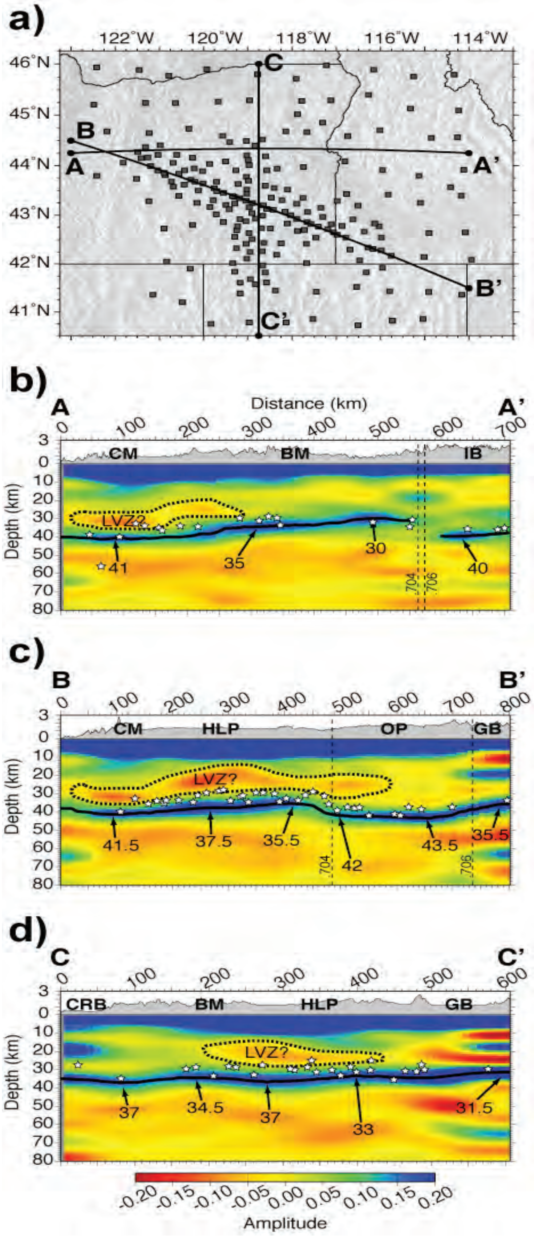

Figure 44. [from *Eagar et al.,* 2010] P-wave velocity models from the HLP reciever function data. Figure b corresponds to Line 1 and figure c corresponds to Line 2. Overall there is good agreement of the crustal thickness between the active- source data and the reciever function data.

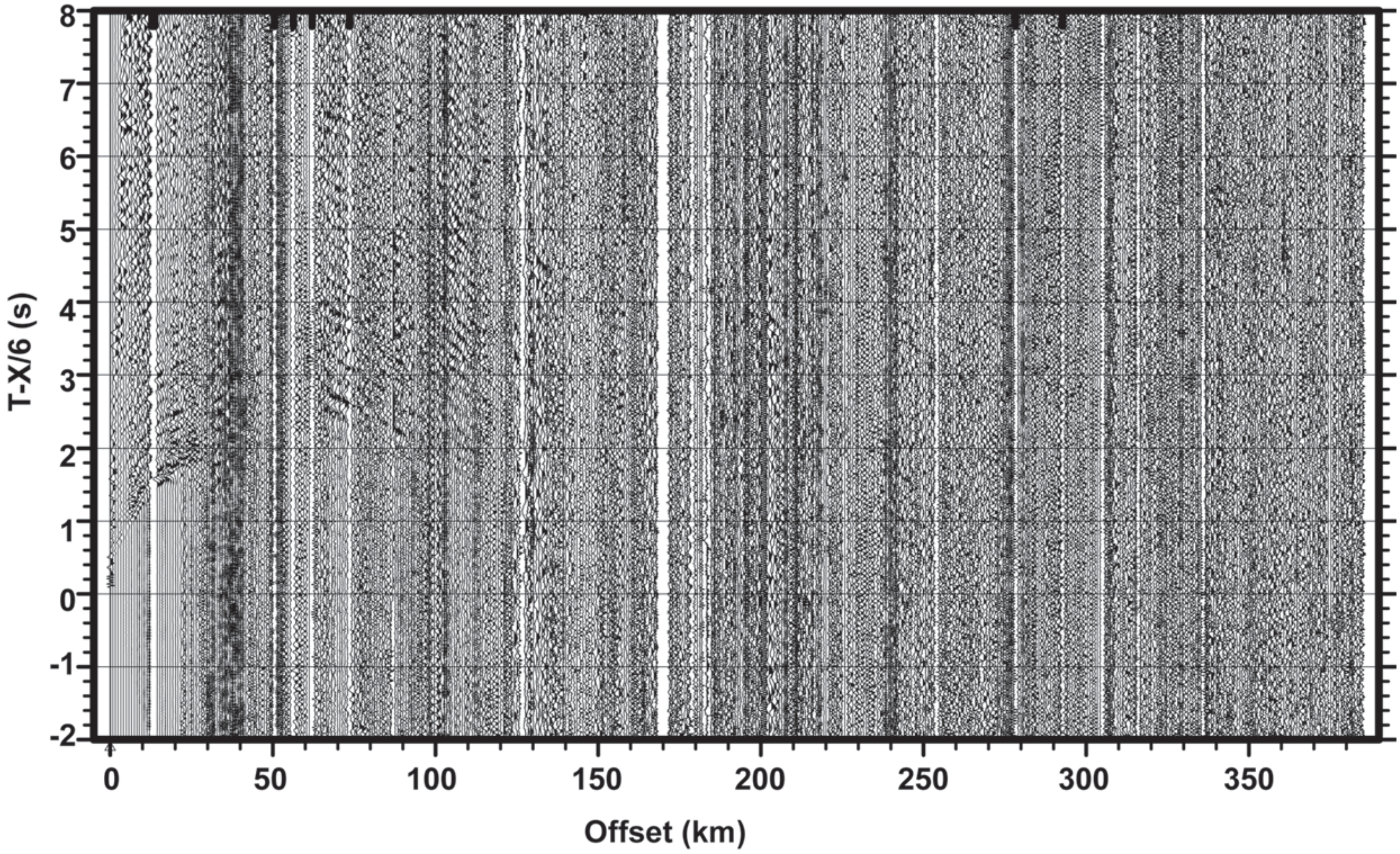

Figure 1. Raw, unfiltered shotgather SP 11.

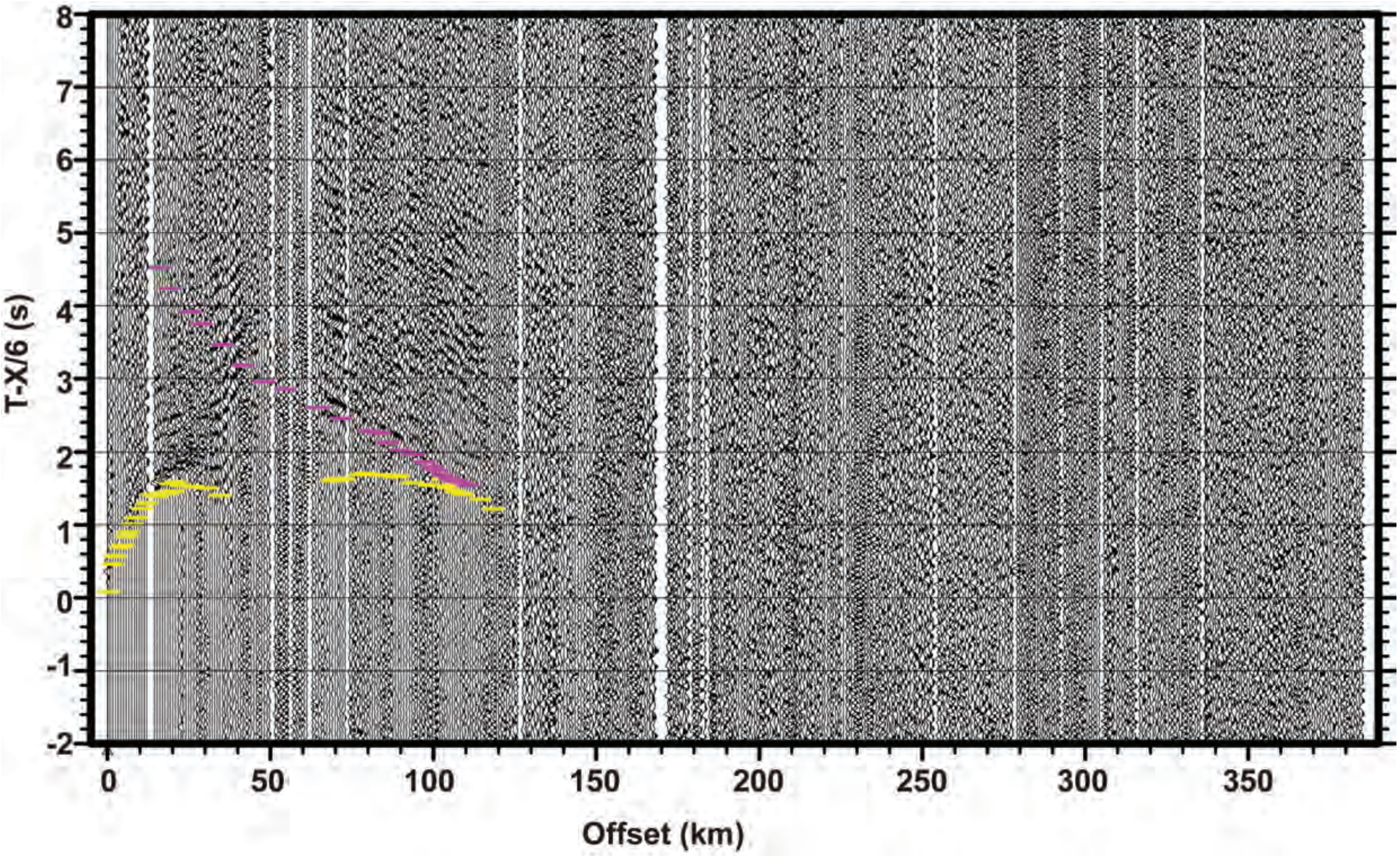

Figure 2. Shotgather SP 11 after applying a 2-4-12-15 Ormsby filter and muting of bad traces. Travel time picks corresponding to Pg (yellow) and PcP (pink).

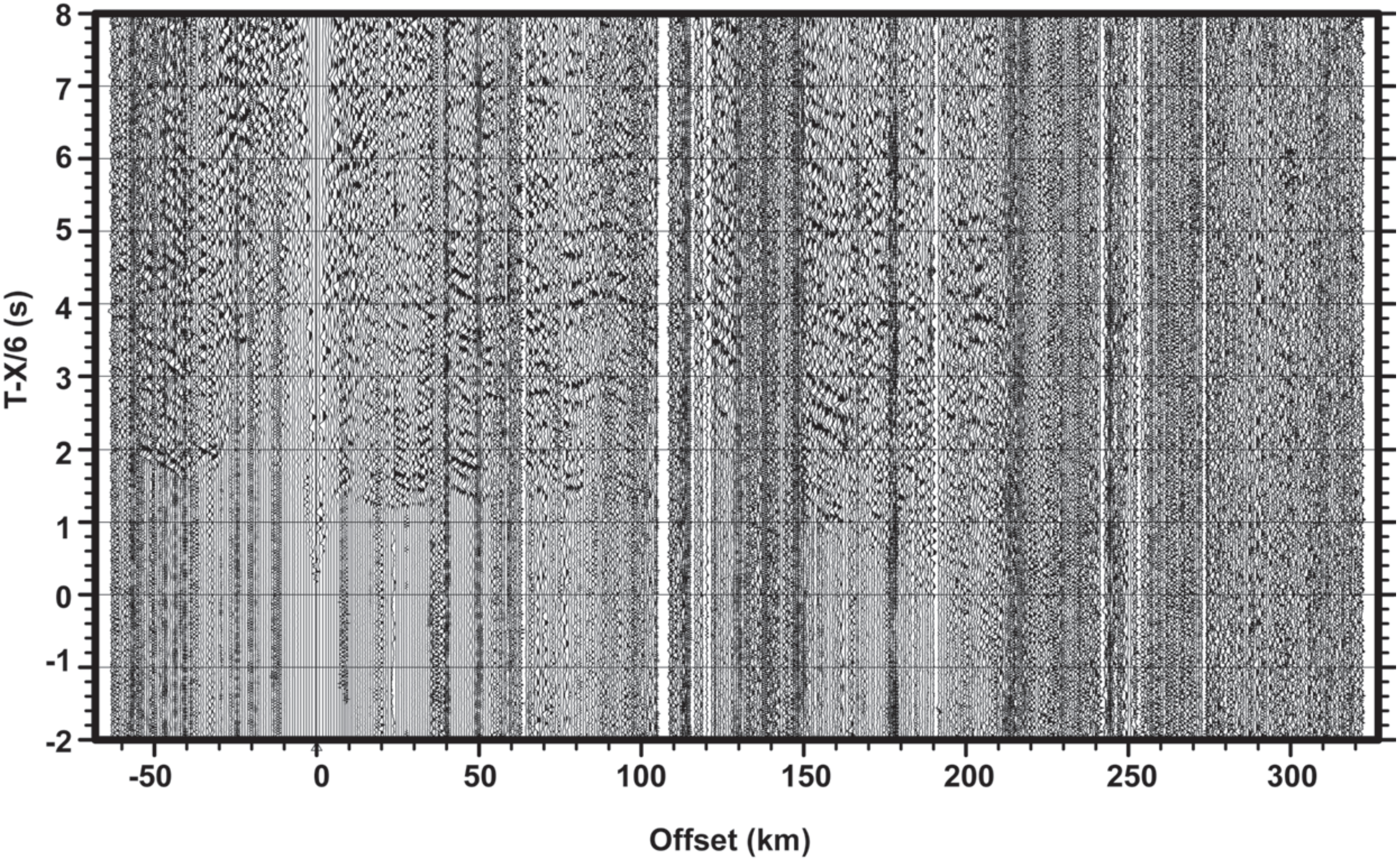

Figure 3. Raw, unfiltered shotgather SP 12.

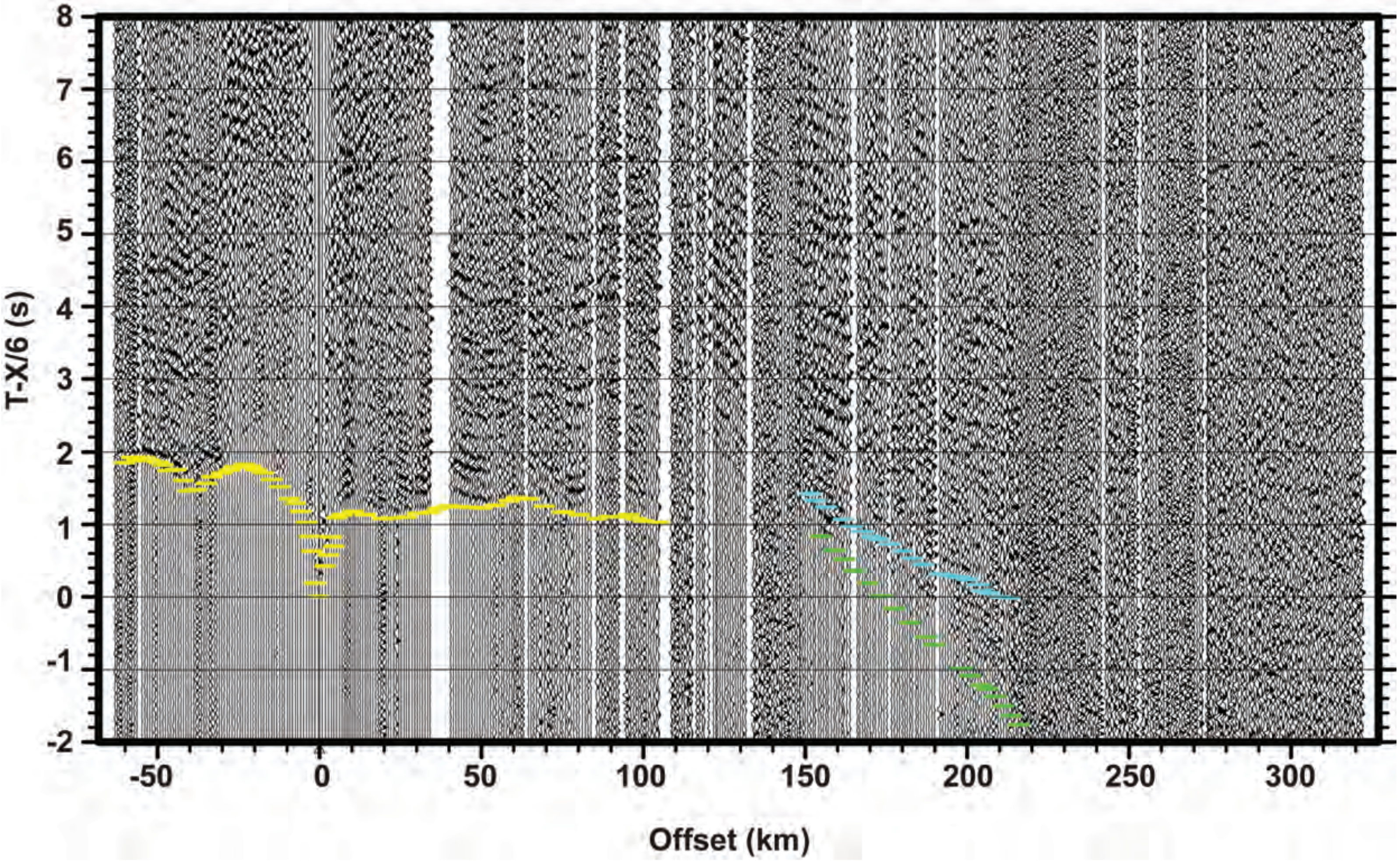

Figure 4. Shotgather SP 12 after applying a 2-4-12-15 Ormsby filter and muting of bad traces. Travel time picks corresponding to Pg (yellow), PmP (light blue), and Pn (green) events.

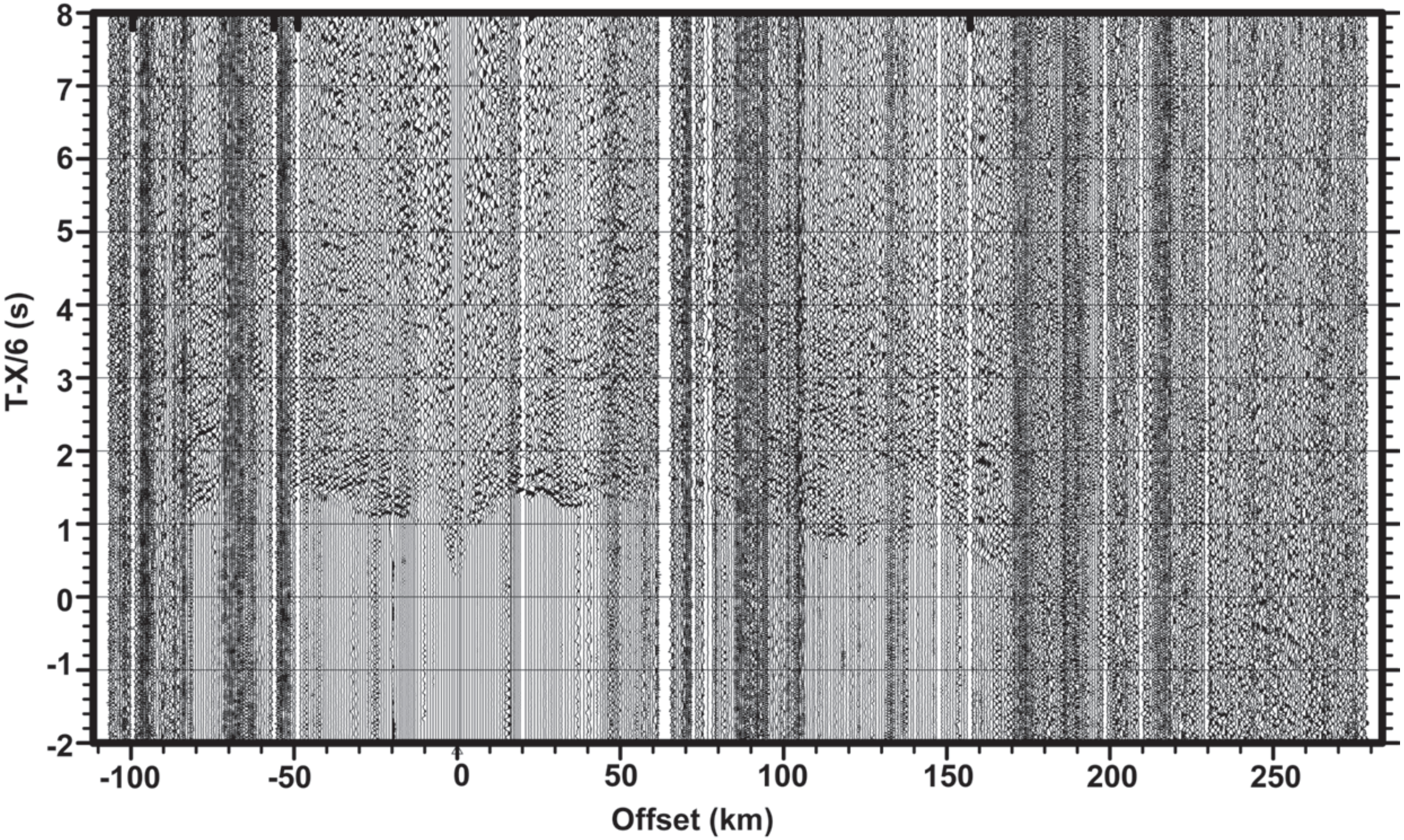

Figure 5. Raw, unfiltered shotgather SP 13.

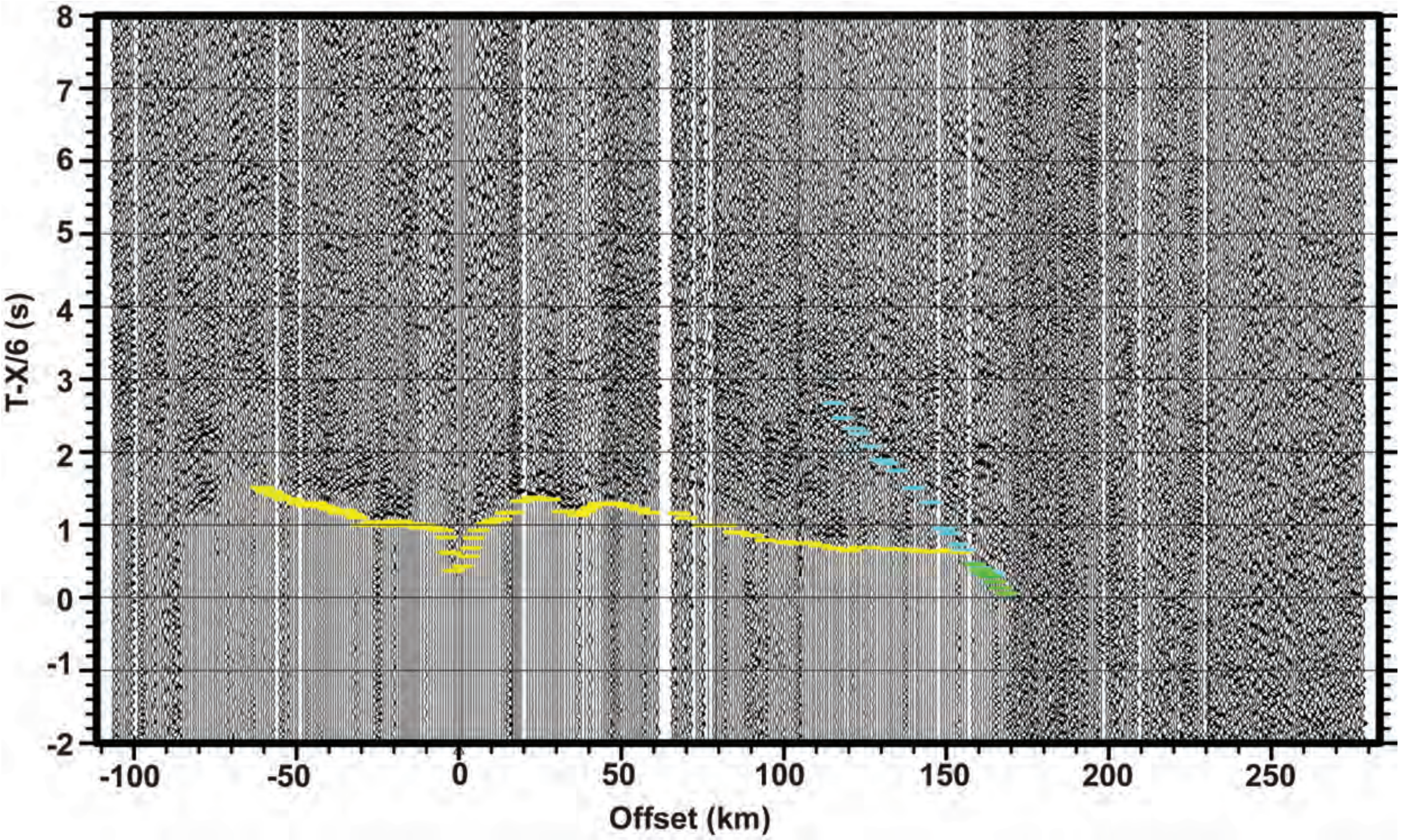

Figure 6. Shotgather SP 13 after applying a 2-4-12-15 Ormsby filter and muting of bad traces. Travel time picks corresponding to Pg (yellow), PmP (light blue), and Pn (green) events.

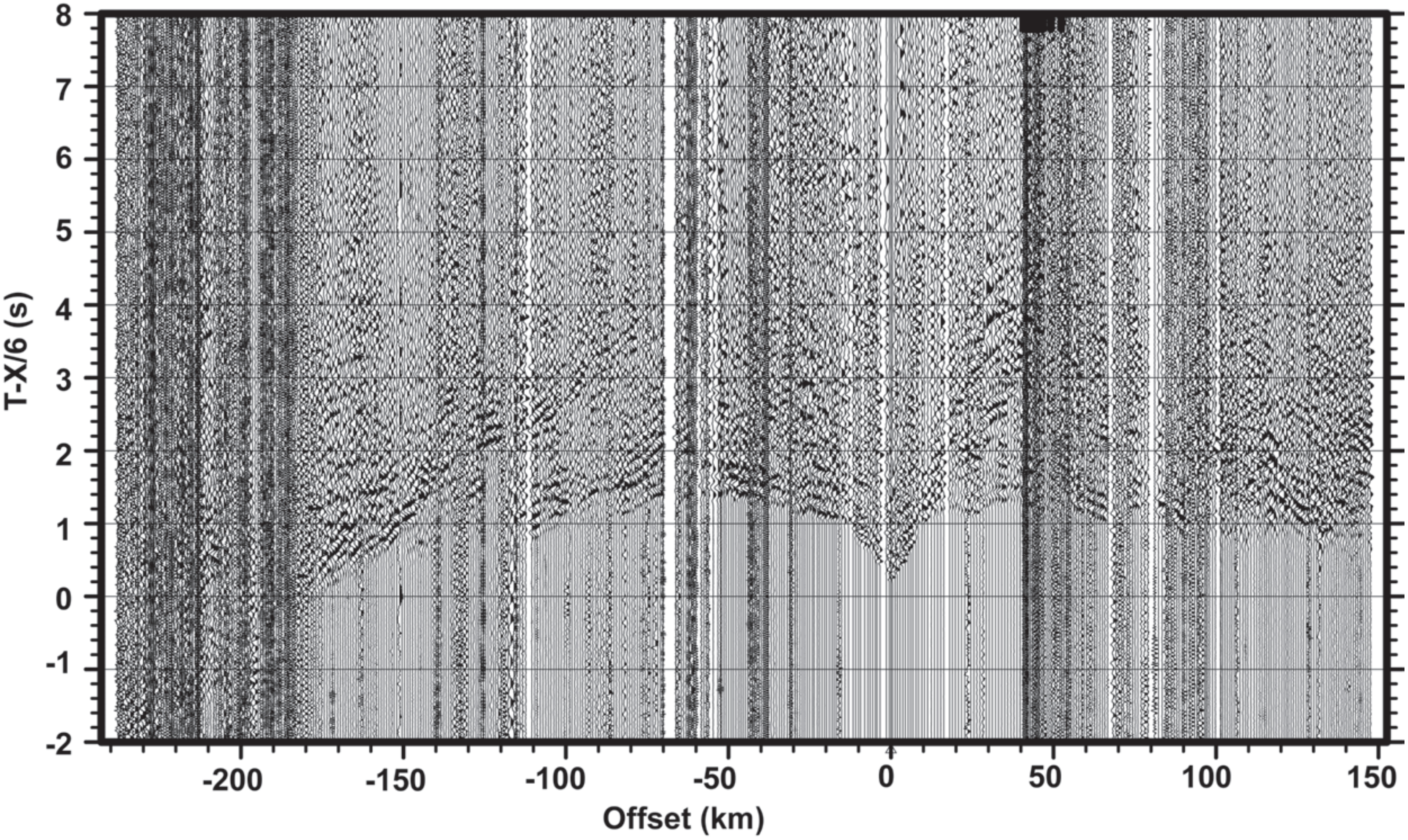

Figure 7. Raw, unfiltered shotgather SP 15.

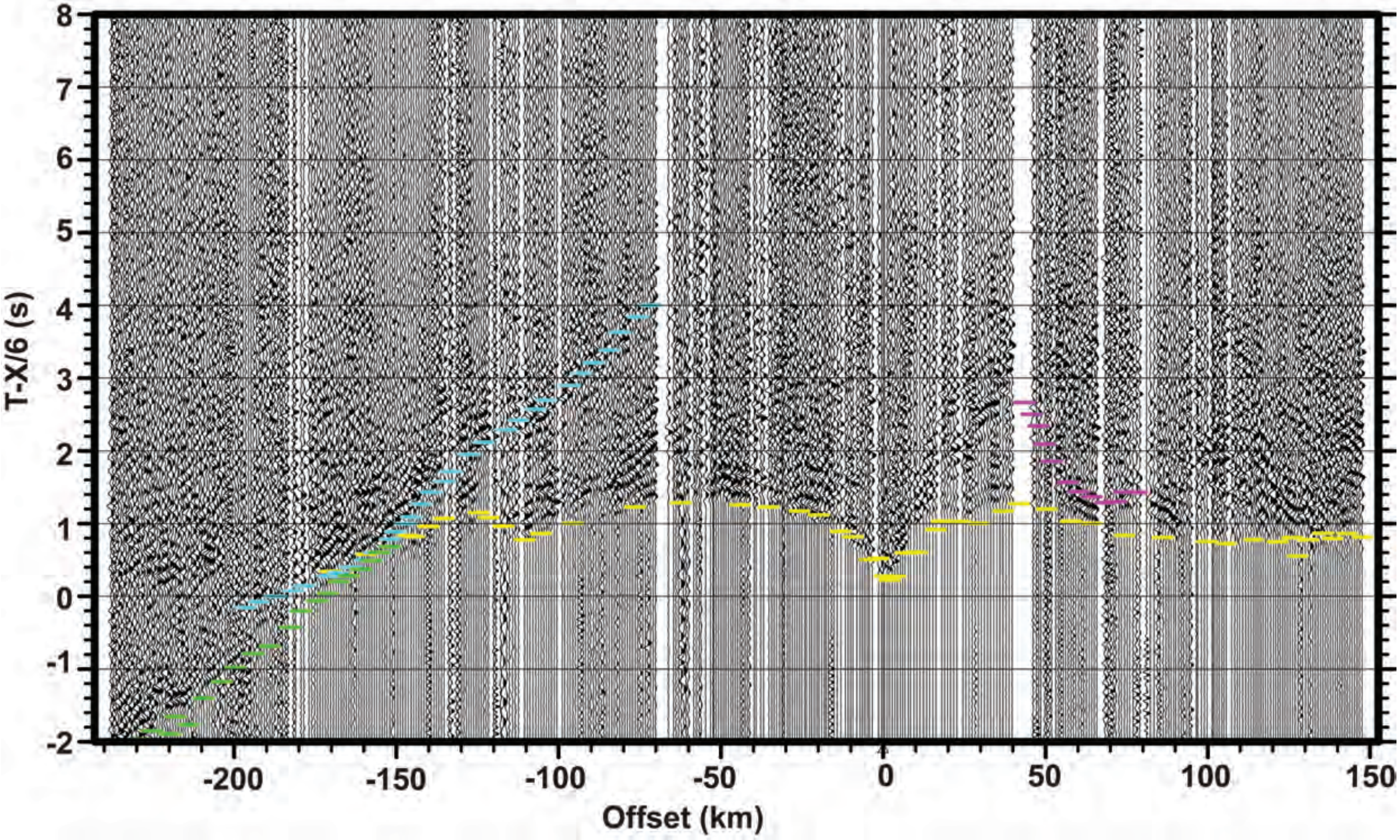

Figure 8. Shotgather SP 15 after applying a 2-4-12-15 Ormsby filter and muting of bad traces. Travel time picks corresponding to Pg (yellow), PcP (pink), PmP (light blue), and Pn (green) events.

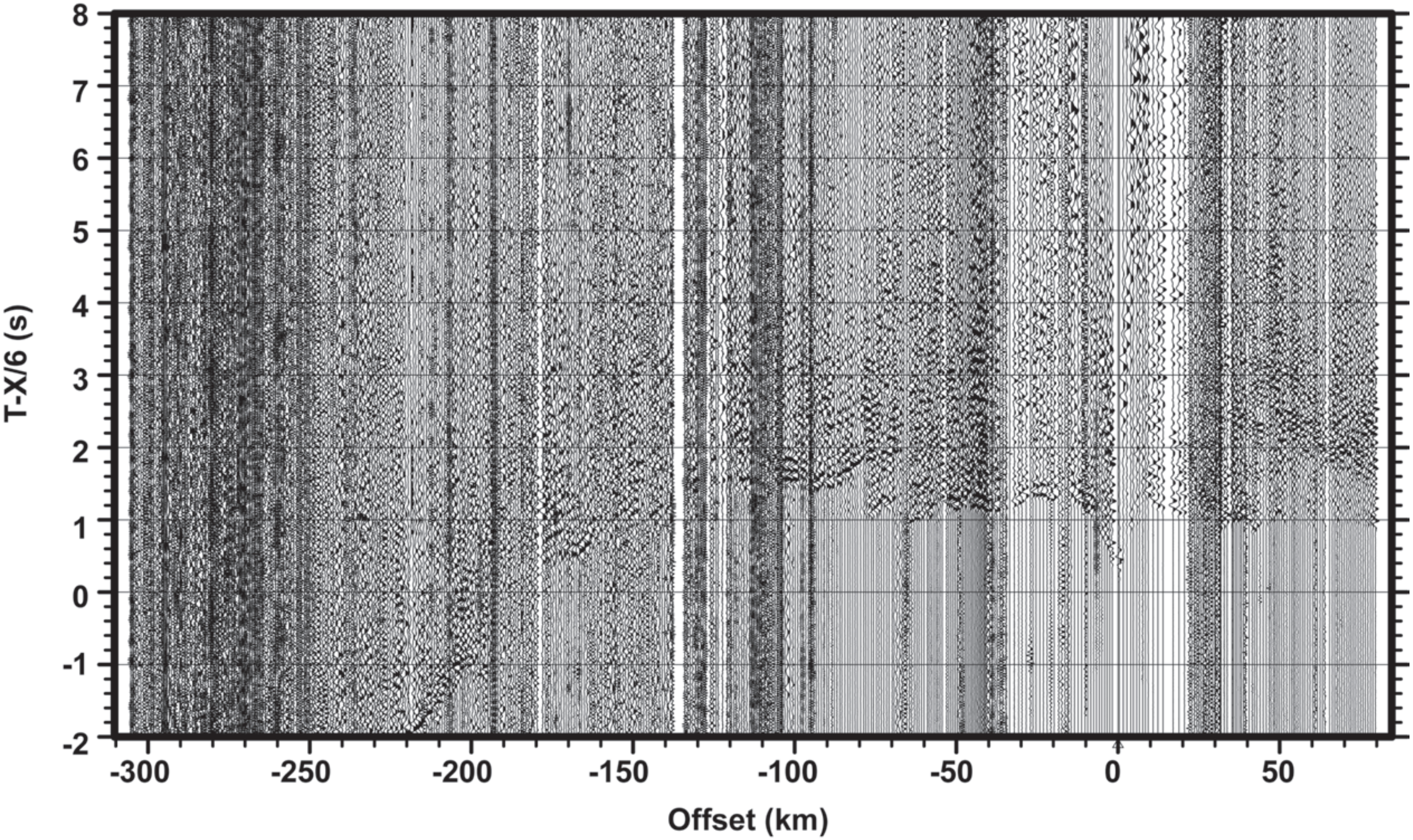

Figure 9. Raw, unfiltered shotgather SP 16.

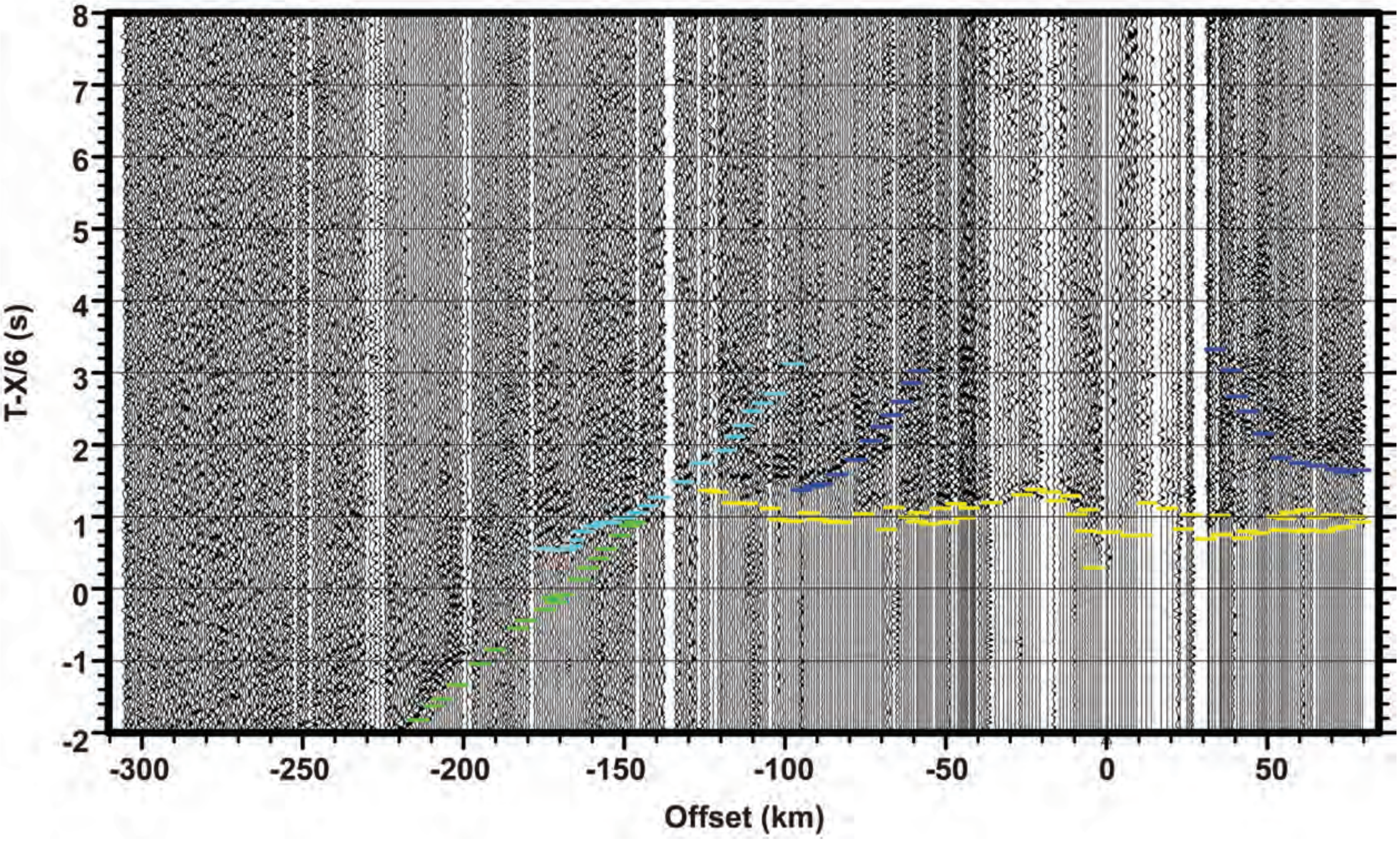

Figure 10. Shotgather SP 16 after applying a 2-4-12-15 Ormsby filter and muting of bad traces. Travel time picks corresponding to Pg (yellow), PcP (dark blue), PmP (light blue), and Pn (green) events.

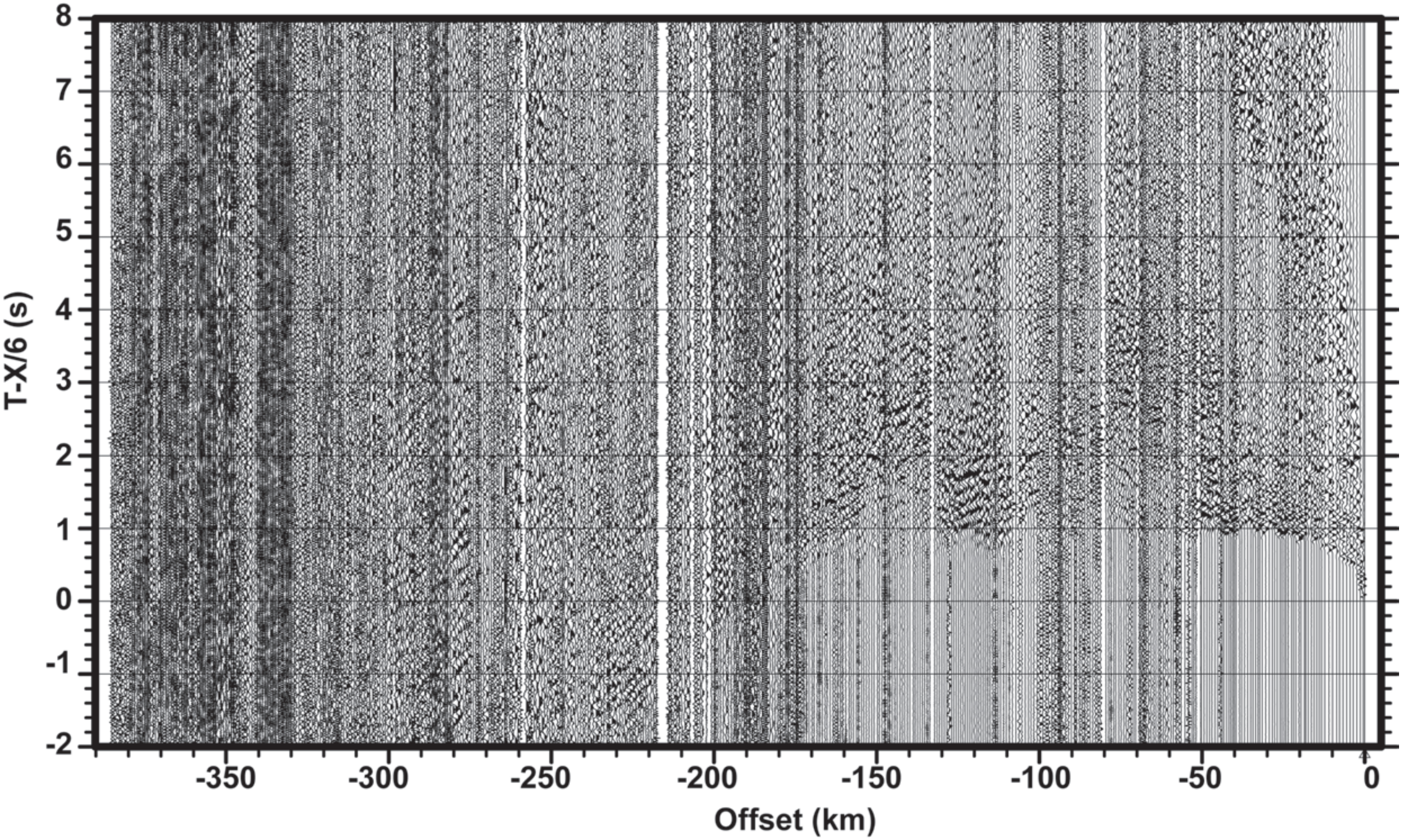

Figure 11. Raw, unfiltered shotgather SP 17.

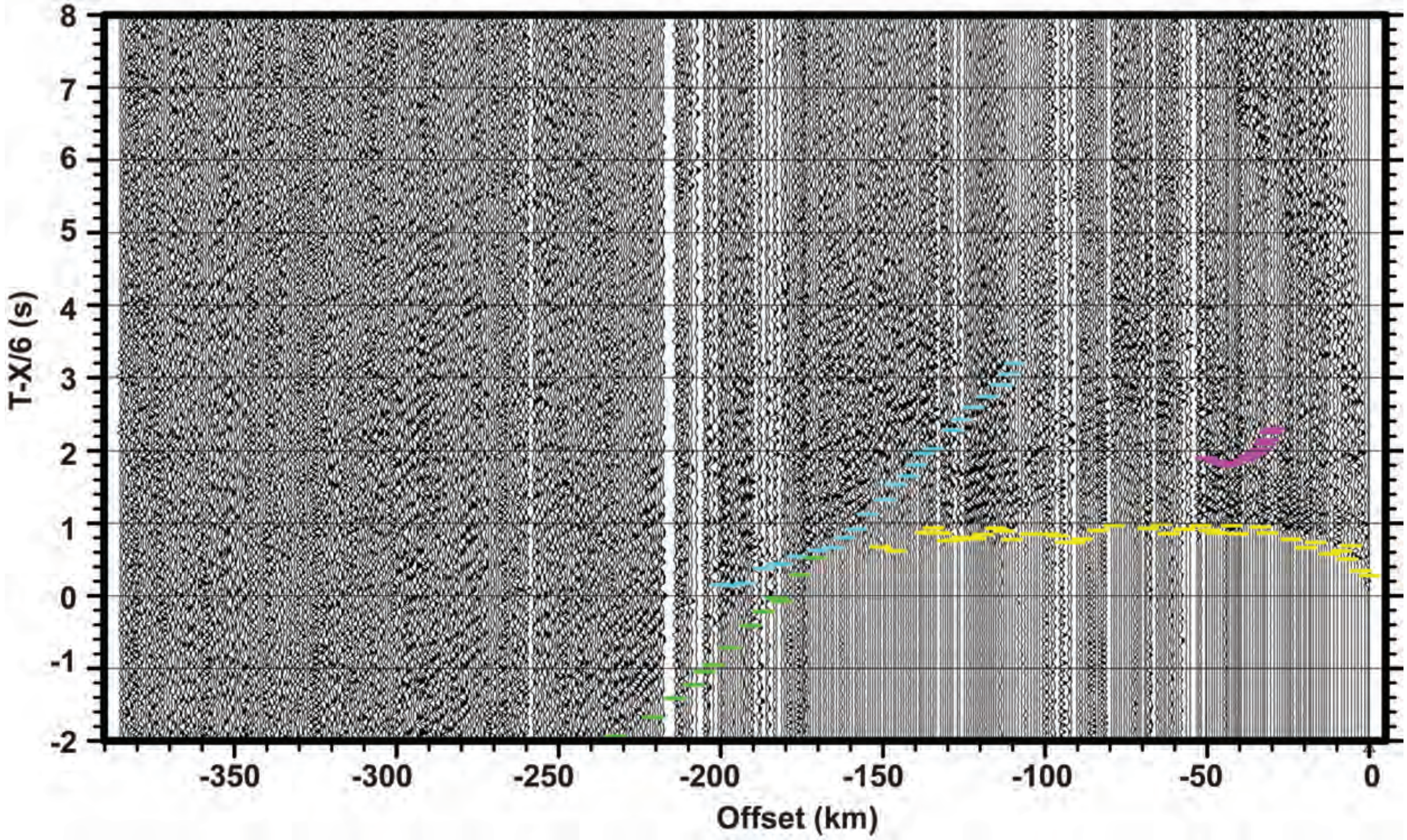

Figure 12. Shotgather SP 17 after applying a 2-4-12-15 Ormsby filter and muting of bad traces. Travel time picks corresponding to Pg (yellow), PcP (pink), PmP (light blue), and Pn (green) events.

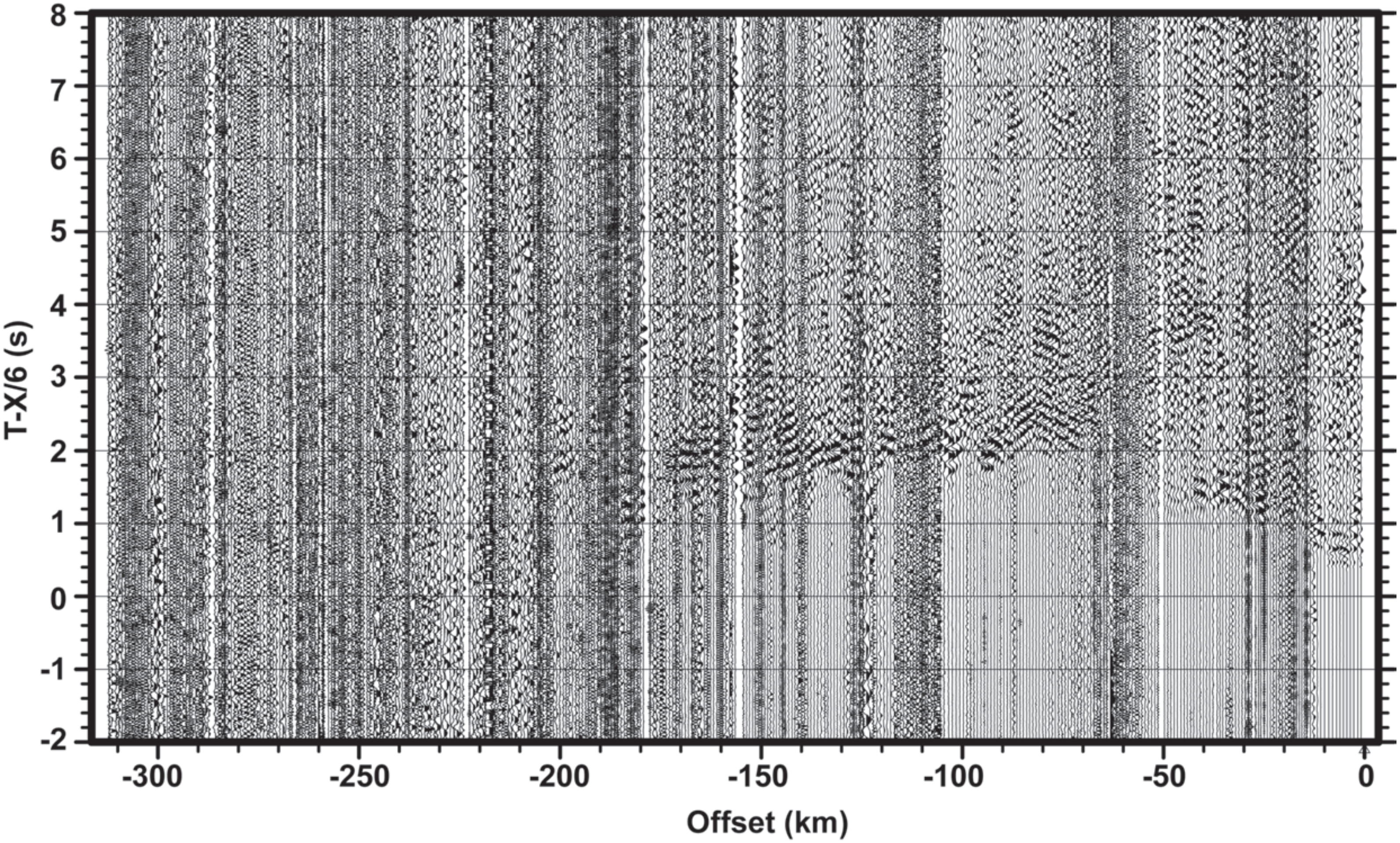

Figure 13. Raw, unfiltered shotgather SP 21.

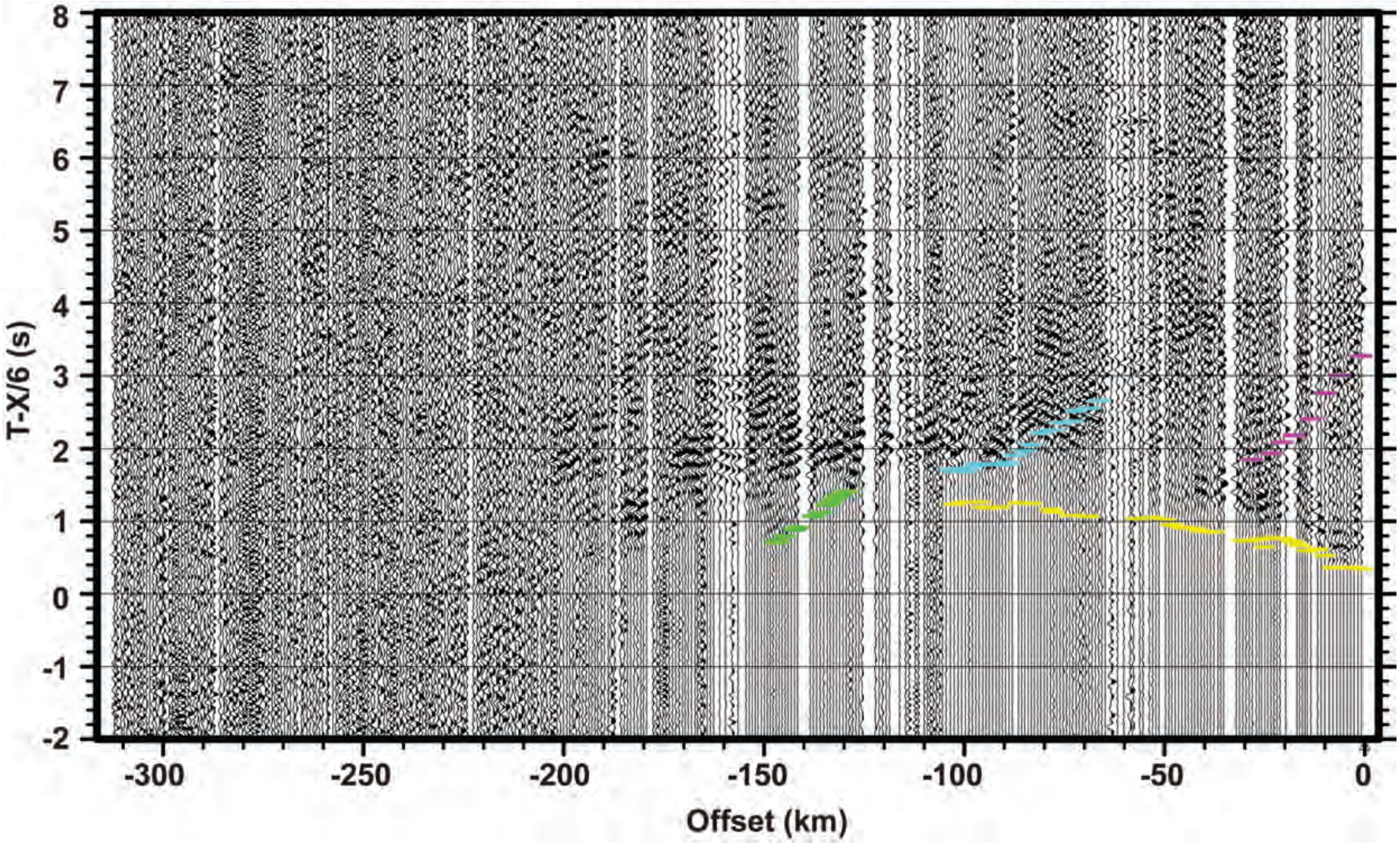

Figure 14. Shotgather SP 21 after applying a 2-4-12-15 Ormsby filter and muting of bad traces. Travel time picks corresponding to Pg (yellow), PcP (pink), PmP (light blue), and Pn (green) events.

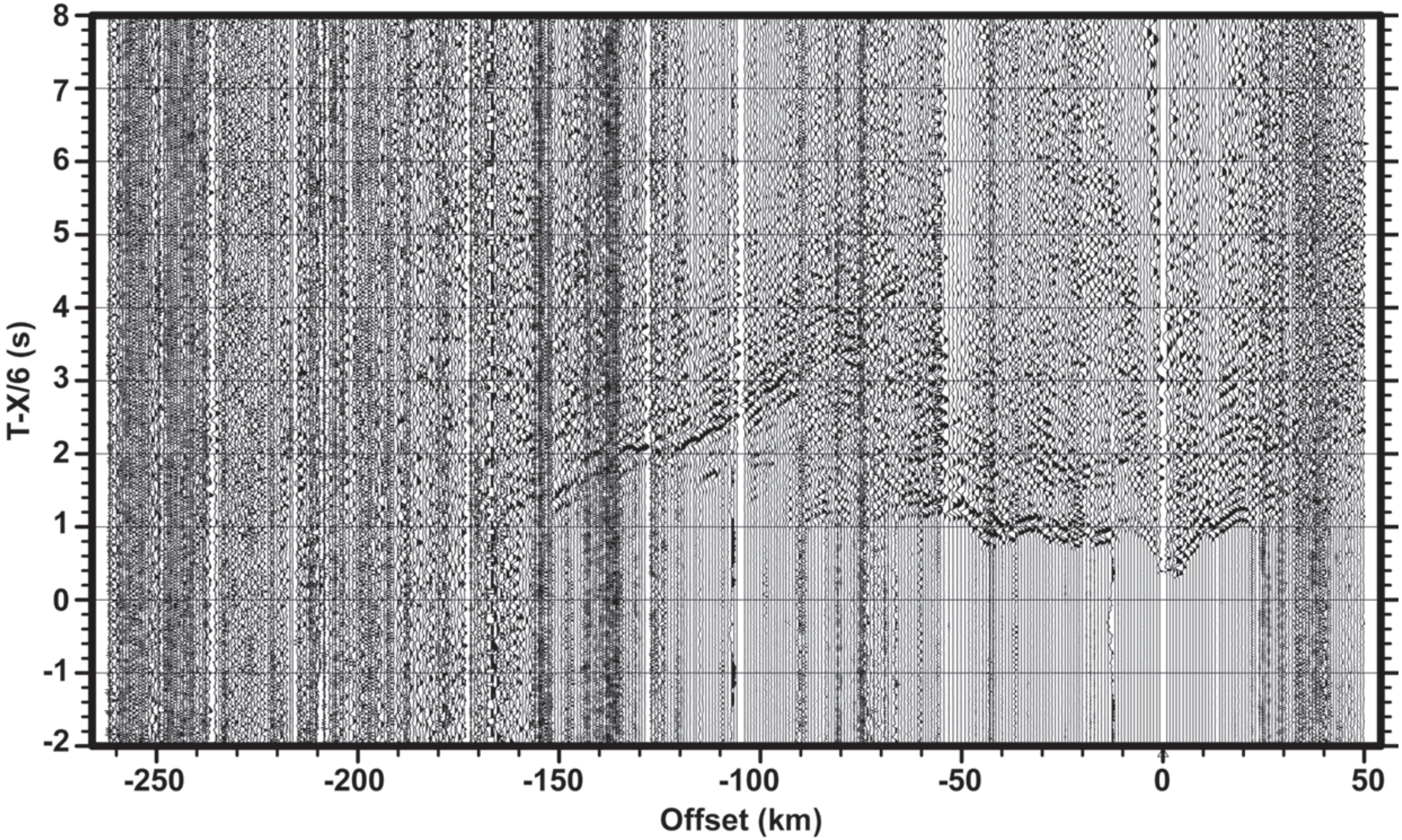

Figure 15. Raw, unfiltered shotgather SP 22.

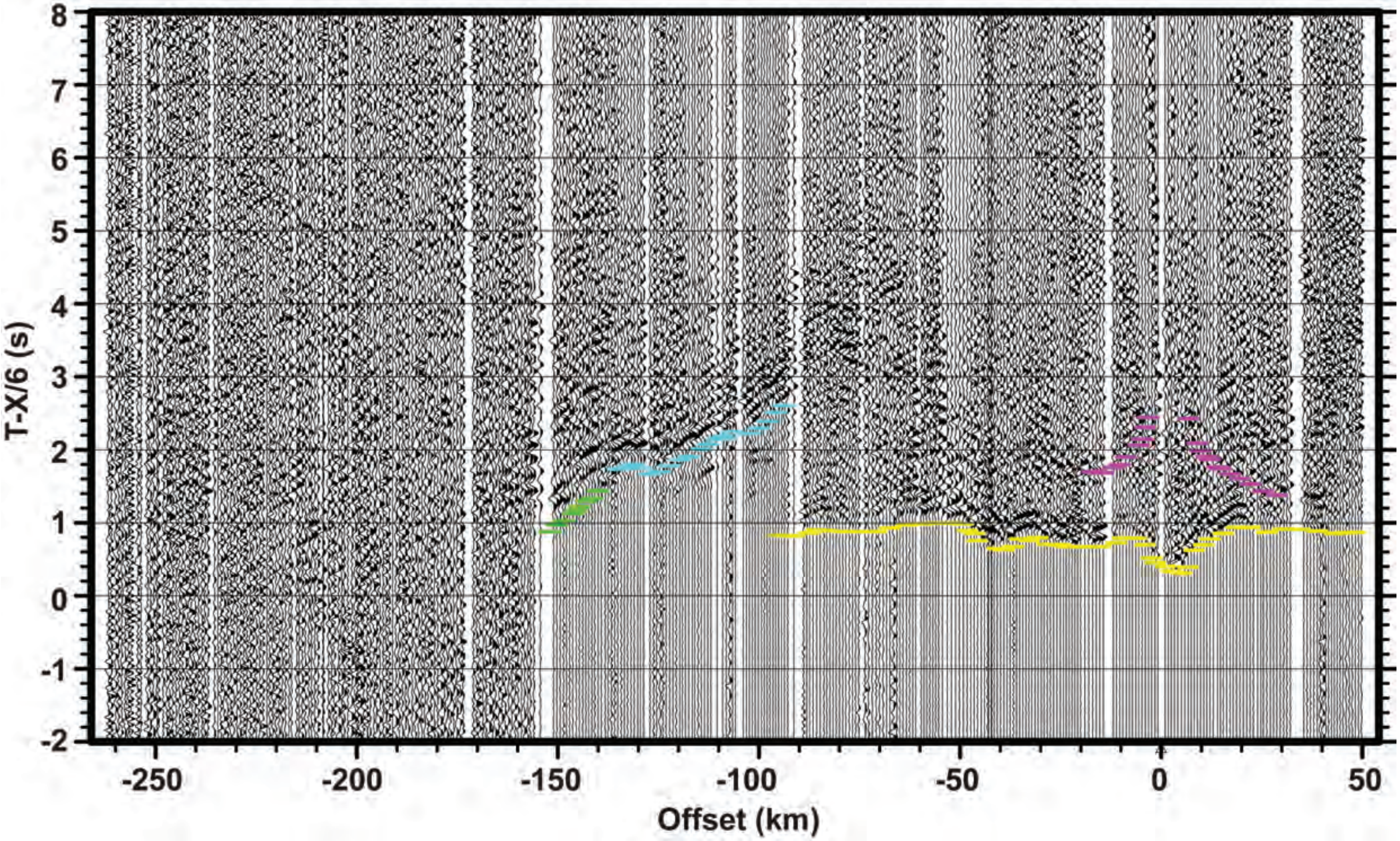

Figure 16. Shotgather SP 22 after applying a 2-4-12-15 Ormsby filter and muting of bad traces. Travel time picks corresponding to Pg (yellow), PcP (pink), PmP (light blue), and Pn (green) events.

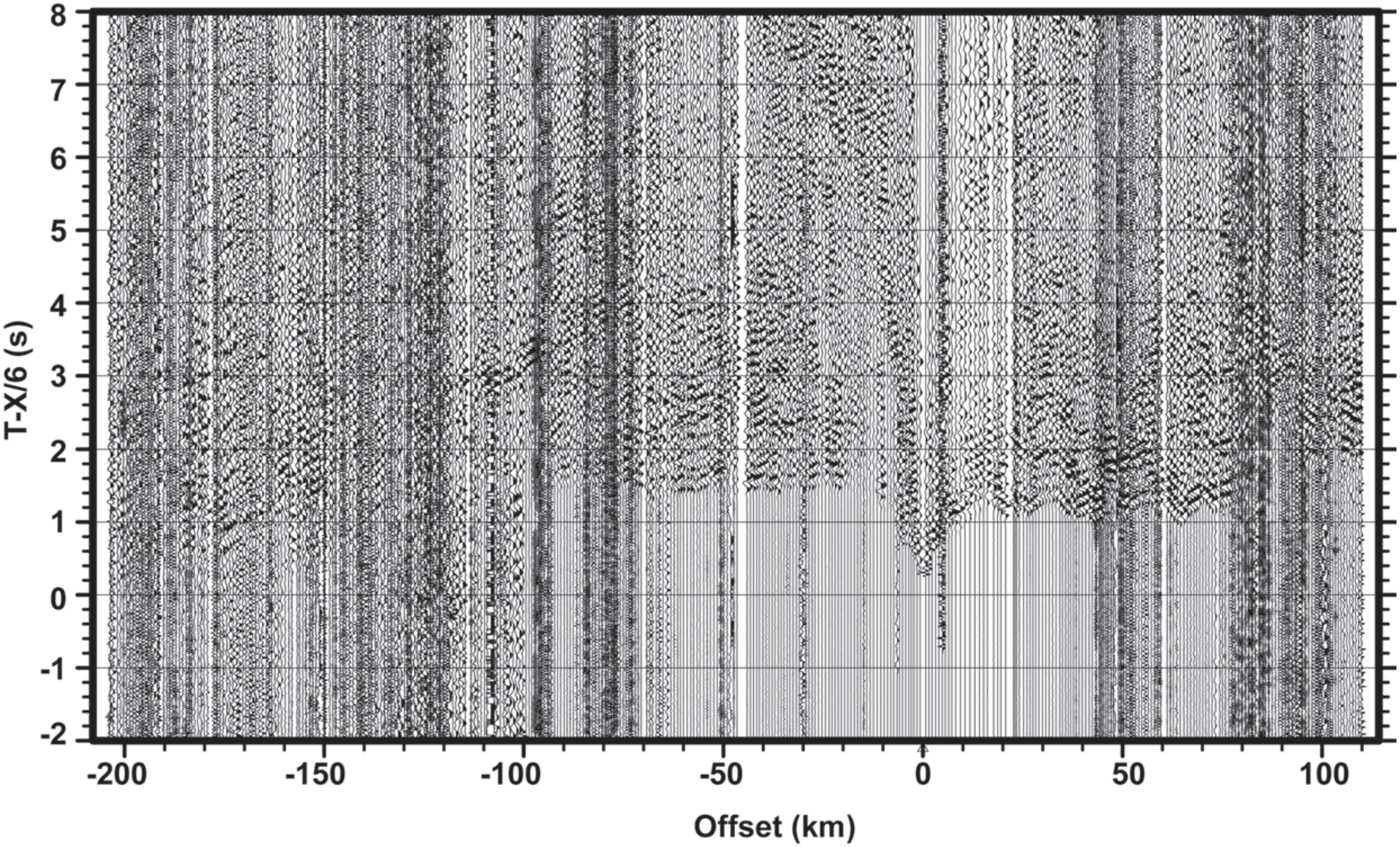

Figure 17. Raw, unfiltered shotgather SP 23.

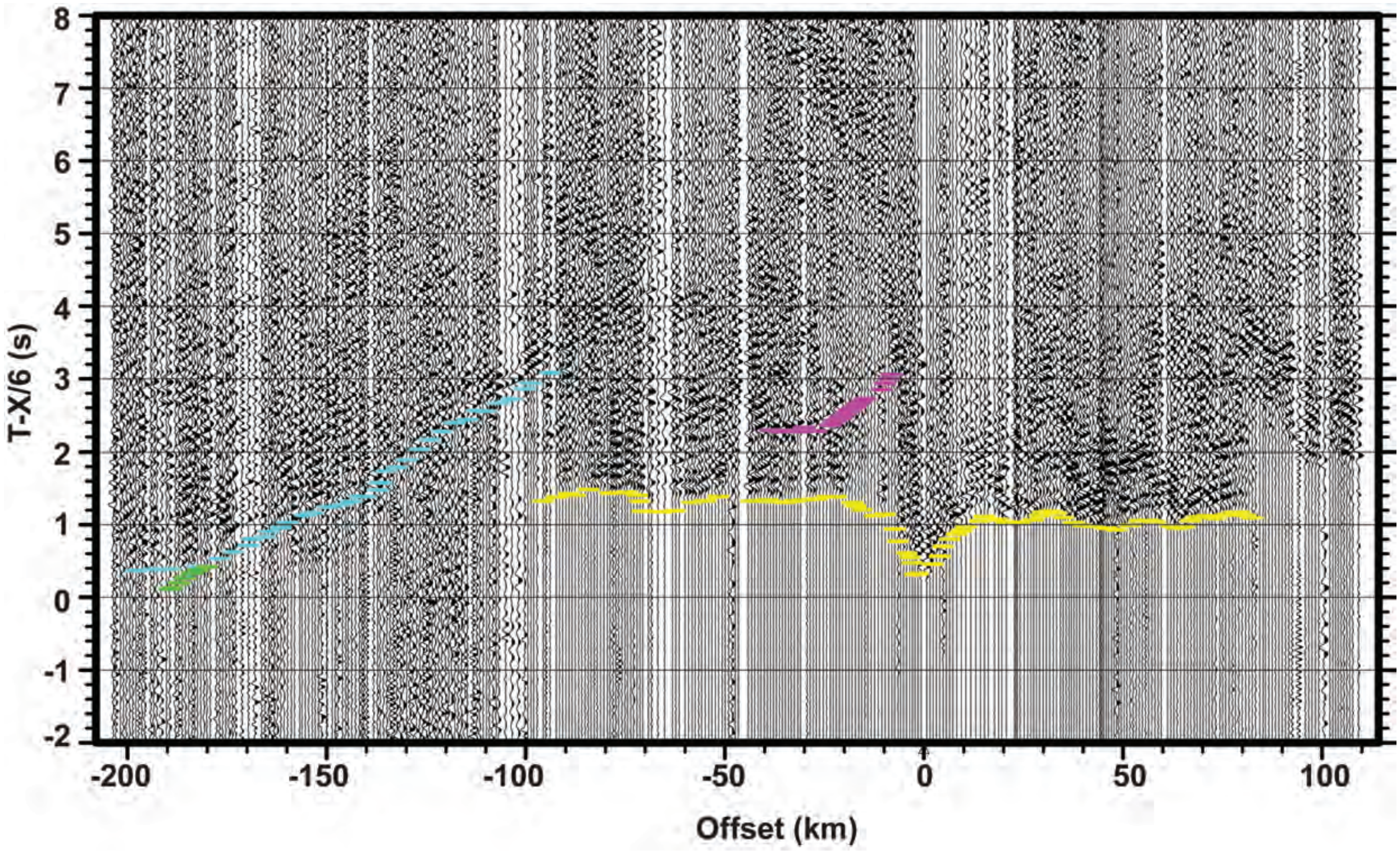

Figure 18. Shotgather SP 23 after applying a 2-4-12-15 Ormsby filter and muting of bad traces. Travel time picks corresponding to Pg (yellow), PcP (pink), PmP (light blue), and Pn (green) events.

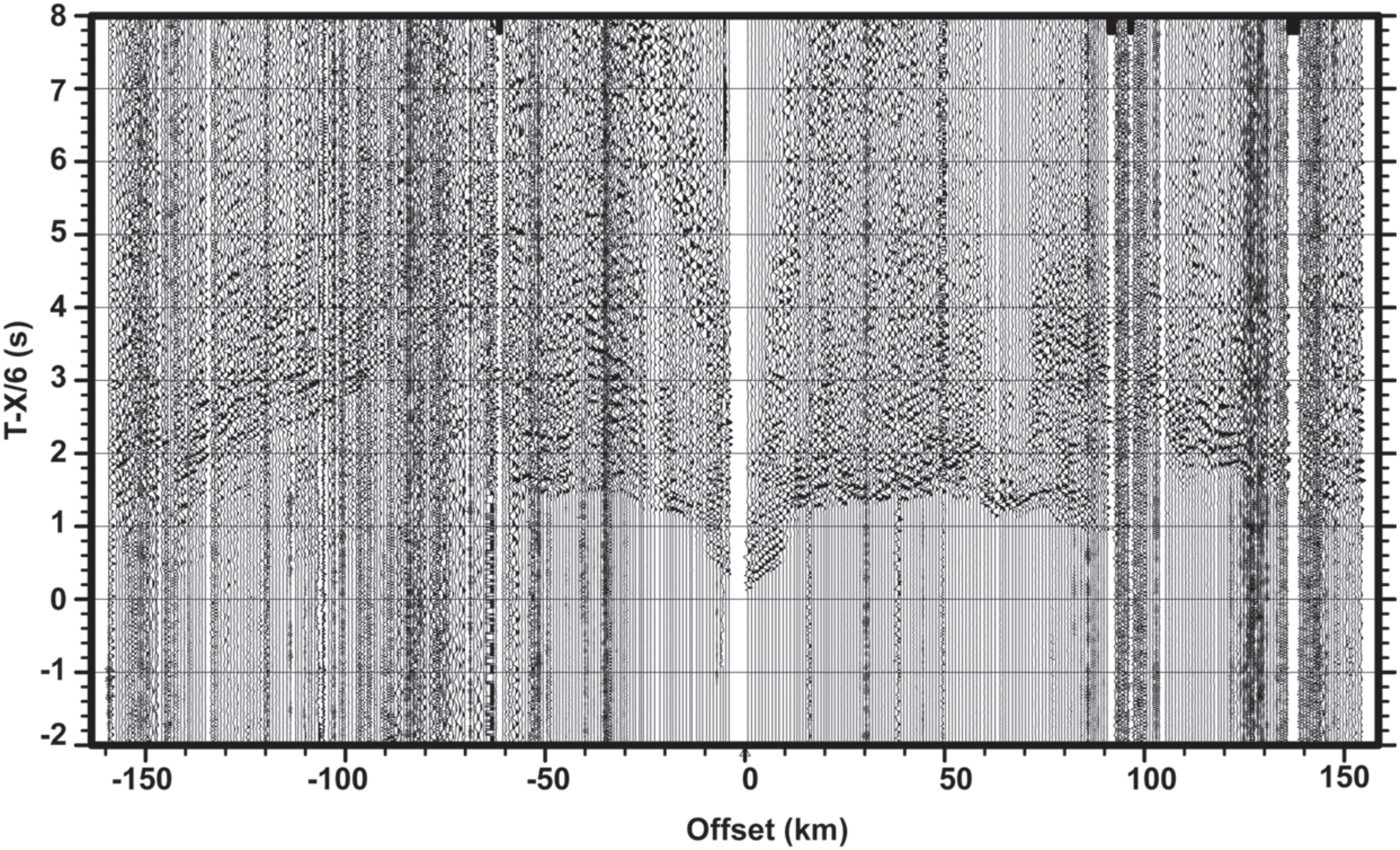

Figure 19. Raw, unfiltered shotgather SP 24.

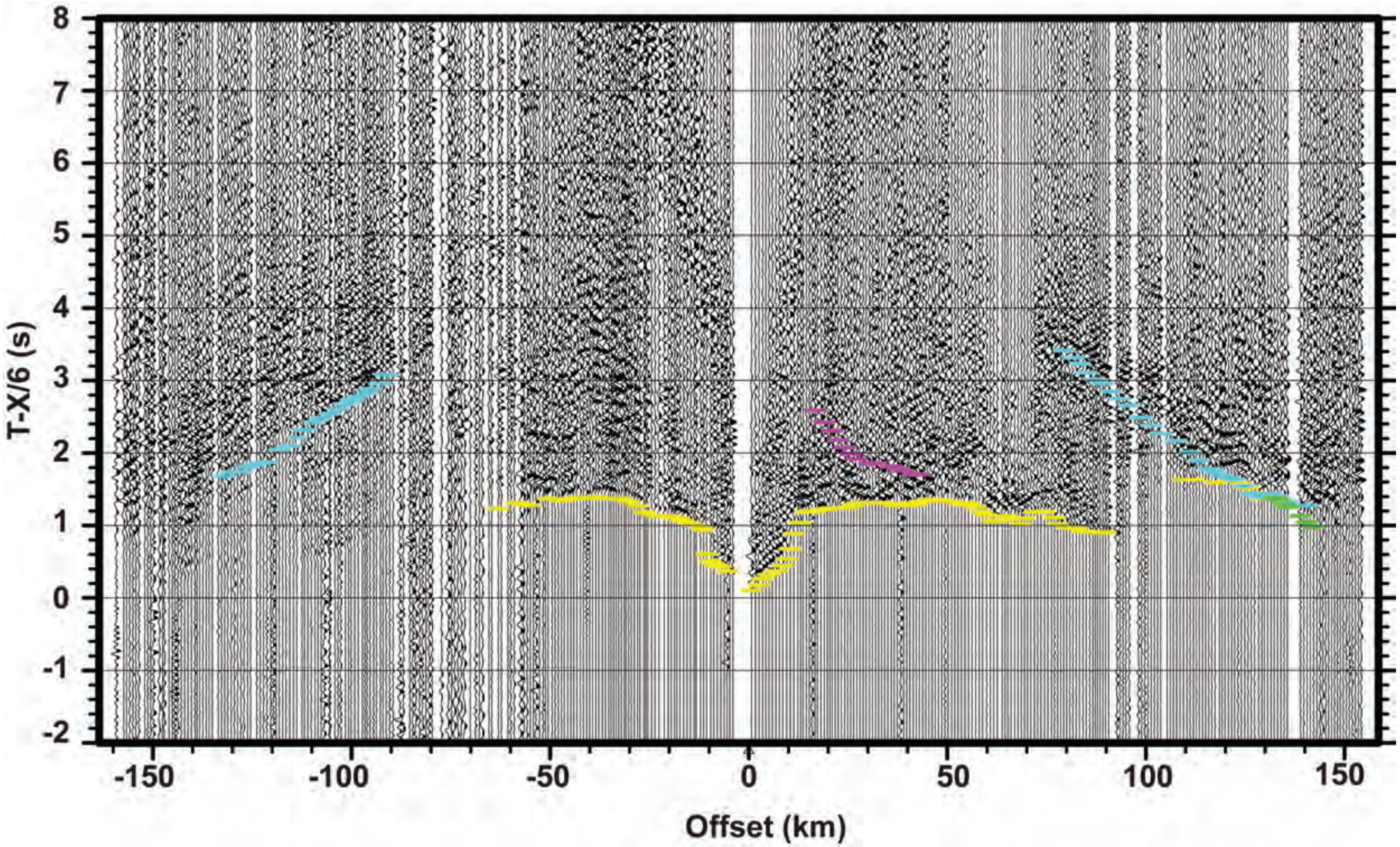

Figure 20. Shotgather SP 24 after applying a 2-4-12-15 Ormsby filter and muting of bad traces. Travel time picks corresponding to Pg (yellow), PcP (pink), PmP (light blue), and Pn (green) events.

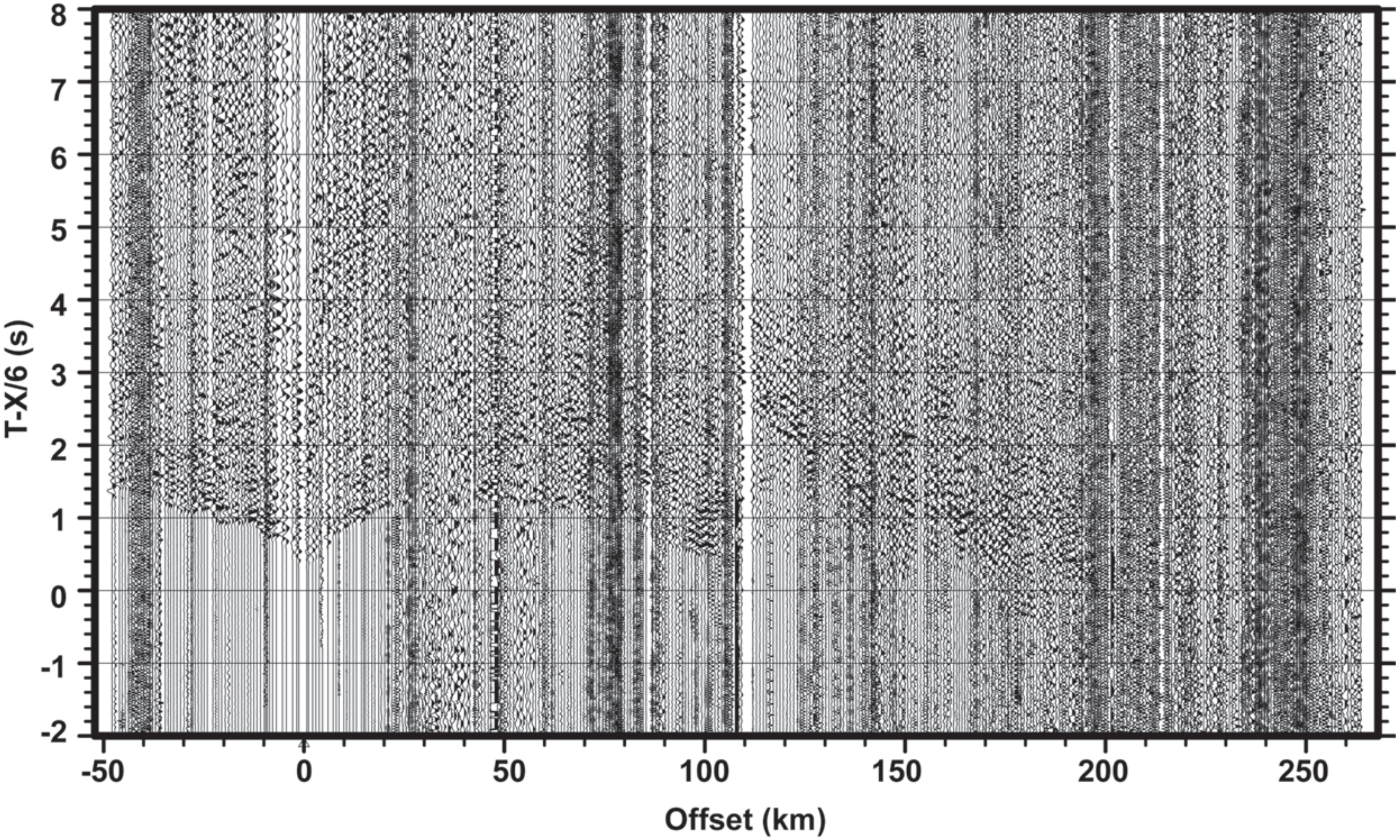

Figure 21. Raw, unfiltered shotgather SP 26.

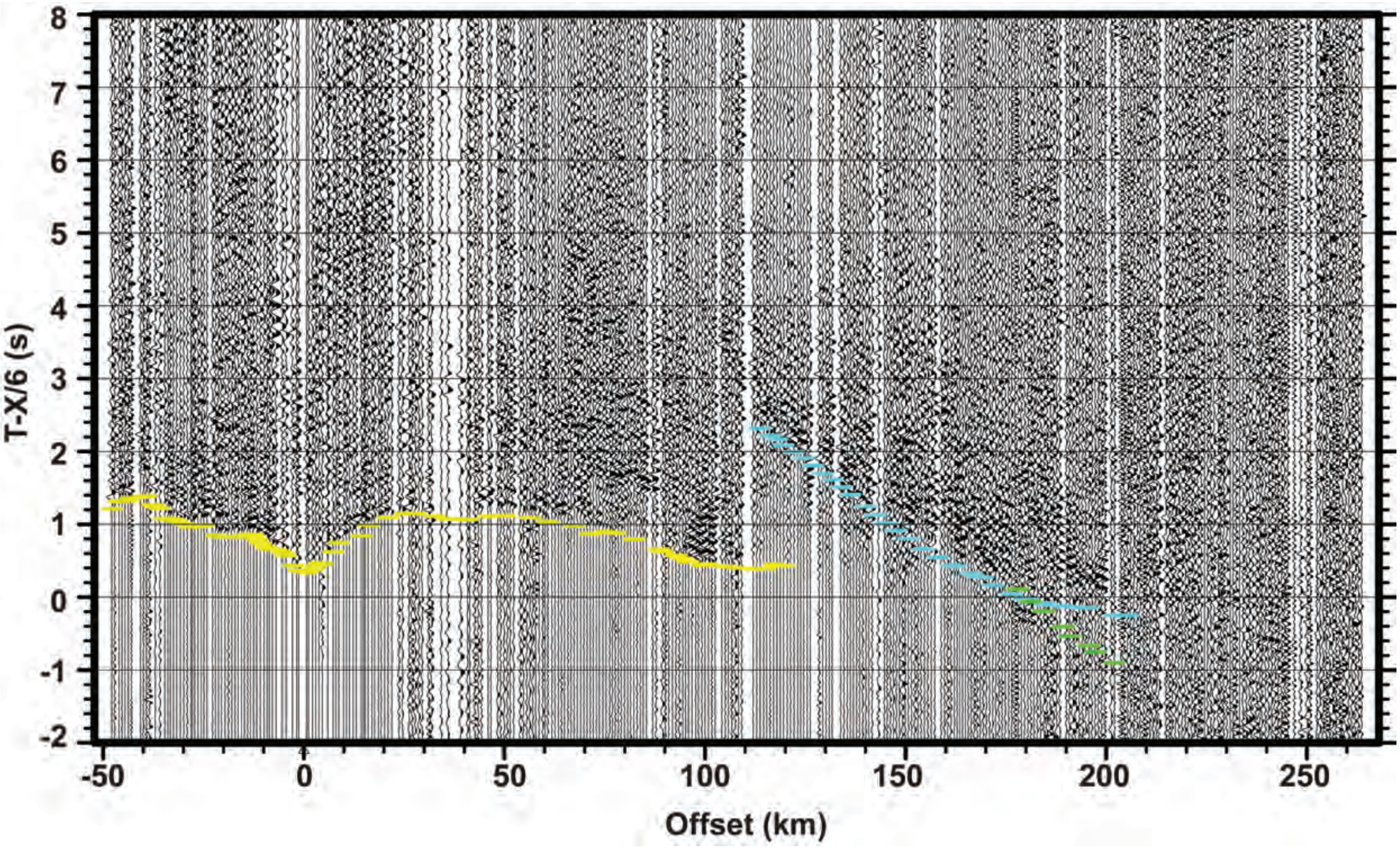

Figure 22. Shotgather SP 26 after applying a 2-4-12-15 Ormsby filter and muting of bad traces. Travel time picks corresponding to Pg (yellow), PmP (light blue), and Pn (green) events.

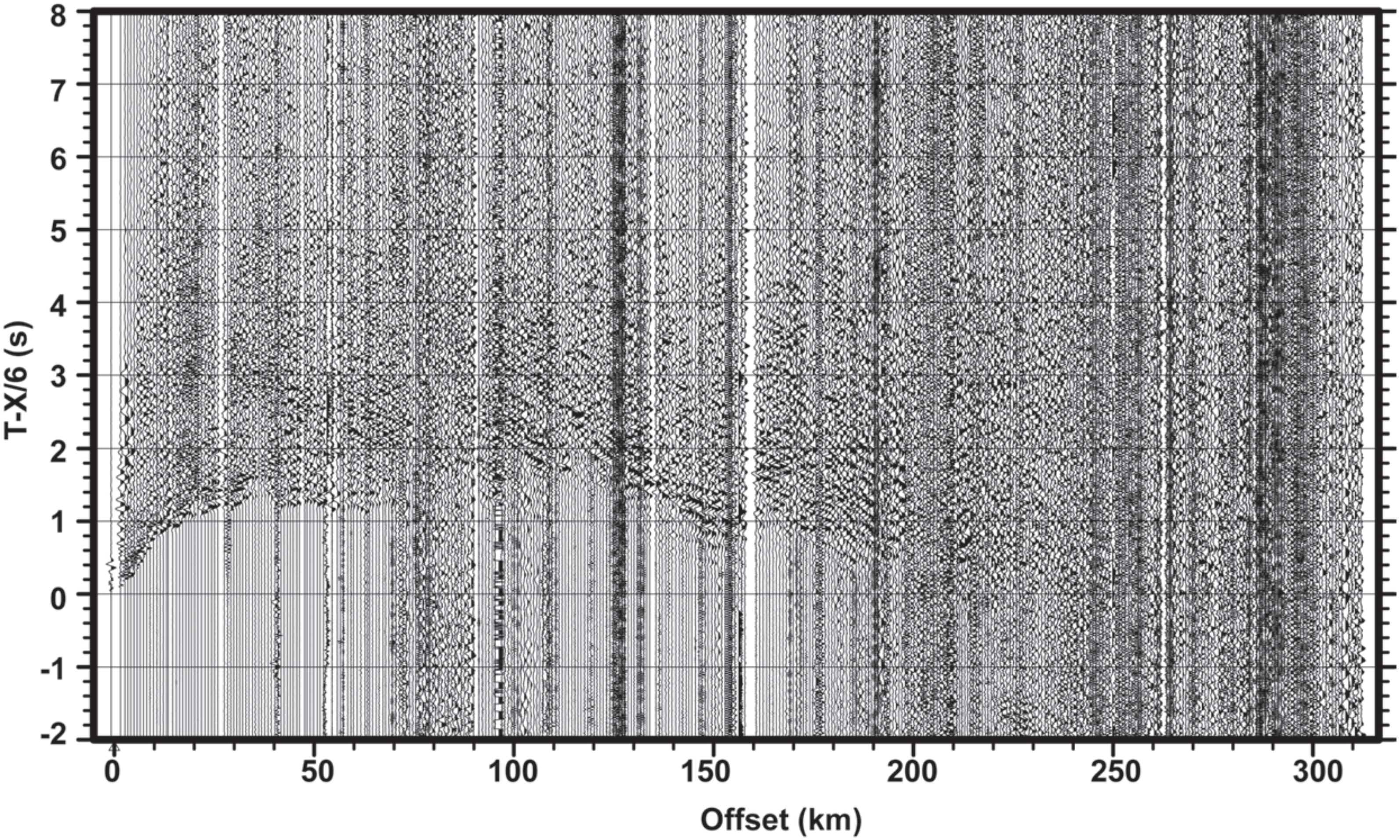

Figure 23. Raw, unfiltered shotgather SP 27.

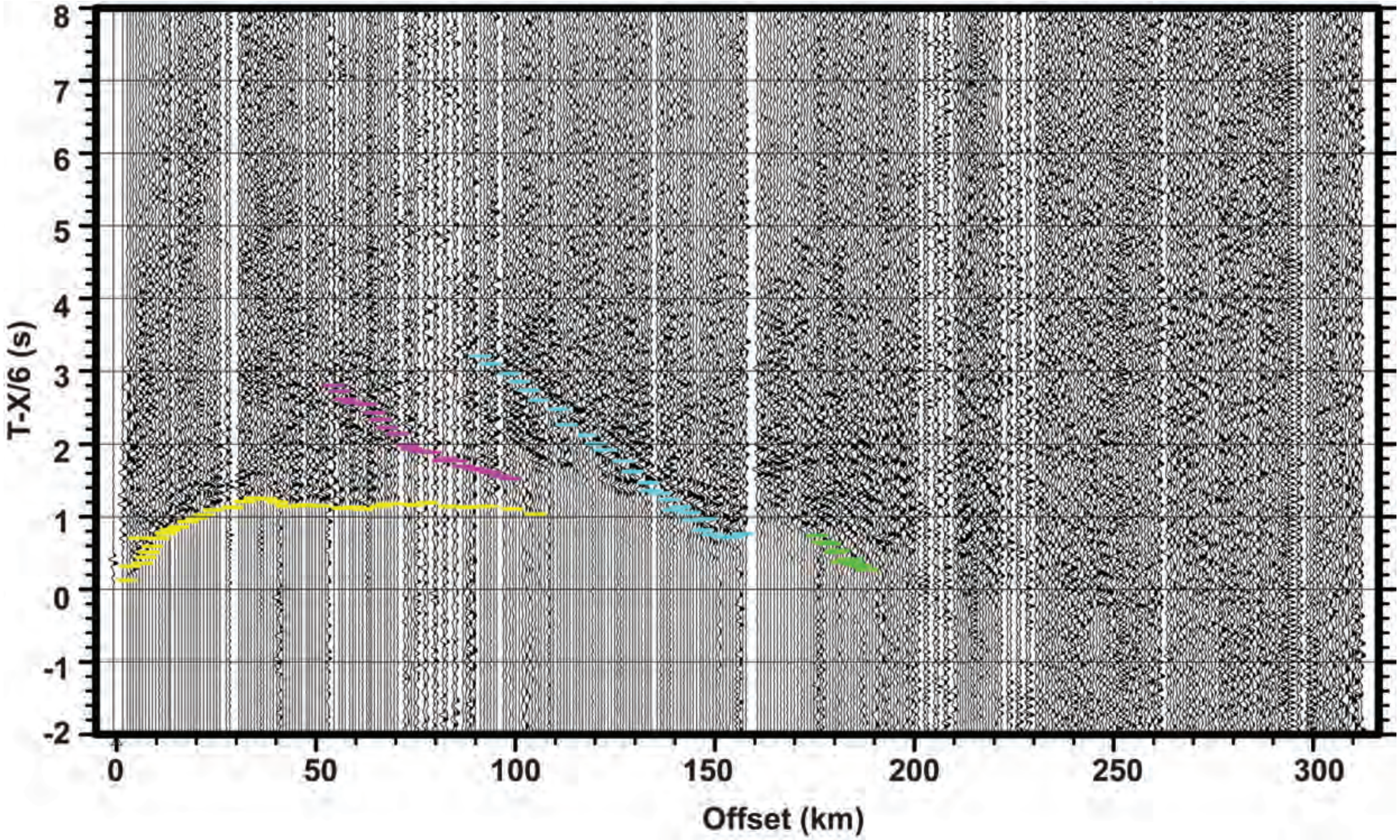

Figure 24. Shotgather SP 27 after applying a 2-4-12-15 Ormsby filter and muting of bad traces. Travel time picks corresponding to Pg (yellow), PcP (pink), PmP (light blue), and Pn (green) events.

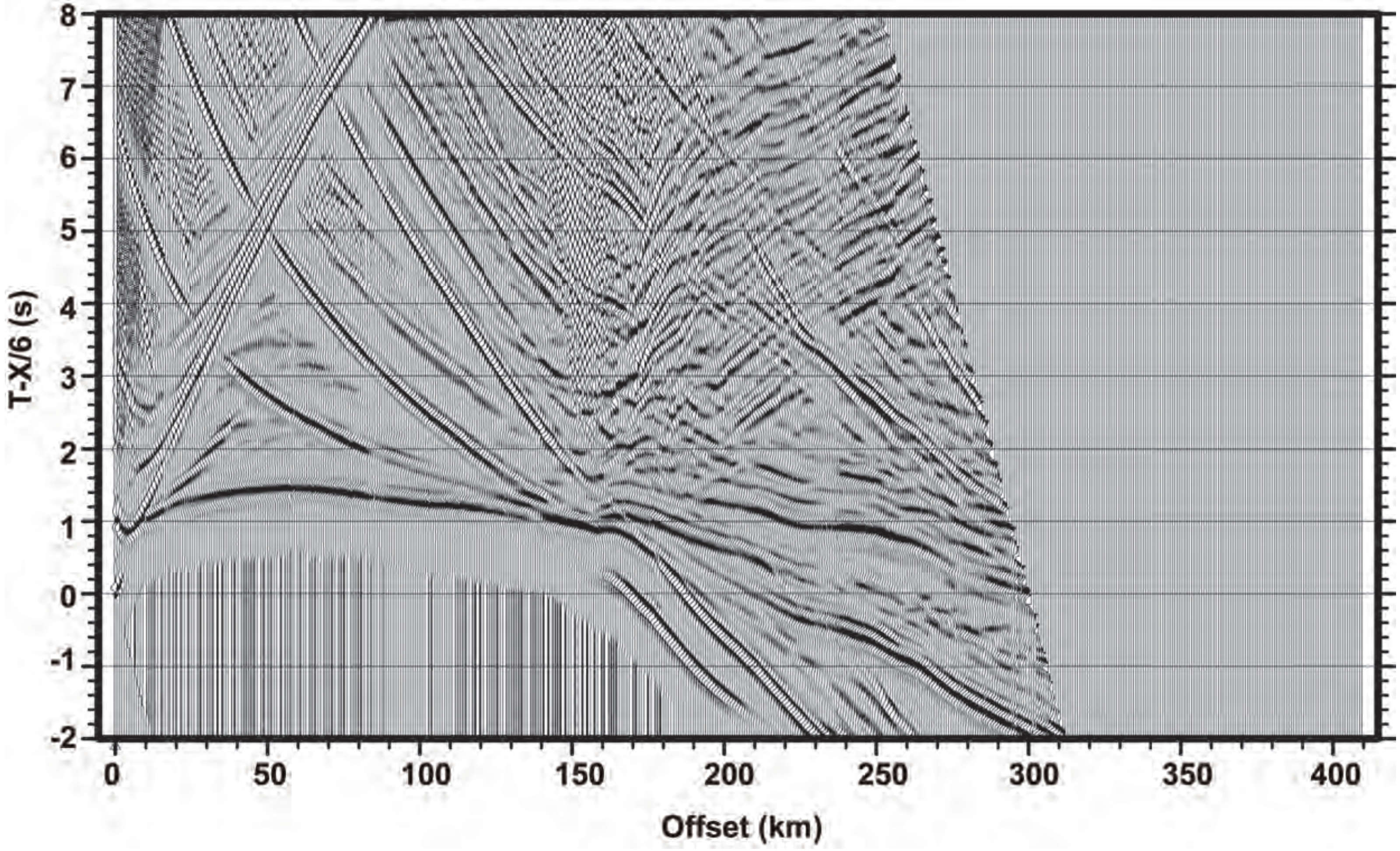

Figure 1. Synthetic seismogram for SP 11 that was created using a commercial finite difference solution of the scalar wave equation.

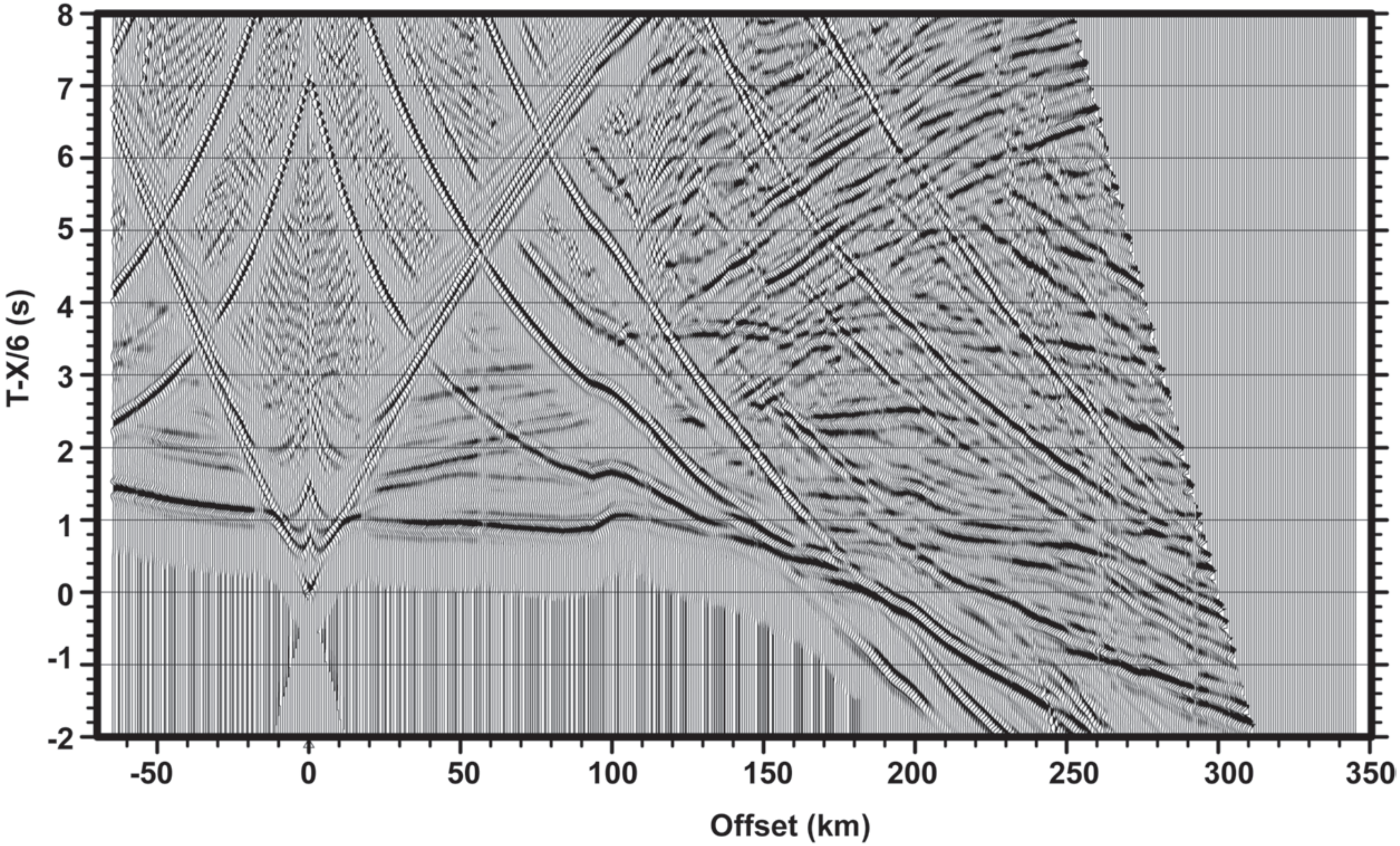

Figure 2. Synthetic seismogram for SP 12 that was created using a commercial finite difference solution of the scalar wave equation.

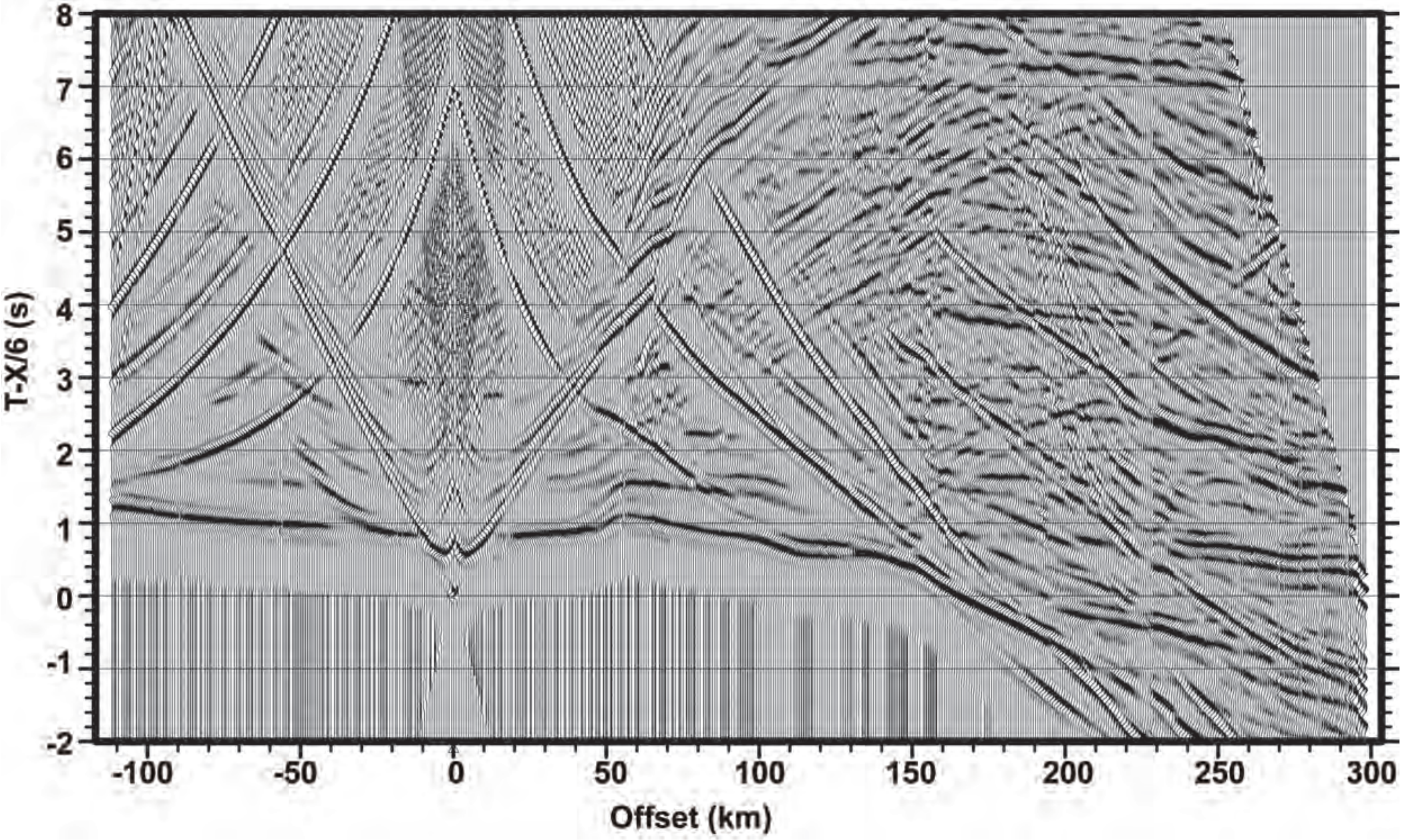

Figure 3. Synthetic seismogram for SP 13 that was created using a commercial finite difference solution of the scalar wave equation.

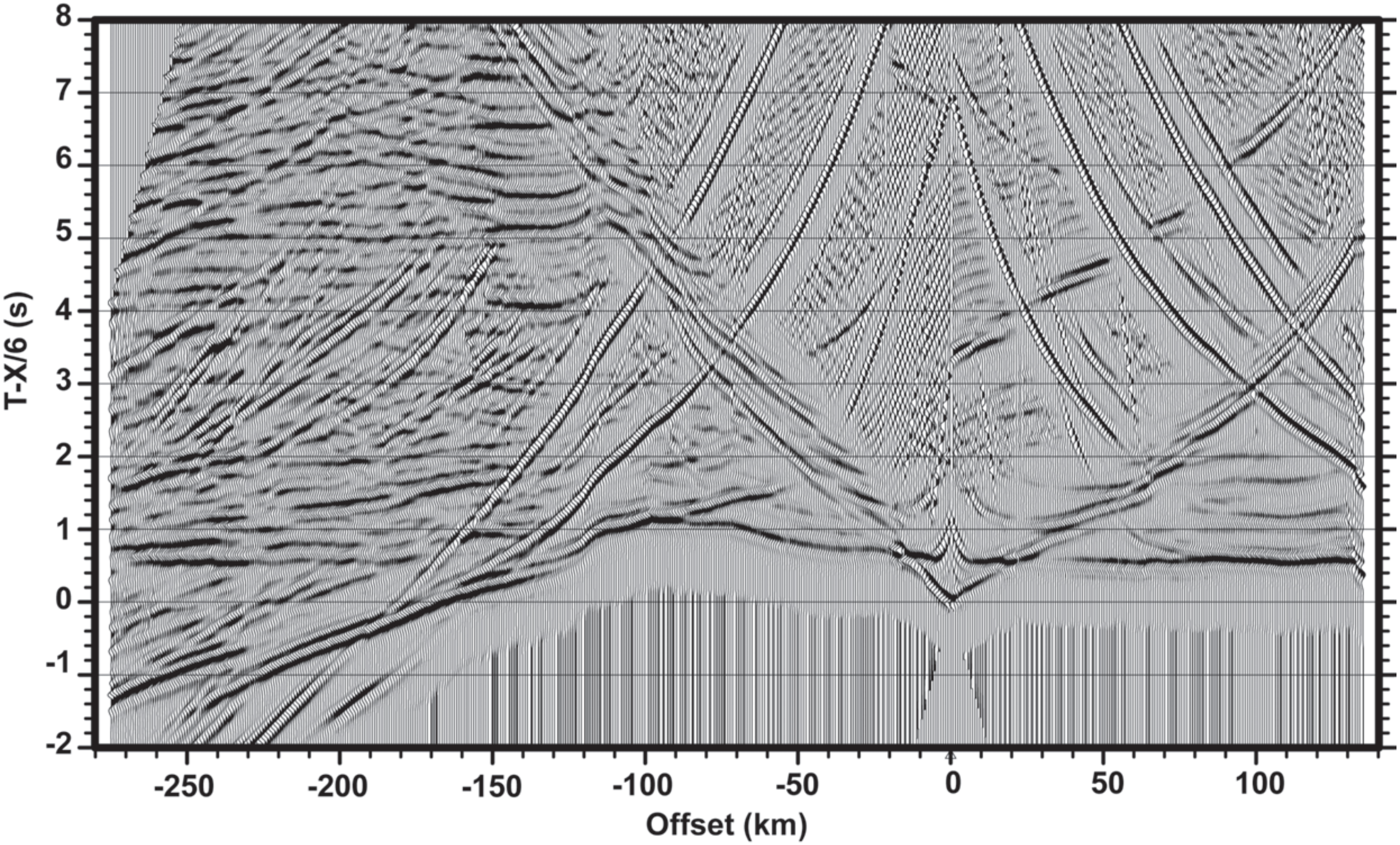

Figure 4. Synthetic seismogram for SP 15 that was created using a commercial finite difference solution of the scalar wave equation.

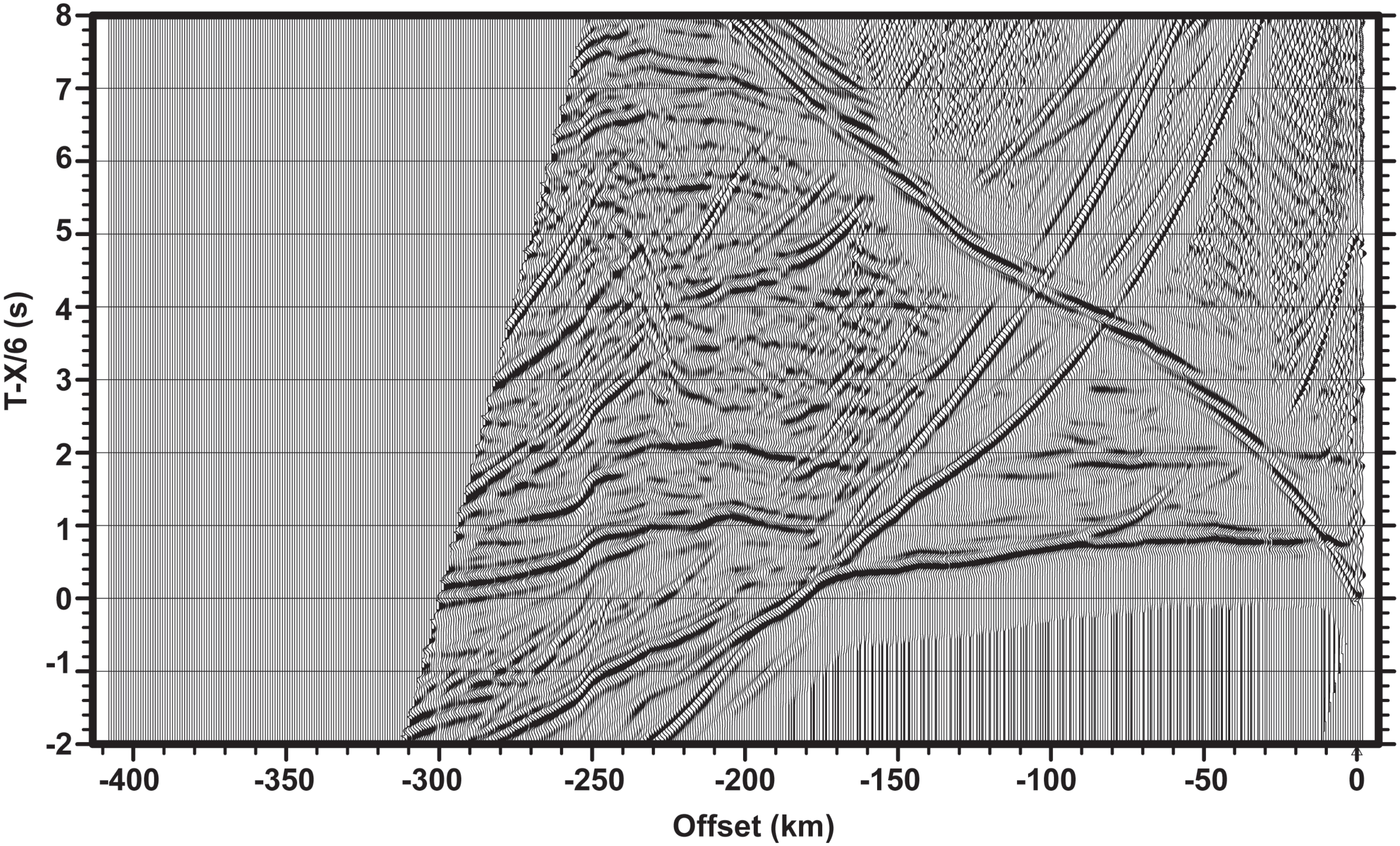

Figure 5. Synthetic seismogram for SP 17 that was created using a commercial finite difference solution of the scalar wave equation.